Evaluating Multi-Temporal DInSAR Measurements of Ground Surface Deformation Around the Rhenish Coalfields in Germany Using Sentinel-1 SAR Imagery

by

Mieszko Fydrych

A thesis
presented to the University of Waterloo
in the fulfilment of the
thesis requirement for the degree of
Master of Science
in
Geography

Waterloo, Ontario, Canada, 2021

Author's Declaration

I hereby declare that I am the sole author of this thesis. This is a true copy of the thesis, including any required final revisions, as accepted by my examiners.

I understand that my thesis may be made electronically available to the public.

Abstract

Ground surface deformation caused by land subsidence is a critical aspect when assessing safety and environmental impacts of open-pit mining operations. These mining-induced deformations can cause severe damage to local infrastructure and buildings located in the region. Monitoring mining operations using traditional techniques is laborious, costly and time consuming, with many locations being difficult to access. As a result, in-situ observations of surface movement and structural stability are often sparsely completed along areas of high risk or concern. Remote sensing observations facilitate a reliable, temporally and spatially continuous monitoring process of mining operations, regardless of physical accessibility, at large scales with minimal cost. In this study, two commonly used C-band Differential Interferometric Synthetic Aperture Radar (DInSAR) methods, namely Small Baseline Subset (SBAS) and Persistent Scatterer Interferometry (PSI), are applied to Sentinel-1 data to show consistency when observing land displacement in the Rhenish coalfields region in Germany. Deformation rates around the Rhenish coalfields are assessed for 2015 and 2016, independently, using both techniques and compared using GNSS station data of three nearby stations part of the EUREF network. The primary focus on this study is to determine the performance differences between the two techniques. The PSI deformation estimates showed significantly lower variation in measurements but had a severely limited spatial coverage compared to the SBAS estimates. Comparison of annual deformation rates measured by the two techniques showed a stronger agreement for 2016 (RMSE = 8.7 mm/year) than 2015 (RMSE = 26 mm/year). The discrepancy between annual comparisons is caused by overestimation of surface subsidence rates by the 2015 SBAS measurements. This overestimation is likely the result of atmospheric artefacts propagating into the phase unwrapping due to a lack of sufficient SAR scenes available in 2015. It was determined that the SBAS technique benefits more heavily from additional data and when data is limited, the PSI technique proves to be more reliable for measuring annual deformation rates. Despite this, both techniques observed similar overall deformation patterns across the landscape but reported different magnitude of deformation; commonly observed in other studies. The two methods showed stronger agreement over targets characterized as hard impermeable surfaces (e.g. built-up areas). Although only one of the three publicly available GNSS sites coincided with the InSAR study domain, when compared with base station GNSS sites, the DInSAR estimates are within the uncertainty range of the GNSS measurements, indicating good potential. This thesis illustrates the applicability of using satellite remote sensing observations to monitor mining-induced surface deformations to supplement traditional monitoring techniques.

Table of Contents

List of Figures

Chapter 1

Introduction

1.1 Context and Motivation

Ground surface deformations caused by land subsidence is one of the most common yet critical issues relating to the mining industry, having a significant impact on the surrounding environment. Such mining-related deformations can cause severe damages to local infrastructure and buildings located near the area of operation (Pawluszek-Filipiak and Borkowski, 2020; Tang et al., 2020). However, even with the deployment of careful mining techniques, the occurrence of ground surface deformation is inevitable, likely causing damage to surrounding infrastructure. Therefore, the monitoring of land deformation is imposed by legislation and used to verify subsidence prediction, maximize extraction rates and reduce the risk posed to the environment (Pawluszek-Filipiak and Borkowski, 2020). Additionally, monitoring mining-induced ground deformation can provide valuable insight of the small surface movements on a mine high wall, showing signs of instability that may preface a catastrophic slope failure (Tang et al., 2020). Therefore, effective and reliable monitoring of mining-induced ground deformation is an essential component, necessary for every active mining operation.

Conventional techniques for monitoring surface movement, such as inclinometers, surveying level techniques, total station and GNSS station, are the main deformation monitoring systems used by major mining operations (Paerse et al., 2014; Tang et al., 2020). The advantages of using these techniques are their capacity for direct observations and high accuracies. Unfortunately, these techniques are typically labour intensive, time consuming, expensive and require direct access to a given region (Pawluszek-Filipiak and Borkowski, 2020). As a result, conventional techniques are often limited to highly localized areas of a few square kilometers at predefined areas of high risk (Paerse et al., 2014; Pawluszek-Filipiak and Borkowski, 2020). In some circumstances, predefined areas are not easily accessible and installation of monitoring equipment might be non-permanent due to the dynamic nature of a mining operation (Tang et al., 2020). This can result in important measurement gaps that limit the spatial coverage of a region. Additionally, traditional monitoring techniques are performed infrequently, and often on a point-by-point basis, resulting in highly localized spatial extent data that does not provide sufficient insight of the wider context of deformation patterns around a given mining operation (Pawluszek-Filipiak and Borkowski, 2020., 2020).

To address these issues, remote sensing techniques have become an important technique for assessing large scale ground surface deformation (Lazecký et al., 2010; Ji et al., 2016). Differential interferometric Synthetic Aperture Radar (DInSAR) techniques allow for remote measurements of

ground deformation in all weather conditions, with high levels of precision, over large areas without the requirement of access to a given region (Xu et al., 2001; Khakim et al., 2013). DInSAR exploits phase differences between two synthetic aperture radar (SAR) acquisitions over the same area at different times. Traditional DInSAR estimates exploit a single interferometric pair, with the accuracy of this technique limited by factors relating to the topographic and orbital errors, spatial and temporal decorrelation, signal propagation delays from atmospheric artefacts and DEM errors (Ferretti et al., 2007). Additionally, conventional DInSAR is limited to measuring surface deformation in only the line-of-sight (LoS) direction, relative to the satellite sensor. More sophisticated multi-temporal DInSAR techniques have been developed that incorporate more than two repeat pass SAR acquisitions to overcome these limitations.

Two of the most prominent multi-temporal DInSAR techniques are the Persistent Scatterer (PSI) approach (Ferretti et al., 2001; Hooper et al., 2007) and the Small Baseline Subset (SBAS) approach (Berardino et al., 2002). The primary difference between these two techniques is the type of targets that are identified and measured. The PSI approach aims to detect persistent scatterers which are point-wise deterministic objects containing single point scatterers with stable phase across a long temporal period (Hooper et al., 2007; Ferretti et al., 2011; Pawluszek-Filipiak and Borkowski, 2020). These objects generally correspond to human-made structures or large hard surfaces. Comparatively, the SBAS approach aims to identify distributed scatters that correspond to small groupings of pixels belonging to areas of moderate coherence in some parts of the temporal span (Ferretti et al., 2011; Pawluszek-Filipiak and Borkowski, 2020). These small groupings of pixels typically correspond with stable scattering areas such as debris fields, non-cultivated or desert areas. Both advanced multi-temporal DInSAR techniques allow for millimeter-scale displacements to be measured over long periods by reducing the contribution from various error sources (Tang et al., 2020). Several studies have successfully used multi-temporal DInSAR techniques to monitor ground surface deformation over wide areas (Hooper et al., 2007; Ferretti et al., 2011; Chaabani & Deffontaines, 2020; Liu et al., 2020; Tang et al., 2020), with several studies demonstrating comparable accuracy of measurements between DInSAR and conventional survey measurements (Lauknes et al., 2006; Lazecký et al., 2010; Fárová et al., 2019; Pawluszek-Filipiak and Borkowski, 2020). However, although these advanced techniques can help provide a more detailed understanding of surface deformation patterns, they are not suitable as stand-alone replacements for conventional techniques (Paerse et al., 2014; Pawluszek-Filipiak and Borkowski, 2020).

The main disadvantage of DInSAR techniques is its inability to detect fast moving ground surface deformations due to the ambiguous nature of interferometric phase and temporal decorrelation. The maximum deformation rate that can be measured by a DInSAR process is dependent on the revisit period

of the SAR observation and the wavelength used for observations (Samsonov et al., 2015). This value is limited to a quarter of the wavelength over the revisit interval between image acquisitions. Due to the long revisit period of older systems, such as ERS and Envisat, this technique was often not applicable to monitoring mining-induced surface deformations. However, the short revisit period of the Sentinel-1 mission (12-day or 6-day) improves the maximum deformation rate that can be measured across a given period. Using the C-band with a wavelength of 5.5 cm, the maximum detectable deformation rate using Sentinel-1 is 1.4 cm every 6 or 12 days, depending on the availability of Sentinel-1B data. Without Sentinel-1B, this gives a maximum deformation rate of 42.5 cm/year which improves to 85 cm/year if Sentinel-1B imagery is available, which reduces the revisit interval by half. Additionally, the relatively small perpendicular baselines of Sentinel-1 data results in reduced DEM error in the measurements, improving the capability to measure deformation rate of continuously changing topography (Tang et al., 2020).

This study uses 64 Sentinel-1 SAR images, in ascending geometry, and multi-temporal DInSAR techniques to measure ground surface deformation around the Rhenish Coalfields in Germany. Within these coalfields are three large open pit lignite mines (Hambach, Inden and Garzweiler) which provide the state of North Rhine-Westphalia with around 40% of their power requirements. Deformation around the mining operations is measured for 2015 and 2016 using Persistent Scatterer and Small Baseline Subset approaches. However, due to decorrelation issues, the mining pits themselves are omitted from the study. The final measurements are then compared to GNSS station data of 3 nearby stations part of the EUREF network. The main purpose of this study is to determine the performance differences between the two multi-temporal DInSAR techniques rather than to determine absolute deformation rates around the Rhenish coalfields.

1.2 Aims and Objectives

The overall aim of this thesis is to evaluate the capability of multi-temporal DInSAR methods to monitor ground surface deformation around the Rhenish coalfields in Germany using Sentinel-1 SAR data. To achieve this, the following objectives were defined:

1. Quantify and characterize land surface movement around the mines using multi-temporal DInSAR techniques;
2. Evaluate InSAR estimates using in-situ GPS measurements;
3. Evaluate the performance differences between PSI and SBAS;

1.3 Thesis Structure

This thesis has been written using the traditional monograph format. Chapter 2 presents background information on SAR, InSAR, multi-temporal DInSAR techniques and the use of multi-

temporal DInSAR for monitoring surface deformation. Chapter 3 describes the study region and the data used in this study. Chapter 4 outlines the methodology and parameters used. Chapter 5 presents the findings of the proposed methodology. Chapter 6 analyzes and discusses the findings, limitations and recommendations for future work. Chapter 7 provides a summary of key findings and concluding remarks.

Chapter 2

Background

2.1 SAR Basics

Synthetic Aperture Radar (SAR) is an active microwave imaging method that uses a pulsed radar installed on a forward moving platform providing high-resolution two-dimensional images independent from daylight, cloud coverage and weather conditions (Moreira et al., 2013). The system uses a high-power pulse sent from a transmitting antenna to illuminate a surface and a receiver to record the echoes of backscattered signal after interacting with the surface. This reflected signal, called the echo, is backscattered from the surface and the returning amplitude and phase of the signal is recorded and used to construct the image (European Space Agency, 2007). These characteristics of the echo are determined by the physical and dielectric properties of the radar-illuminated surface such as roughness, geometry and permittivity. In a monostatic system, the transmitting antenna sends a beam of microwave pulses towards the target and the returning signals are received by the same antenna. A bistatic or multi-static system spatially separates the transmitting antenna from the receiver antennae to improve capability and reliability (Wang & Deng, 2018).
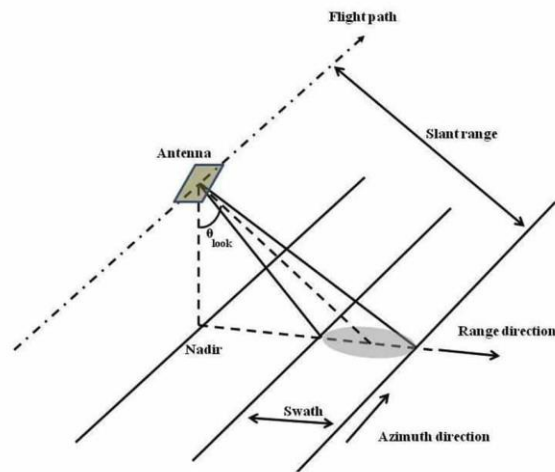
Figure 1. Visualization of a typical side-looking SAR configuration (Alaska Satellite Facility, n.d.).

The configuration of a typical side-looking SAR system is shown in figure 1. The azimuth is the flight direction, the range is the direction perpendicular to the azimuth and the nadir is a vertical line directly below the sensor. As the platform moves along the azimuth, the radar beam illuminates a continuous area called the swath, and the ground area illuminated by the antenna is referred to as the footprint. The near range refers to the portion of the swath closest to the nadir track while the far range refers to the furthest portion. The radar beams are transmitted at a look angle, relative to the nadir, and

interact with a surface at an incidence angle, relative to the vertical of the target surface. The slant range is the actual range measured from the system to the target, derived from the time delay of the echo. Ground range is the slant range projected onto a reference surface and represents the perpendicular distance of the target from the nadir. Deviations of the target surface from the reference cause topographic distortions and influence local range resolutions in the final image (Woodhouse, 2006).

Slant range resolution is a system-limited parameter that is independent of the target surface and dependent on the pulse bandwidth. The ability to discriminate features that are on the Earth's surface is referred to as the ground range resolution. This resolution is determined as a function of the local incidence angle and slant range resolution. Deviations from the target surface to the reference surface influence the local incidence angle consequently impacting the local range resolutions. As the angular distance from nadir is increased, the incidence angle increases resulting in an improved ground range resolution at the far range and a degraded resolution at the near range (Woodhouse, 2006). The azimuth resolution is the ability to discriminate two features at the same range but varying azimuth angles. For any given wavelength, the azimuth angle can be controlled by length of the antenna or by synthesizing an effective antenna length (European Space Agency, 2007). To achieve improved azimuthal resolution and practical spatial resolutions from space, a SAR synthesizes a larger effective antenna by exploiting Doppler mechanics and using a small antenna which moves along the flight line (Woodhouse, 2006; European Space Agency, 2007).

2.2 Radar Equation

All radar systems measure a target distance through the time delay of a faint echo. To determine whether this echo can be detected, the radar equation is used to calculate the proportion of the transmitted energy that is returned from a target (Woodhouse, 2006). This equation assumes a monostatic radar system, in which the transmitter and receiver share the same location, and traces the radar signal from the transmitter, to the target and back to the receiver. This equation takes the following parameters into consideration: the range, R, of the target from the radar antenna, the directional sensitivity of the antenna or the gain, G, and the radar cross-section, σ, of the observed target.

As energy is transmitted in a spherical pattern, the power density (P_t) of a signal decreases proportionally with its distance, of radius R, from the antenna. The power, measured in watts, leaving the antenna is shaped by antenna sensitivity patterns derived from the gain and reduced by a factor proportional to the surface area of the sphere intercepted at radius R (Woodhouse, 2006). The power intercepted and scattered back by the target is given by:

$$Power\ scattered\ by\ target = \frac{P_t G \sigma}{4\pi R^2} \qquad \text{(Eq. 1)}$$

As the scattered power response is also transmitted in a spherical pattern, there is a decrease in power density of the scattered signal at the receiving antenna, P_r , proportional to increasing return distance. Of this returning signal, some amount of the signal is intercepted by the target with an effective area (A_e) proportional to the surface area of a sphere with radius R. Therefore, A_e can be considered the equivalent of a cross-section of the antenna. Given this, the power density of the signal received is given by:

$$Signal\ received = P_r = \left(\frac{P_t G \sigma}{4\pi R^2}\right) \frac{A_e}{4\pi R^2} \tag{Eq. 2}$$

The effective area, A_e, is related to the transmitting gain, G, and wavelength of the radar, λ, expressed by:

$$A_e = \frac{G\lambda^2}{4\pi} \tag{Eq. 3}$$

Substituting this term into equation 2, the radar equation for a monostatic system can be expressed by:

$$P_r = \frac{P_t G^2 \lambda^2 \sigma}{(4\pi)^3 R^4} \tag{Eq. 4}$$

It should be noted that the signal response deteriorates very rapidly with the range, limiting the operationality of an instrument. To ensure signal from a typical target is usable, the returned signal must be larger than the instrument noise, N_o. As such, equation 4 is often rewritten as the *signal-to-noise ratio* (SNR) equation:

$$\left(\frac{P_r}{N_0}\right) = \frac{P_t G^2 \lambda^2 \sigma}{(4\pi)^3 R^4 N_0} \tag{Eq. 5}$$

The power intensity and SNR both increase linearly with transmitted power and increases exponentially with the antenna size. The exponential increase is result from the antenna length being used for both transmission and reception of the signal.

Of all the factors used in this equation, σ is the only one that is not dependent on the system configuration but rather on the target's properties. However, as targets in Earth observation are typically characterized as a distributed area rather than a discrete object, this cross-section is often normalized (Woodhouse, 2006). Normalizing σ by the illuminate area, A, gives the capability to compare measurements of a target from different instruments. The normalized equation for the radar cross-section is solved by rearranging equation 5 as:

$$\sigma^0 = \frac{\sigma}{A} = P_r \frac{(4\pi)^3 R^4}{A P_t G^2 \lambda^2} \tag{Eq. 6}$$

2.3 Frequency and Wavelength
The wavelength of the transmitted signal determines how the signal interacts with a surface and how far it can penetrate a medium. Generally, longer wavelengths provide deeper penetration into

vegetation canopies and soils while shorter wavelengths provide a better resolution but respond to surface scattering. SAR sensors use long wavelengths, ranging from the centimeter to meter scale, allowing the system to penetrate cloud, vegetation and surface soil layers. This spectral range is divided into frequency bands defined during the second world war and shown in table 1. For spaceborne SAR system, the commonly used frequency bands range from X- to P-band. As X-band has a shorter frequency, it is often used for urban and infrastructure monitoring because of its strong surface response. However, it's lack of penetration limits it ability to monitor sub-canopy vegetation (Flores-Anderson et al., 2019). Comparatively, L-band systems have lower frequency and an enhanced canopy penetration capability proving itself useful to for monitoring change under canopies such flooding (Flores-Anderson et al., 2019). With a wavelength between the X- and L-bands, the C-band acts a compromise between the two; relative to X-band systems, C-band offers better canopy penetration and wider swath coverage, making it more ideal for global-scale monitoring. Although C-band has increased canopy penetration relative to the X-band, it will not penetrate dense canopies, limiting its applicability of vegetation studies. As such, C-band is often used to for hazard monitoring, land use change and crop and forest monitoring (Flores-Anderson et al., 2019).

Table 1.Designation of microwave bands (Flores-Anderson et al., 2019).

Band	Frequency	Wavelength
Ka	27 – 40 GHz	1.1 – 0.8 cm
K	18 – 27 GHz	1.7 – 1.1 cm
Ku	12 – 18 GHz	2.4 – 1.7 cm
X	8 – 12 GHz	3.8 – 2.4 cm
C	4 – 8 GHz	7.5 – 3.8 cm
S	2 – 4 GHz	15 – 7.5 cm
L	1 – 2 GHz	30 - 15 cm
P	0.3 – 1 GHz	100 - 30 cm

2.4 Polarization and Scattering Mechanics

Polarization refers to the orientation of the plane of oscillation of the transmitted signal in the plane perpendicular to the direction of propagation (Moreira et al., 2013). SAR sensors are commonly linearly polarized, transmitting and receiving horizontally and/or vertically polarized signals. Horizontal polarization limits the signal to a horizontal plane while a vertical polarization limits the signal to a plane perpendicular to the horizontal, as seen in figure 2. In a SAR system, the polarization of signal being

transmitted and received can be controlled with signals transmitted and received in both vertical and horizontal polarizations leading to the four possible configurations: VV, HH, VH and HV. The first two configurations are referred to as like-polarized, indicating the polarization of the transmitted signal is the same as the received signal. The latter two configurations are referred to as cross-polarized, indicated the polarization of the transmitted is orthogonal to the polarization of the received signal. A single polarization system only has one of the configurations stated and is usually like-polarized but cross-polarized single polarization systems do exist. Having a combination of two configurations, such as VV and HH or VV and VH, is known as a dual polarization system and a system with all four configurations is referred to as a quadrature polarimetric or a full polarimetric system.

© CCRS / CCT
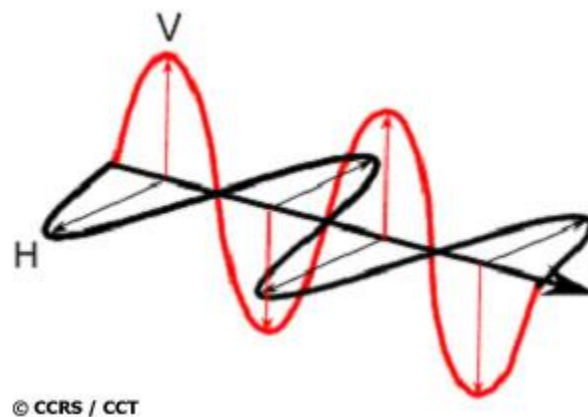
Figure 2. Visualization of vertical (red) and horizontal (black) polarization (National Resources Canada, 2015).

The polarization of the signal impacts how the signal is scattered when interacting with a surface and the recorded radar brightness of the object. When interacting with a surface, radar signals are subjected to three types of scattering: rough surface scattering, double bounce scattering and volumetric scattering (figure 3.) Rough surface scattering caused by bare soil, water, paved surfaces and low vegetation is most sensitive to VV polarization. Double-bounce scattering is caused by vertical structures, such as buildings or trees, that reflect an already reflected signal back towards the receiver and is most sensitive to cross-polarization. Finally, volumetric scattering is caused by the signal bouncing multiple times as it propagates through a structure of randomly distributed discrete elements, such as vegetation canopies and is most sensitive to HH polarization. Scattering mechanics and backscatter returns are also influenced by the local incidence angle.

As these polarizations are sensitive to different forms of scattering, the application of SAR is dependent on the polarization configuration used. As VV polarization is sensitive to surface scattering, it is used in several applications including DInSAR deformation measurements (Braun & Veci, 2020). HH polarizations prove useful when measuring soil moisture under vertically oriented crops such as

barley or wheat as the signal has improved penetration and likelihood of reaching the soil (European Space Agency, 2007). As cross-polarized signals are less sensitive to surface roughness, these configurations are useful for differentiating between volumetric and surface scatterers. Examples of this application include ship detection over water (Touzi, 1999), and separating broadleaf vegetation from grain crops (European Space Agency, 2007; Flores-Anderson et al., 2019).
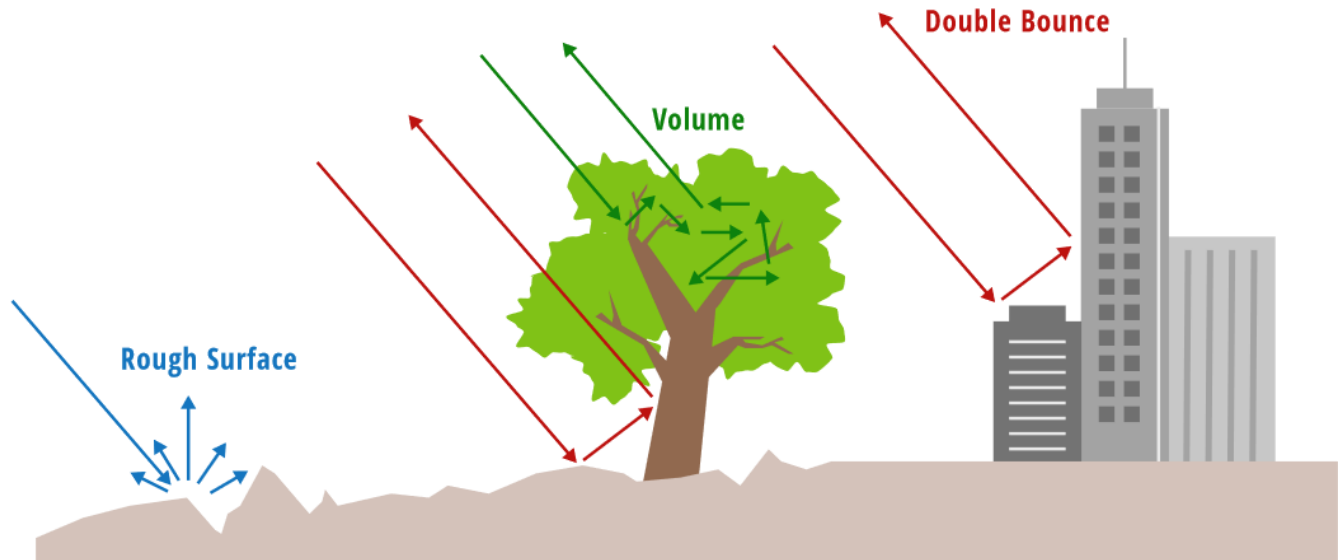
Figure 3. Visualization of the different types of backscattering: Rough Surface scattering, Volumetric scattering and Double Bounce scattering (Flores-Anderson et al., 2019).

2.5 C-Band Radar Observations Used in This Study: The Sentinel-1 Mission

The European Space Agency (ESA) developed a series of missions called Sentinels, under the European Union's Copernicus program, to provide optical and radar observations of the Earth's surface. Each mission is based on a constellation of two satellites to improve revisit and coverage requirements. The Sentinel-1 mission consists of twin polar orbiting SAR satellites, Sentinel-1A and Sentinel-1B, launched in April 2014 and April 2016, respectively. Although the revisit period of a Sentinel-1A is 12 days, the mission images the entire Earth every six days by having Sentinel-1B operate within the same orbital plane but with a 180° offset from its counterpart. The mission includes C-band imaging operating in four imaging modes with spatial resolutions as small as 5 m and coverage up to 400 km and dual polarization capability. The four imaging modes are: Stripmap (SM), Interferometric Wide swath (IW), Extra-Wide swath (EW) and Wave (WV).

The SM, IW and EW modes are available in dual polarization (VV+VH or HH+HV) or single polarization (HH or VV) while the WV mode is only available in single polarization. SM provides uninterrupted coverage at 5m by 5m spatial resolution with a swath size of 80km and a coverage of 375km. Improving swath size at the expense of resolution, IW and EW offer resolutions of 5m by 20m

and 20m by 40m with swath widths of 250k and 400km, respectively. The IW and EW modes implement a new type of ScanSAR called Terrain Observation with Progressive Scan (TOPS) SAR. The basic principal of TOPSAR is to shrink the azimuth antenna pattern, as seen by a spot target, to reduce scalloping effects in the image and achieve the same coverage and resolution as ScanSAR with nearly uniform SNR and Distributed Target Ambiguity Ratio (DTAR). WV captures a single stripmap image with an alternating elevation beam producing vignettes of 20km by 20km at regular intervals of 100km.

Each mode can generate products at three processing levels: Level-0, Level-1 and Level-2. Level-0 products consist of compressed unfocused SAR raw data and required decompression and processing to become usable. Level-1 products are intended for most users and produced as Single Look Complex (SLC) and Ground Range Detected (GRD). SLC products include a single look in each dimension using the full transmit signal bandwidth and contain complex samples preserving the phase information. GRD products are detected, multi-looked and projected to ground range using an Earth ellipsoid model. The resulting product has approximately square spatial resolution pixels with reduced speckle at the cost of degraded spatial resolution and the loss of phase information. Level-2 products are used for ocean applications and includes Ocean Swell spectra, Ocean Wind Fields and Surface Radial Velocities.

Sentinel data products are made freely available to all users including the general public, scientific and commercial users. The data can be delivered within an hour of reception for Near Real-Time (NRT) emergency response and within three hours for NRT priority areas and within 24 hours for systematically achieved data. Each Sentinel-1 satellite is expected to transmit data for at least 7 years and has fuel for 12 years.

2.6 InSAR

Interferometric Synthetic Aperture Radar, or InSAR, can be explained as the acquisition of two or more complex SAR images of the same area used to compute additional information about the imaged terrain through the application of phase differencing of returning transmitted signals (Lawal et al., 2016). By measuring the phase of two or more returning radar waves, the phase differences between these waves can be converted into topography or vertical and lateral displacements assuming the wavelength and perpendicular baseline are known factors (Khakim et al., 2013). Traditional InSAR processing requires an image to be assigned as the master, and a secondary image to be assigned as the slave. These images can be collected simultaneously through a single-pass using a bistatic system or through repeat-passes using a monostatic configuration. A schematic for InSAR viewing geometry is seen in Figure 4. The polarization of these images must be the same, as image pairs with different polarizations cannot be combined to generate a single interferogram (Ferretti et al., 2007). For measuring surface deformation and elevation, the VV polarization is preferred due to its sensitivity to rough surface scattering.
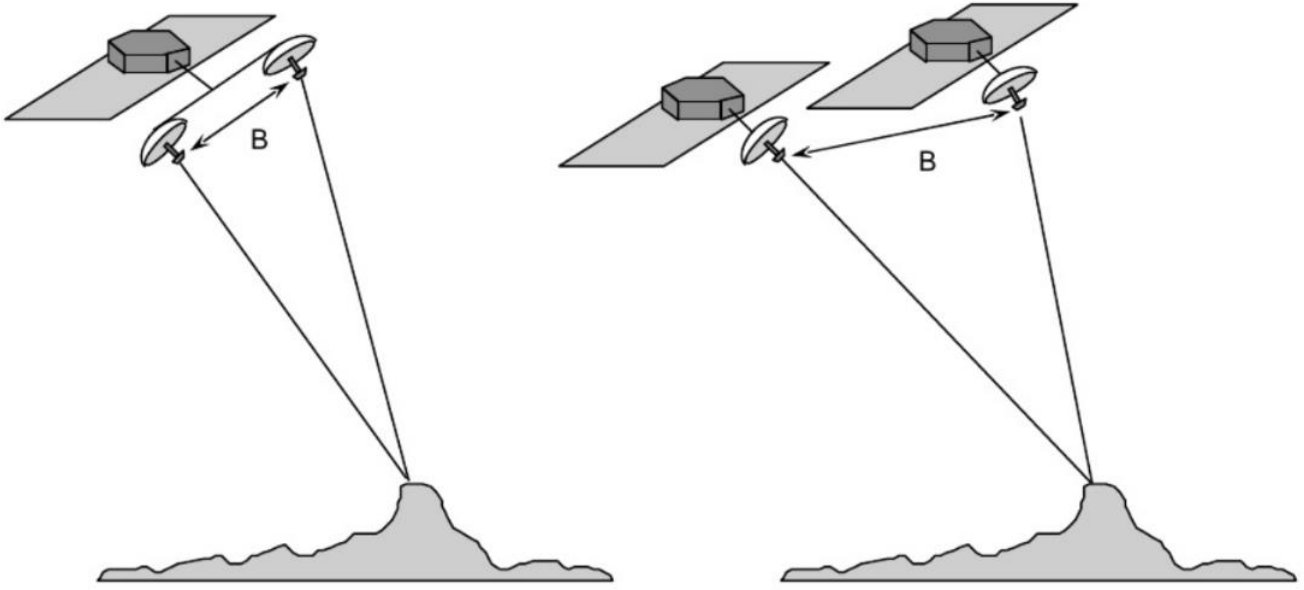
Figure 4. Visualization of a bistatic SAR acquisition (left) and a repeat pass monostatic SAR acquisition (right). The perpendicular baseline of the image pairs is denoted by B.

A SAR interferogram is created by cross-multiplying, pixel-by-pixel, a master SAR image with the complex conjugate of a second SAR image, referred to as the slave image (Ferretti et al., 2007). The resulting interferogram has amplitude values of the master image's values multiplied by the values of the second image, whereas the phase information of the interferogram (interferometric phase) is calculated as the phase difference between the two images. Within an interferogram, the phase information is represented as fringes. A fringe is a colour cycle, typically ranging from red to blue, that represents the phase differences of the two images. During this process, the images are co-registered and geometrically corrected to fit one another, allowing for direct pixel-to-pixel comparisons of the datasets (Ferretti et al., 2007; Khakim et al., 2013). The multiplication of amplitudes and differences in phase is given as:

$$\phi_{in} = \frac{4\pi\Delta R}{\lambda} \qquad\qquad (Eq.\ 7)$$

where ϕ_{in} is the interferometric phase, ΔR is the differences in line of sight distances measured by the two acquisitions and λ is the wavelength used. The interferometric phase information is the sum of several phase contributions and can be expressed with the following:

$$\phi_{in} = \phi_{topo} + \phi_{ref} + \phi_{orb} + \phi_{atm} + \phi_{def} + \phi_n \qquad\qquad (Eq.\ 8)$$

The total interferometric phase thus contains contributions from the topography ϕ_{topo}, the reference surface ϕ_{ref}, orbital errors ϕ_{orb}, phase delays due to atmospheric changes between acquisitions ϕ_{atm}, ground deformation between acquisitions ϕ_{def}, and other noise ϕ_n. Of these phase contributions, ϕ_{topo}

and ϕ_{def} tend to be of most interest, as ϕ_{topo} can be used to create a DEM or DSM of an imaged surface and ϕ_{def} can be used in DInSAR to measure surface deformations between acquisitions to a high level of accuracy. For traditional InSAR, ϕ_{topo} is the only part of the signal that is meaningfully used and is the result from different parallax angles at the two acquisition times. The phase contributions from topography ϕ_{topo}, can be calculated using the following:

$$\phi_{topo} = -\frac{4\pi B_{perp}h}{\lambda R sin\theta} \qquad \text{(Eq. 9)}$$

Where B_{perp} is the perpendicular baseline, θ is the incidence angle and h is the height of the surface measured. It should be noted that as B_{perp} approaches a very large number, ϕ_{topo} increases proportionally, and can overwhelm ϕ_{in}, rendering it useless (Ferretti et al., 2007). Since the topographic phase contributions scale linearly with the perpendicular baseline, precise knowledge of the perpendicular baseline is crucial (Khakim et al., 2013). The remaining phase contributes are treated as noise and need to be removed or mitigated.

Unwanted phase contributions are removed or mitigated depending on the application to isolate phase corresponding to the parameter of interest. Phase contributions from the reference surface ϕ_{ref} can create phase differences between two points of the same height. This is the result of orbital paths having large slope angle differences or not being parallel. This phase contribution can be calculated using the following:

$$\phi_{ref} = -\frac{4\pi B_{perp}\Delta R}{\lambda R tan\theta} \qquad \text{(Eq. 10)}$$

This phase contribution can lead to fringes occurring in the interferogram where the surface should be flat. To correct for this, the flat earth phase is removed using orbital data to calculate parallel baselines. This process is known as interferogram flattening. This generates a phase map proportional to the relative terrain altitudes (Ferretti et al., 2007).

Phase contributions due to orbital errors, ϕ_{orb}, are removed using the precise orbital data of the satellite. Applying these data to the interferograms provides precise three-dimensional references of the satellite's locations, relative to the surface, during the time of acquisition. After orbital corrections, errors resulting from incorrect coordinates cause a linear phase change across the interferogram that can overwhelm the phase contributions of topography or deformation. This trend is removed by subtracting phase values estimated using a Maximum-Likelihood frequency estimator (Lauknes et al., 2006).

Phase contributions from atmospheric delays and other noise sources (such as co-registration errors) cannot be directly removed and must be mitigated to reduce their impacts on ϕ_{in} so a given parameter can be more accurately isolated. Mitigating these contributions can be completed using

Gaussian filtering or by stacking interferograms. Stacking interferograms requires a larger dataset than a simple master-slave combination and averages out atmospheric and other noise error terms throughout a time series (Ferretti et al., 2011). Prominent examples of time series techniques include the PSI and SBAS processes.

The fringe values of an interferogram are bounded within the range of -π to π. Once interferograms have been corrected, this phase information can be unwrapped to provide a measure of elevation or land deformation (Khakim et al., 2012). This process is completed by transforming the discrete wrapped phase into continuous phase information from the interferogram. The transformation from discrete to continuous phase information is accomplished by restoring the correct multiple of 2π to each pixel in the interferometric image and removing the correct integer number of altitudes of ambiguity, equivalent to an integer number of 2π phase cycles (Werner et al., 2002; Ferretti et al., 2007). This phase unwrapping is completed using algorithms such as the Statistical-Cost Network-Flow Algorithm for Phase Unwrapping (SNAPHU), a least cost pathway algorithm developed by Chen and Zebker (2000).

Actual phase unwrapping tends to be more complicated than this because the phase can exceed the range of the –π to π. This is caused by phase noise, phase under-sampling, phase discontinuities and phase ambiguity. Phase noise is often reduced by filtering and multi-looking approaches; however, these techniques are unable to remove all the noise from an interferogram (Werner et al., 2002). Phase under-sampling occurs when the phase gradient exceeds half of a fringe, or phase cycle, per sample. This often occurs at lower gradients when phase noise is prominent (Werner et al., 2002). Phase discontinuities are representative of a jump in phase values caused by a discontinuous surface, such as a cliff, translating to a discontinuity of phase values across the interferogram. Phase ambiguity is when the incorrect integer multiple of 2π is applied to a pixel during phase unwrapping. This occurs when the displacement between neighbouring pixels exceeds half the wavelength as the result of phase discontinuities or high phase noise (European Space Agency, 2007; Samsonov et al., 2015).

For each interferogram, there is some defined height in which the interferometric phase change of 2π is generated after interferogram flattening (Ferretti et al., 2007). The altitude of ambiguity is inversely proportional to the perpendicular baseline and can be expressed using the following:

$$h_a = \frac{\lambda R sin\theta}{2B_\perp} \qquad \text{(Eq. 11)}$$

Generally, the higher the perpendicular baseline, the more accurate the altitude measure and the smaller the topographic height needed to a produce a fringe of phase change. Phase unwrapping solves this ambiguity by integrating phase differences across neighbouring pixels (Braun & Veci, 2020). A visualization of phase unwrapping is shown in Figure 5.
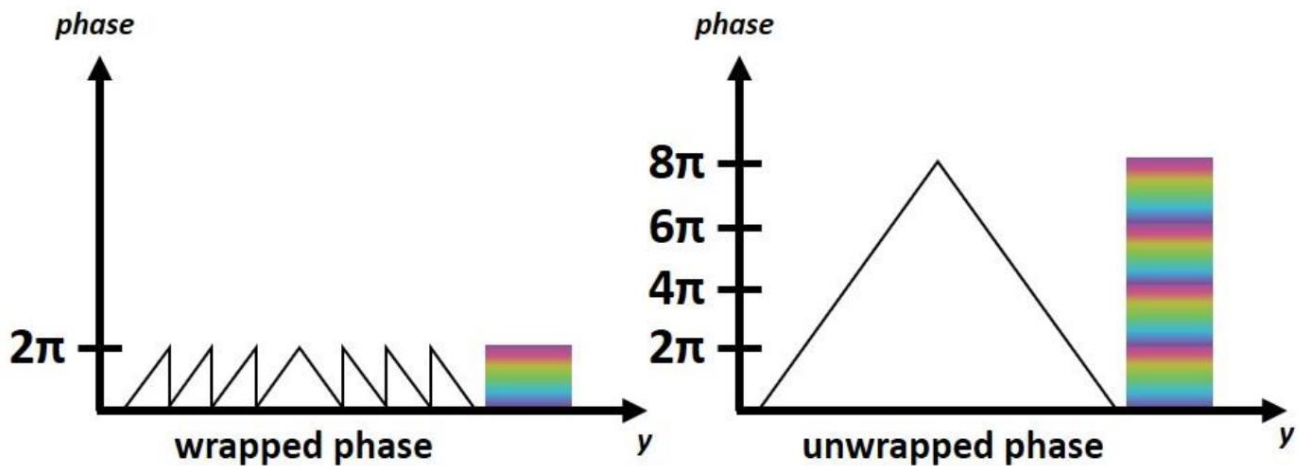
Figure 5. A demonstration of the principals of phase wrapping (Braun & Veci, 2020).

2.6.1 Baselines

When creating an interferometric pair, the temporal and perpendicular baselines of the image pair heavily impact the coherence and quality of the interferogram generated, as discussed in Section 2.6.2. The perpendicular baseline can be defined as the distance between the two satellites, or orbits, during the time the acquisition, measured perpendicularly from the transmitted wavelength of one satellite to the other (Ferretti et al., 2007). For measuring topography and DEM generation, a larger perpendicular baseline is preferred to accentuate the topographic contributions to the interferometric phase. These contributed are associated with observing a terrain from different viewing angles (Ferretti et al., 2007). For this use, perpendicular baselines between 150 and 300 meters are optimal. Conversely, smaller perpendicular baselines which minimize the topographic contributions are preferred for measuring displacements between images. By minimizing these contributions, the phase associated with deformation is more easily isolated and a less precise DEM will be required for topographic phase subtraction.

Smaller perpendicular baselines tend to have higher expected coherence values, improving the quality of the interferogram. However, interferograms with very small baselines values (< 30 meters) are almost useless due to their high sensitivity to phase noise and atmospheric effects (Ferretti et al., 2007). Interferograms with normal baselines (> ~450 meters) are usually almost impossible to unwrap unless an *a priori* DEM is available and the topography of the images surface is not very smooth (Ferretti et al., 2007). Such large perpendicular baselines also tend to have low coherence values due to decorrelation from geometrical and volume scattering (Ferretti et al., 2007). As the perpendicular baseline increases, the fringe frequency of the resulting interferogram proportionally increases (Rosen et al., 1999). This relationship can be defined as:

$$B_\perp = Bcos(\theta - \alpha) \tag{Eq. 12}$$

Where α is the baseline orientation angle and θ is the look angle. The maximum perpendicular baseline which can be used to reliably generate interferograms is referred to the critical baseline. More specifically, the critical baseline is the perpendicular baseline at which the phase rate reaches 2π per range resolution, interferometric fringes become too dense and the interferometric correlation becomes zero (Rosen et al., 1999). This critical baseline is dependent on the wavelength of the sensor used, the range and the range resolution. The critical baseline is determined by the following equation:

$$B_{crit} = \frac{\lambda \rho tan\theta}{n\Delta\rho} \tag{Eq. 13}$$

Where $\Delta\rho$ is the range resolution element. More simply, the critical baseline has the following proportionality relationship:

$$B_{crit} \propto \frac{\lambda}{\Delta\rho} \tag{Eq. 14}$$

When $B_\perp$ is greater than B_{crit} the spectral shift equals the bandwidth in the range direction, causing the signal to become entirely decorrelated, rendering the interferogram useless (Li et al., 2020). For Sentinel-1, the critical baseline is about 5188 meters (Chen et al., 2020).

The temporal baseline is defined by the time difference between image acquisitions. By varying the temporal baselines between interferometric acquisitions, deformation velocities ranging from several meters per second down to a few millimeters per year can be reliably measured (Moreira et al., 2013). For repeat pass imagery captured using monostatic systems, the temporal baseline is limited to an interval of the system's revisit period. As Sentinel-1 has a revisit period of 6 or 12 days (dependent on geographical location and availability of Sentinel-1B imagery), the temporal baselines for interferograms created using Sentinel-1 imagery will be constrained to multiples of 6 or 12 days. Although the same is true for single-pass image pairs created from bistatic systems, the temporal baseline for single pass image pairs is very small and often negligible. As the temporal baseline for an image pair increases, the amount of change that can occur between acquisition times increases. Thus, a longer temporal baseline often translates to lower coherence values. However, this is not always the case as certain landscapes, such as large deserts, can retain high coherence values even with very large temporal baselines of several years (Samsonov et al., 2015). Areas that experience large seasonal changes, particularly snow falls and vegetation changes, can have very low coherence values even with relatively short temporal baselines (Samsonov et al., 2015). Often, due to this relationship, non-coherent processes or landscapes that experience rapid change cannot be meaningfully measured using InSAR techniques with repeat-pass imagery. Reliably measuring or tracking of such processes often requires single-pass imagery to be used due to its capability to capture a discrete state of the phenomena during a discrete time. As a result, the

coherence for interferograms generated using single-pass imagery is not heavily impacted by a rapidly changing imaged surface.

2.6.2 Coherence

Coherence, γ, is an estimate of the phase noise of an interferometric pair and by proxy, the quality of the resulting interferograms (Ferretti et al., 2007; Khakim et al., 2013). It can also be described as measuring the similarity of the dielectric properties of pixels covering the same area (Khakim et al., 2013). Coherence is cross-correlation coefficient of the image pair estimated through a small window of a few pixels once all deterministic phase components are compensated for (Ferretti et al., 2007). These deterministic phase components are linear in both azimuth and slant-range and can be estimated from the interferogram using frequency detection of complex sinusoids in noise, such as Fast Fourier Transformations. Coherence values are bound within the range of 0 to 1, where 0 indicates the interferometric phase is purely noise and 1 indicates the complete absence of phase noise. Generally, coherence values above 0.3 to 0.35 are considered reliable and suitable for phase unwrapping, while pixels with lower coherence values are masked out as the phase unwrapping process for these pixels becomes either impossible or too inaccurate to be meaningful (Xu et al., 2001; Ferretti et al., 2007; Khakim et al., 2013; Samsonov et al., 2015). Thus, coherence analysis is a crucial step of InSAR processing as it is used to discriminate inappropriate InSAR pairs and assess the reliably of the phase unwrapping results.

Zebker and Villasenor (1992) describe coherence as the product of the thermal coherence $\gamma_{thermal}$, spatial coherence $\gamma_{spatial}$ and temporal coherence $\gamma_{temporal}$, defined as:

$$\gamma = \gamma_{temporal} \cdot \gamma_{spatial} \cdot \gamma_{thermal} \qquad \text{(Eq. 15)}$$

where $\gamma_{thermal}$ is characteristic by system noise, $\gamma_{spatial}$ is the result of viewing angle differences between the two acquisitions causing a parallax effect and $\gamma_{temporal}$ corresponds to physical changes to the scatterer between acquisitions. As such, coherence is affected by many factors, including temporal and perpendicular baselines, land cover, seasonal changes, atmospheric effects and the topography of the study area (Samsonov et al., 2015). Essentially, any change to the targeted surface, or the medium between the sensor and the surface can impact the coherence. In areas of dense vegetation, coherence is more susceptible to seasonal changes due to vegetation phenological changes, rapidly decreasing in value, while in desert-like environments it can remain relatively high for several years (Samsonov et al., 2015). By extension, the lowest coherence values are often related to water bodies, as the surfaces of these areas are constantly changing due to wind and water flow (Khakim et al., 2014), whereas the highest

coherency values are often found in areas with relatively unchanged ground conditions (Samsonov et al., 2015).

Significant effort is directed to maximizing the coherence between interferometric pairs to increase the number of acceptable pairs and the overall reliability of the results. Maximizing coherence can be done using several techniques, such as applying multilooking, adaptive filtering, pixel masking and selecting an ideal radar wavelength (Khakim et al., 2013; Paerse et al., 2014; Samsonov et al., 2015). As several of these techniques are not mutually exclusive, they are often used in conjunction with one another. Multilooking is the process of reducing SAR speckle noise, by averaging adjacent pixels within a window of N x N size, defined by the user, reducing the standard deviation of the noise and forcing noise in the SAR images into a more Gaussian distribution at the cost of decrease resolution (Gagnon & Jouan, 2000; de Leeuw & de Carvalho, 2009). Adaptive filtering works in a similar fashion but is done using post-image formation and does not affect the spatial resolution of the imagery (Gagnon & Jouan, 2000). Commonly, coherence masks are applied to interferograms after multilooking and filtering to omit pixels of low coherence from the unwrapping process (Samsonov et al., 2015; Yang et al., 2015). Such pixel omissions can reduce the occurrence of phase discontinuities and improper unwrapped phase calculations.

Although techniques such as multilooking and adaptive filtering can be applied to improve the coherence of existing interferograms, their effects can only be taken so far. More than by post-processing measures, coherence is impacted by the image pair parameters and the nature of the surface or phenomena being observed. Relevant image pair parameters include wavelength, polarization, perpendicular baselines and temporal baselines. The wavelength chosen, as discussed in Section 2.3, dictates the penetration and resolution of the signal. When measuring phase over vegetated areas, longer wavelengths penetrate deeper than shorter wavelengths, increasing the probability of the signal interfacing with a surface below the vegetation rather than a volumetric scatterer. This results in less temporal decorrelation and larger temporal baselines that can still provide usable interferometric pairs (Khakim et al., 2013). As a shorter wavelength also translates to a finer spatial resolution, the confidence that a pixel represents the same ground target in two different acquisitions is increased with shorter wavelength image pairs. As discussed in Section 2.4, signal polarization effects the scattering mechanisms of radar waves and what the signal is most sensitive to. For measuring topography, choosing a VV polarization increases the reliability of the returned signal interacting with the Earth's surface rather than vegetation. Summarily to using longer wavelengths, this increases the coherence by increasing the probability of the same surface being measured.

Longer perpendicular baselines tend to lower the coherence of image pairs, while shorter perpendicular baselines can exhibit the highest coherence (Canaslan & Ustun, 2012). This is primarily due to coherence loss in areas with foreshortening once the baseline exceeds a few meters. From a temporal baseline perspective, increasing the time delay between acquisitions increases the probability of large change occurring to an area, ultimately decreasing the coherence. However, Khakim et al. (2013) suggests that increasing the time interval between image acquisition can be used to increase the signal-to-atmospheric noise ratio. Conversely, Samsonov et al. (2015) determined that having a shorter time interval between images results in an increased average coherence, because target surface changes are minimized for non-dynamic surface types.

Coherence can also be improved by identifying a permanent source of consistent backscatter within the scene to act as a reference point. This practice improves the capability of year-round InSAR processing in areas that experience high seasonal fluctuations (Paerse et al., 2014). Common examples of permanent and consistent scatterers include local infrastructure, such as roads or facilities, which remain relatively unchanged between seasons and provide a consistent, clear and bright SAR response. By adjusting InSAR pairs so that the reference points selected have approximately the same phase, the coherence of the resulting interferograms is improved.

Another common methodology to improve coherence is interferogram stacking. This multi-temporal process stacks multiple interferograms on top of each other and averages the pixels values between slaves to provide a more reliable presentation of the Earth's surface (Ji et al., 2016). The main assumption of this technique is that the correlations of displacement phases between interferogram pairs are high (Samsonov et al., 2013). If the assumption is true, image stacking reduces unwanted contributions to phase and error terms, such as atmospheric effects and signal noise by averaging them out (Samsonov et al., 2013). The main issue with this technique, is that residual noise in the interferograms can often propagate through to the unwrapped phase (Khakim et al., 2013). To counter this, weights can be applied to the images, derived from temporal intervals between the images (Khakim et al., 2013; Ji et al., 2016).

Although the above-mentioned techniques have been shown to successfully increase the coherence of interferometric pairs, it is not guaranteed that the coherence of the images will be increased to an acceptable range. As perfect coherence values are not expected, it is reasonable to assume that pixels with coherence values of 0.35 – 0.45 or greater can be unwrapped to form reliable results (Samsonov et al., 2015). Of course, higher coherence values are still sought after as they translate to improved reliability of results.

2.6.3 Uncertainty in InSAR Measurements

Uncertainty in InSAR measurements are the result of phase decorrelation, orbital errors, topographic residuals, phase unwrapping errors and atmospheric contributions to phase (Hanssen, 2001; Fattahi & Amelung, 2015). Phase decorrelation ϕ_n, measured using coherence γ, is most impacted by temporal decorrelation, as physical changes to a surface between acquisitions affect it's scattering properties. Although phase noise in an interferogram cannot be mitigated without reducing the spatial resolution, selecting interferometric pairs with minimal temporal baselines can reduce the phase decorrelation and by extension, the uncertainty of the measurements. With precise orbital determination of modern satellites, the uncertainty from orbital errors ϕ_{orb} is small, having typical velocity uncertainties less than 0.5 mm/year over 100 km distance (Fattahi & Amelung, 2014). For older systems, this uncertainty increases to 1.5 mm/year over 100 km distance. The uncertainty from topographic residuals are inherently caused by errors in the reference DEM used for processing and spatial resolution differences to the SAR scenes. These residuals are then accentuated by temporal changes to the physical surface not reflected in the reference DEM. The topographic residuals can be corrected for by analyzing the interferograms as a stack in a time series (Ferretti et al., 2001; Berardino et al., 2002; Fattahi & Amelung, 2015). During phase unwrapping, uncertainty is introduced when phase noise is high, resulting in phase ambiguity, as discussed in Section 2.6. This can be mitigated by improving the coherence and masking out poor coherence pixels from the phase unwrapping.

Atmospheric phase contributions ϕ_{atm} caused by signal path delays mainly from changes in pressure, temperature and water vapor in the troposphere is the main source of uncertainty for InSAR measurements, resulting in uncertainty up to several centimeters (Fattahi & Amelung, 2015; Fárová et al., 2019). In some cases, the differential radar phase delay caused by atmospheric changes can be higher than those expected from surface deformations ϕ_{def} (Fárová et al., 2019). As with topographic residuals, uncertainty from atmospheric phase delays ϕ_{atm} can be mitigated by averaging stacked interferograms in a time series (Ferretti et al., 2001; Berardino et al., 2002; Hooper et al., 2007; Lazecký et al., 2010; Samsonov et al., 2013). As such, measurements of surface deformation, rather than simply an indication of a monitored phenomenon should be done using a stack of interferograms instead of a single interferogram (Fárová et al., 2019). Although atmospheric phase contributions are not correlated in time, as they randomly change between acquisitions, they are spatially correlated as temperature, pressure and humidity are continuous over large distances (Hanssen, 2001).

Being the main source of uncertainty for InSAR measurements, several techniques have been proposed to mitigate the effects of atmospheric phase contributions. Multi-temporal methods, such as PSI and SBAS apply spatial-temporal filtering to a time series of SAR scenes (Ferretti et al., 2001;

Berardino et al., 2002). Although increasing the number of acquisitions can reduce the uncertainty in velocity measurements, these low-pass temporal and spatial-temporal filtering approaches ignore the non-Gaussian distribution of the atmospheric delays, resulting in biased displacement time series and velocities (Fattahi & Amelung, 2015). This systematic bias is the result of atmospheric delays caused by seasonal variations and moisture in the atmosphere, which can be mitigated by using acquisitions separated by one year (Fattahi & Amelung, 2015). The displacement bias is most pronounced during the peak of seasonal cycles.

Onn and Zebker (2006) proposed interpolation of the atmospheric water vapor from GPS data to generate delay maps used to correct InSAR deformation measurements. Up to 31% of the uncertainty in InSAR measurements were corrected for using this technique, but the requirements of GPS network measurements make this technique not feasible in all study sites. Moderate Resolution Imaging Spectroradiometer (MODIS) observations from the Aqua and Terra satellites have also been used to estimate atmospheric signal delays through water vapor mapping techniques (Li et al., 2009; Fattahi et al., 2015). However, this technique is limited by daylight and cloud-free conditions, hindering a major advantage of SAR data.

Avoiding data limitations, Simons et al. (2002) estimated uncertainty caused by atmospheric delays by assessing the root mean squared (RMS) differences of the interferograms. The concept of this technique is based on *a priori* knowledge that the observed surface deformation is occurring very slowly so any high changes in RMS could be attributed to atmospheric signal delays. A similar technique is used by Tang et al. (2020), who used RMS as a measurement of the total uncertainty of velocity measurements from InSAR processing. Areas with large RMS values were determined to contain large errors, attributed to atmospheric or unwrapping errors, or non-linear deformations. Areas with little deformation and atmospheric effects had homogenous and low values for RMS. A more basic approach to this, is preforming a coherence-based analysis of the interferograms. Areas with low coherence are thought to be unreliable with high uncertainty (Xu et al., 2001; Ferretti et al., 2007; Khakim et al., 2013; Samsonov et al., 2015). However, this approach does not determine whether the loss in coherence is caused by interference or by an actual physical change to the surface. Therefore, this technique is only useful for determining pixels were the uncertainty is too high to be considered reliable but does not measure uncertainty of pixels with higher coherence.

2.7 DInSAR

Differential Interferometric Synthetic Aperture Radar (DInSAR) aims to isolate the phase contributions from surface deformation, ϕ_{def}, from the total phase. This phase information is converted into deformations or displacements in the slant range (Line-of-Sight) to measure minute surface

deformations. Differential Interferometric phase is expressed similarly to interferometric phase, as seen in equation 7, but also contains d, the relative scatterer displacement projected on the slant range direction (Ferretti et al., 2007). By adding this term, the interferometric phase can be expressed as:

$$\Delta\phi_d = \frac{4\pi}{\lambda}d \tag{Eq. 16}$$

As a result, the interferometric phase contains both altitude and motions contributions after interferogram flattening. Using an external DEM, the phase contributions from altitude can be removed from the interferogram, isolating the terrain motion component into a differential interferogram. As with traditional InSAR, the topographic phase contributions from altitude are caused by a non-zero $B_\perp$. The phase contributions from orbital errors ϕ_{orb} and the reference surface ϕ_{ref} are calculated and removed using the same process as traditional InSAR. The remaining phase then contains contributions from deformation ϕ_{def}, atmospheric noise ϕ_{atm} and other noise ϕ_n. Mitigation of unwanted signal contribution from noise is completed using the same techniques used for traditional InSAR, but this time attempting to isolate ϕ_{def} rather than ϕ_{topo}. However, even with mitigation, noise is expected to persist in the unwrapped phase as smaller perpendicular baselines are preferred for DInSAR but are more sensitive to noise from the atmosphere and other sources. Larger perpendicular baselines increase the spatial decorrelation caused by differences in viewing angles and contributions from topography.

The unwrapped phase from differential interferograms is converted to surface displacements in slant range using the following equation:

$$\Delta d_{LoS} = \frac{\phi_{unw}\lambda}{-4\pi} \tag{Eq. 17}$$

These displacement rates can then be converted into vertical displacements using simple trigonometry and the following equation:

$$\Delta d_v = \frac{\Delta d_{LoS}}{cos\theta_{inc}} \tag{Eq. 18}$$

Alternatively, the process can be simplified into a single step using the following:

$$\Delta d_v = \frac{\phi_{unw}\lambda}{-4\pi cos\theta_{inc}} \tag{Eq. 19}$$

Where ϕ is the unwrapped phase values, λ is the wavelength and θ_{inc} is the line-of-sight-to-vertical factor.

DInSAR is limited to measuring very small and very large deformation gradients (Massonnet and Feigl, 1998 as cited in Samsonov $et\ al.$, 2015). The theoretical maximum displacement that can be measured using DInSAR is related to residual orbital and atmospheric noise, coherence and wavelength (Samsonov et al., 2015). The main factor driving the theoretical maximum limit is caused by phase

ambiguity and is directly related to the wavelength. This theoretical maximum displacement that can be measured is defined as the follow:

$$d^0_{max} = \frac{\lambda}{2x},$$

(Eq. 20)

Where d^0_{max} is the theoretical maximum detectable deformation, λ is the SAR wavelength and x is the SLC sample spacing. However, the real maximum displacement is always smaller than the theoretical value and is coherence dependent. The main difference between theoretical and real maximum displacements is the result of atmospheric and residual orbital noise (Samsonov et al., 2015). The real maximum displacement that can be measured using DInSAR is defined as follows:

$$d_{max} = d^0_{max} - 0.002(1 - \gamma)$$

(Eq. 21)

The real minimum displacement that can be measured is also dependent on coherence and is defined as:

$$d_{min} = 0.00007(1 - \gamma)$$

(Eq. 22)

As multilooking decreases the spatial resolution of the interferograms, the theoretical maximum detectable gradient is also decreased. Similarly, filtering the interferogram reduces signal spatial resolutions and can make phase unwrapping in areas of large gradients impossible (Samsonov et al., 2015).

2.8 Multi-temporal DInSAR

Multi-temporal DInSAR techniques are used to overcome the limitations of DInSAR caused by geometrical decorrelation and atmospheric artefacts (Tang et al., 2020). By mitigating against these decorrelations, the real maximum displacement that can be measured is increased. By improving the coherence of interferograms, the minimum displacement that is detectable is also improved, allowing for millimeter-scale displacements over long periods of times. Two prominent multi-temporal DInSAR techniques include persistent scatterer InSAR (PSI) (Ferretti et al., 2001; Hooper et al., 2007) and small baseline subset (SBAS) (Berardino et al., 2002). Between these two methods, the primary difference is the type of scatterer that is being measured. PSI, as the name implies, aims to detect persistent in-scene scatterers, whereas SBAS is used to detect distributed scatterers. Persistent scatterers are defined as point-wise deterministic objects containing single point scatterers whose phase remain stable over long time periods and dominate a pixel's SAR response (Hooper et al., 2007; Ferretti et al., 2011; Pawluszek-Filipiak & Borkowski, 2020). Distributed scatterers correspond to pixels belonging to areas of moderate coherence in some interferometric pairs of the data set, where many neighbouring pixels share similar reflectivity values (Ferretti et al., 2011; Pawluszek-Filipiak & Borkowski, 2020). These targets usually correspond to debris areas, non-cultivated lands with short vegetation and desert areas.
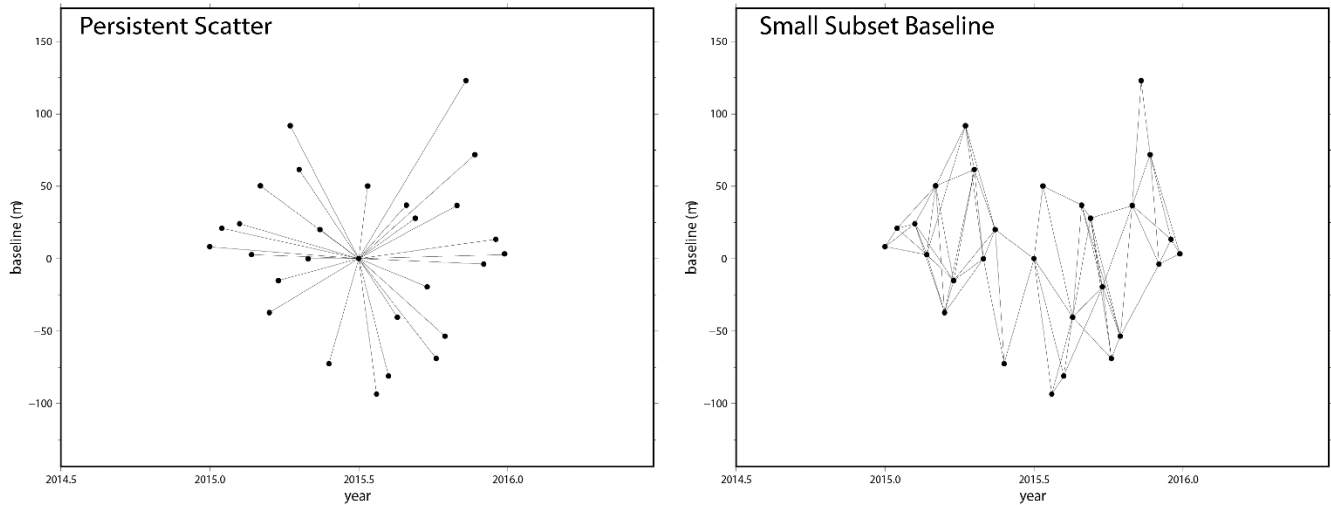
Figure 6. Visualization of the interferometric pairs (connecting lines) formed by PSI (left) and SBAS (right) using the same data. The x-axis shows the temporal baselines between acquisitions and the y-axis shows the perpendicular baselines between acquisitions.

The other major difference between PSI and SBAS is how they handle creating interferometric pairs. PSI uses a single master that all slave images are paired to. This image should be chosen to minimize the cumulative temporal and perpendicular baselines of the data set. Generally, this means picking an image that is approximately half the study's time period from the start date and a perpendicular baseline which is about average for the dataset. As a result, there are N – 1 interferograms created from a dataset, where N is the total number of scenes. Taking a different approach, SBAS aims to create as many interferometric pairs as possible given some user defined thresholds applied to both the temporal and perpendicular baselines. Although there is no consistent master for all pairs, a super master is still selected as the reference for co-registration and deformation calculations in the end steps. As a result, this process generates many more interferometric pairs than PSI. A visualization of how the two techniques form interferometric pairs can be seen in figure 6.

2.8.1 PSI

Persistent Scatter InSAR aims to identify coherent radar targets within a series of interferograms that exhibits high phase stability across the entire time period of observations. These targets should only be slightly affected by temporal and geometrical decorrelations, often point-wise scatterers characterized by high reflectivity values generated by dihedral reflection or simple (deterministic) single-bounce scattering (Ferretti et al., 2011). Examples of such scatterers include human-made structures, boulders and outcrops. As such, PSI is particularly reliable when monitoring urban areas characterized by a high density of point-wise stable targets in the form of man-made structures. Conversely, PSI struggles to provide high-quality and reliable measurements over non-urban areas characterized with a high density

of distributed scatterers (Ferretti et al., 2011). Persistent scatterers have properties independent of their associated amplitudes and therefore can be used to reliably measure deformation in areas of high decorrelation, assuming at least a few persistent scatterers are available (Hooper et al., 2004). Atmospheric and orbital artifacts are estimated and removed from the total interferometric phase based on the space-time information available (Ferretti et al., 2001).

PSI techniques were first developed by Ferretti et al. (2001) and developed further by Hooper et al. (2004) to create the Stanford Method for Persistent Scatterers, or StaMPS. The original methodology developed by Ferretti et al. (2001) used permanent scatterers, rather than persistent scatterers, and used amplitude information to identify stable scatterers. Hooper et al. (2004) improved upon the original PSI methodologies with its ability to select PS pixels independently of their amplitude values, opting to select pixels based on spatial correlation of phase. A minimum of 5 acquisitions are required for StaMPS processing and selected pixels are combined within patches, with each patch being processed independently (Hooper, 2008). As such, StaMPS has improved capability over non-urban areas but still struggles to match the capability over urban areas. This process results in high omission rates for pixels, with selected pixels having a high reliability of surface displacement measurements. It should be noted that as PSI utilizes a single common master, it is common for some interferometric pairs to have large baselines (sometimes greater than the critical baseline) and thus suffer from baseline decorrelation (Berardino et al., 2002). As a result, PS density can be rather low as the scatterers do not maintain sufficiently high coherence values in all interferograms, specifically over non-urban areas. The methodology of selecting appropriate PS pixels and using these pixels to estimate surface deformations is described in Section 4.1.

2.8.2 SBAS

Small subset baseline techniques, first developed by Berardino et al. (2002), are the most extensively used techniques in research (Pawluszek-Filipiak & Borkowski, 2020). SBAS methods aim to increase the temporal sampling by using all acquisitions included in different small baseline subsets and to preserve the capabilities of the system to provide spatially dense deformation maps (Berardino et al., 2002). The latter requirement is a key issue of traditional DInSAR and is directly related to the use of small baseline interferograms that limit the baseline decorrelation within each interferogram. To mitigate the baseline decorrelation of interferograms, small baseline methods attempt to minimize the perpendicular, temporal and Doppler baselines, a key improvement compared to other multi-temporal DInSAR techniques (Hooper, 2008; Pawluszek-Filipiak & Borkowski, 2020). This process however does not benefit from two potential benefits of other multi-temporal DInSAR methods. These benefits are the

capability to process data at the highest possible resolution and to unwrap phase robustly in three dimensions, the third being time (Hooper, 2008).

SBAS techniques rely on using an appropriate combination of many small baseline interferograms, based on user defined thresholds (Lauknes et al., 2006). Given some thresholds applied to the perpendicular and temporal baselines, all combinations of interferometric pairs within these thresholds are generated. These interferograms are first multi-looked and then individually unwrapped (Hooper, 2008). DEM errors are mitigated as a topographic error estimation is incorporated into the standard SBAS method to improve robustness (Berardino et al., 2002; Lauknes et al., 2006). This is accomplished by estimating the low-pass displacement parameters using an external DEM (Berardino et al., 2002). When no *a priori* knowledge is available, a simplified linear, constant-rate model of phase variation in time is commonly applied (Pawluszek-Filipiak & Borkowski, 2020). It should be noted that this relationship does not hold true when measuring mining-related subsidence. Instead, a high non-linear trend is expected (Pawluszek-Filipiak & Borkowski, 2020). Similarly to PSI, atmospheric and orbital artifacts are estimated and removed based on the space-time information (Berardino et al., 2002; Lauknes et al., 2006). The methodology of creating these small baseline interferograms and stacking them to estimate deformation rates is outlined in Section 4.2.

2.8.3 Measuring Land Subsidence using Multi-temporal DInSAR

Multi-temporal DInSAR techniques have been successfully used to monitor slow moving land surface deformation. Lauknes et al. (2006) compared SBAS results of subsidence monitoring in Oslo, Norway to geodetic measurements and external PSI results using ERS data. Over the 1992-1999 period, a maximum subsidence rate of over 5 mm/year was detected, which agreed well with the geodetic data. Although the pattern of deformation measured using SBAS was nearly identical to the pattern observed in the external PSI results, the actual measured velocities significantly differed between the two sets of results. A similar behavior was observed by Lazecký et al. (2010) when comparing PSI and SBAS results to leveling data when monitoring land subsidence caused by mining activities. The maximum deformation rates measured in this study were -40 mm/year and 44 mm/year. In this case, the PSI and SBAS measurements were shown to heavily underestimate subsidence rates when compared to the surveying data but showed very similar spatial patterns of deformation. Because of this relationship, Lazecký et al. (2010) determined that multi-temporal DInSAR measured were best suited for coarse estimates of subsidence rates and for detecting the presence of subsidence and epicenters of subsidence rather than providing accurate measurements. Extending the temporal range of the study was attempted to increase the confidence of the estimates but resulted in a large loss of data due to decreased coherence.

More recently, deformation estimates from PSI were compared to traditional DInSAR results using Sentinel-1 data to monitor highway stability following a landslide in the Czech Republic by Fárová et al. (2019). These measurements were validated using in-situ geodetic measurements, 3D inclinometers and laser scanning. They found that the PSI measurements corresponded very well with the in-situ measurements over areas of high coherence and could provide a detailed insight to the land deformation process. Comparatively, the traditional DInSAR techniques were simpler to implement, but could only reliably be used to prove the existence of a deformation rather than measure it. Both techniques proved to be reliable at determining vertical displacement hotspots, with rates up to 20 mm/year, and spatial patterns of surface deformation, even over some densely vegetated areas. A similar study, comparing traditional DInSAR to multi-temporal DInSAR was completed by Pawluszek-Filipiak and Borkowski (2020) to monitor land subsidence caused by underground coal mining in Poland. This time, the DInSAR measurements were compared to SBAS estimates and validated using leveling data. The fast displacement and high nonlinearity of the deformation made accurate measurements challenging. Although this study used a large amount of SAR images, 106 in ascending and 107 in descending orbits, the SBAS technique failed in areas of maximum subsidence rate. The combination of ascending and descending imagery allowed for both vertical and horizontal displacements to be measured. This technique showed a maximum subsidence rate up to -1 m/year and showed good agreement between the DInSAR and SBAS results. It was concluded that accuracy should not be worse than 40 mm/year using this approach. With RMSE values ranging from 9 mm to 32 mm/year when compared to leveling data, DInSAR was deemed as a cost-effective method that could be used complementary to conventional geodetic techniques. Although able to fill measurement gaps and provide reliable monitoring, DInSAR was not suggested as an ideal stand-alone technique for deformation monitoring.

Deformation measurements from SBAS techniques were compared over urban and rural areas by Chaabani and Deffontaines (2020) using Envisat ASAR and Sentinel-1 imagery. The Envisat data was used to measure subsidence from 2003 – 2007 while Sentinel-1 was used to measure deformation from 2016 – 2018 over Tunis City and the Mornag Plain. Subsidence rates up to 14 mm/year and 19 mm/year were measured using Envisat and Sentinel-1, respectively. As surface deformation here was mainly attributed to by excessive groundwater pumping, the measurements were validated using piezometric data which showed a good relationship in areas of high coherence. SBAS was shown to be effective at monitoring displacement with multi-millimeter accuracy in both urban and semi-urban areas, if the vegetation coverage allowed it. Liu et al. (2020) preformed a similar multi-platform SBAS study to monitor urban subsidence of the Beijing Plain using 47 Envisat and 24 Radarsat-2 imagery. Once again, the main cause of subsidence was over exploitation of ground water pumping, sometimes with a delay

between water pumping and land surface response. The two sets of multi-temporal DInSAR results showed similar spatial patterns and consistent trends of deformation with varying measured rates. This is the same behavior observed in the previously mentioned studies. Both sets of results were validated using leveling data, showing an RMSE of 1.15 mm/year and a good agreement of deformation patterns, demonstrating a strong effectiveness of the technique in the region.

Anderssohn and Riedmann (2014) suggested using bi-static and monostatic TanDEM-X data to monitor land surface deformation of the Garzweiler open-pit mine in the Rhenish coalfields using SBAS. The usage of SBAS was suggested over PSI due to the improved capability of SBAS to measure non-linear surface deformations over PSI. This is likely caused by the image pairing processing of SBAS allowing measurements to be made between all pairs independently rather than from a single master date. It was determined that an accurate DEM had a crucial impact on the quality of surface movement measurements, especially over the mining pit itself, which made accurate measurements challenging. To combat this, CoSSC data from TanDEM-X can be used to generate high quality DEMs over the region and used as a reference surface during the SBAS processing. This mitigates a significant portion of unwanted signal contributions attributed by the reference surface, ϕ_{ref}.

Following this work, Tang et al. (2020) used a coherence based SBAS approach to monitor mine stability in the Rhenish coalfields using a multiplatform approach. This study used three stacks of SAR images of ascending and descending imagery from TerraSAR-X and Sentinel-1 to measure vertical and horizontal displacements within and around the mining pits. The small perpendicular baselines of Sentinel-1 showed to cause a very small DEM error in the deformation results, when over the continuously changing surface topography of the mining pit. However, the vegetation coverage in the region resulted in a large loss of coherence due to the short wavelengths of the systems used. Although the TerraSAR-X results were more sensitive to slow and small displacements and had a higher spatial resolution, providing more detailed information about ground deformation, it suffered more heavily from temporal decorrelation. Surface deformation rates up to 500mm/year, 380 mm/year and 310 mm/year were observed around the Hambach, Garzweiler and Inden mines, respectively. Although the compaction process of waste materials was shown to be the main contributor to land subsidence, a distinct relationship between ground water pumping and surface deformation in the area was identified. Significant land subsidence was also measured in storage/recultivation areas caused by the compaction process of unconsolidated soil materials. Additionally, surface uplift was found near active working parts of the mine due to the excavation process. Tang et al. (2020) determined that a coherence based SBAS approach could be used for not only for the identification of unstable areas but also for forecasting slope failures and landslides. However, it was discussed that this technique is limited by requiring a large

number of multi-temporal images for processing and may conflict with rapid responses for early warning system frameworks.

Although Tang et al., (2020) were able to successfully measure surface deformation around the Rhenish coalfields, they did so using a coherence-based SBAS technique with Sentinel-1 and TerraSAR-X data. This study aims to assess the capabilities of using conventional SBAS and PSI using only Sentinel-1 data to measure surface deformations around the Rhenish coalfields and compare the performance between the two techniques. By using only Sentinel-1 data, the impact of temporal decorrelation between image acquisitions is emphasized. The Rhenish coalfields are chosen as the study area due to the large coverage and availability of Sentinel-1 data. Additionally, the mixture of hard (built-up areas) and soft (agricultural fields) targets present a great opportunity to evaluate the differences between the PSI and SBAS approaches. This helps demonstrate the conceptual differences between the two techniques, as PSI focuses on measuring deformation of only hard and persistent targets while SBAS aims to provide full coverage of deformation results, focusing on soft and distributed scatterers.

Chapter 3

Data

3.1 Rhenish Coalfields

The Rhenish coalfields are in the German's most populated state of North Rhine-Westphalia, west of Cologne. This coalfield is operated by RWE Power AG to extract lignite (also known as brown coal) from three large open-pit mines – Hambach, Garzweiler and Inden, as seen in figure 7. Mining operations begun in the area over 100 years ago and currently has an operating size of 9,000 ha (as of 2017) with a total annual capacity of 120 million tonnes of lignite (Tang et al., 2020). The area surrounding the mining pits is relatively low-lying terrain with a hill range to the south-west. Together, the three mines provide coal to supply coal-fired power stations that meet approximately 40% of the power requirements for North Rhine-Westphalia.
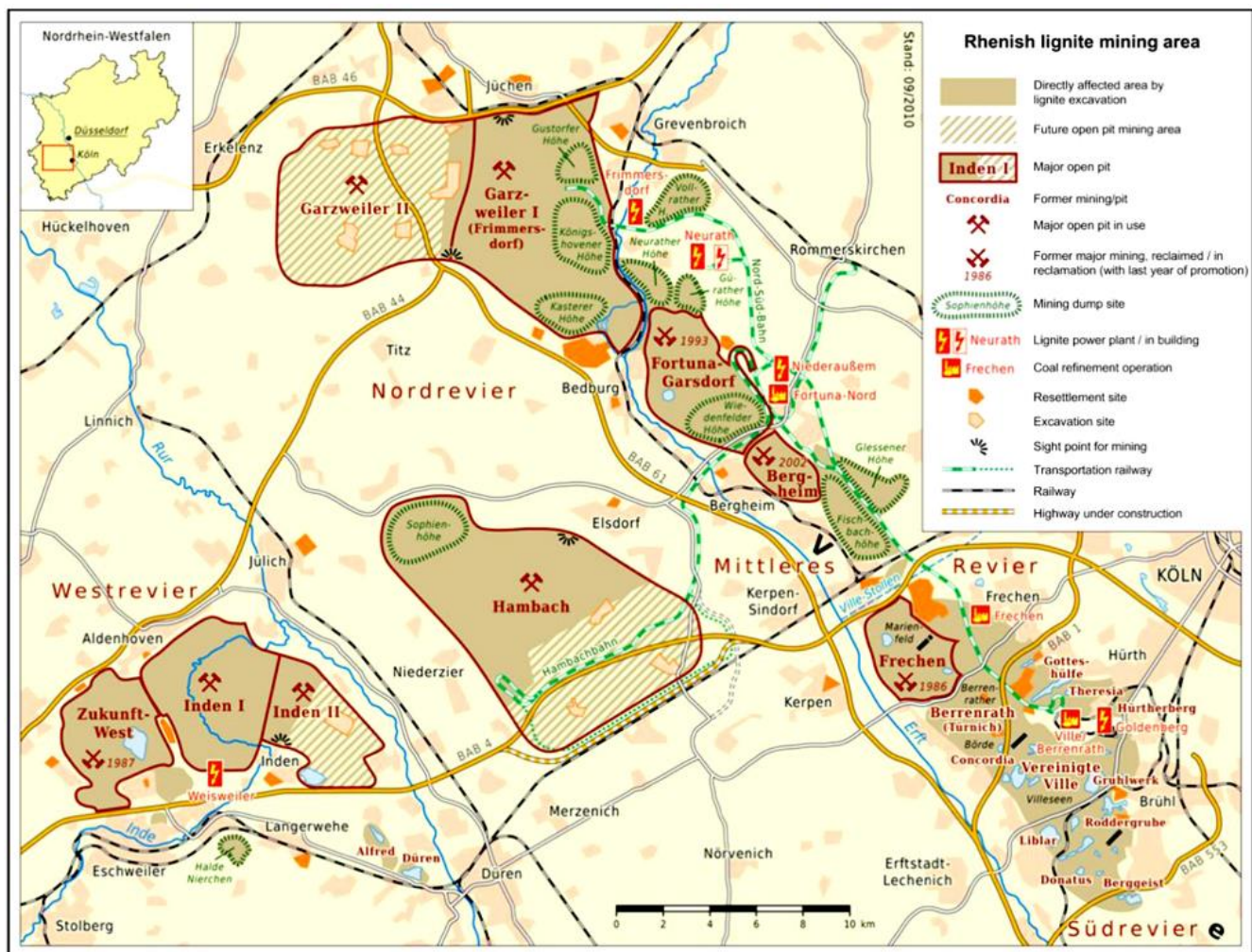
Figure 7. Overview of the Rhenish Coalfields with the Hambach, Inden and Garzweiler open-pit mines (Tang et al., 2020).

Of these three, Hambach is the largest mine with an operating size of 4,380 ha, approved up to 8,500 ha. It began operation in 1978. This operation has an annual coal production of 40 million tonnes and a capacity of 1,350 million tonnes. To make way for the mining activities, the 5,500 ha Hambach forest was cut down to 1,100 ha and is further threatened by mining exploration (Donahue, 2018, as cited in Tang et al., 2020). Alongside heavy deforestation, small villages were relocated to make space for the expanding mining operation. The bottom of the pit is 293 meters below sea level, or 399 meters below ground surface, forming an artificial repression in North Rhine-Westphalia (Tang eta al., 2020). A notable landmark of the Hambach pit is the Sophienhöhe hill, the world's largest artificial hill, made from mining spoil.

South-west of Hambach lies the Inden open-pit mine. The mine has an operating size of 1,700 ha and a coal capacity of 260 million tonnes. Supplying 20 million tonnes of lignite annually, the Inden mine is the primary supplier for the nearby Weisweiler power plant, generating about 2,000 MW of power for the state. Garzweiler mine, situated north of Hambach, has an operating size of 3,200 ha and an annual production of 35 million tonnes. The operation is divided into two sectors, the eastern Garzweiler I and the western Garzweiler II. The remaining area is filled with wind farms and large areas of farmland, which were re-established as part of the recultivation.

The Hambach and Garzweiler mines are expected to continue operation until 2045 while the Inden mine is expected to operate until 2030. Once the Inden mine is exhausted, the adjacent lignite power plant will also end operations. Following these closures, RWE Power AG will begin the landscape reclamation and remediation processes. These processes including flooding Hambach to create a 4,000 ha lake, flooding Inden to become an 1,100 ha lake and repurposing Garzweiler into new agricultural land.

3.2 Sentinel-1 Data

To evaluate the capability of InSAR time series methods to estimate land deformation, two stacks of Sentinel-1 images were collected for 2015 and 2016. 29 images in ascending geometry for 2015 and 35 images in ascending geometry for 2016 are used. The increased number of scenes for 2016 is the result of the Sentinel-1B satellite launch. VV polarization was used due to its sensitivity to rough surface scattering, improving land surface detection. All images are acquired in Level-1 Single Look Complex (SLC) IW mode with pixel spacing of 2.3 meters by 14.1 meters and a swath width of 250 km. To be compatible with InSAR processing, all images within a dataset must be acquired along the same track. In this step, images are not discriminated against based on perpendicular or temporal baselines. The short repeat period of the sensor (12 days) increases the ability to monitor deformation surrounding mining areas with low temporal decorrelation. Despite this, the non-coherent nature of the mining operation

causes even this small temporal difference to create a loss of coherence too high to accurately assess deformation within the mining operation using repeat-pass imagery. Additionally, there remains significant loss of coherence due to the scattering of the short wavelength (λ = 5.6 cm) within dense vegetation surrounding the region. Appendix A and B list the radar images used in this study. An example of a SLC SAR image is shown in Figure 8.
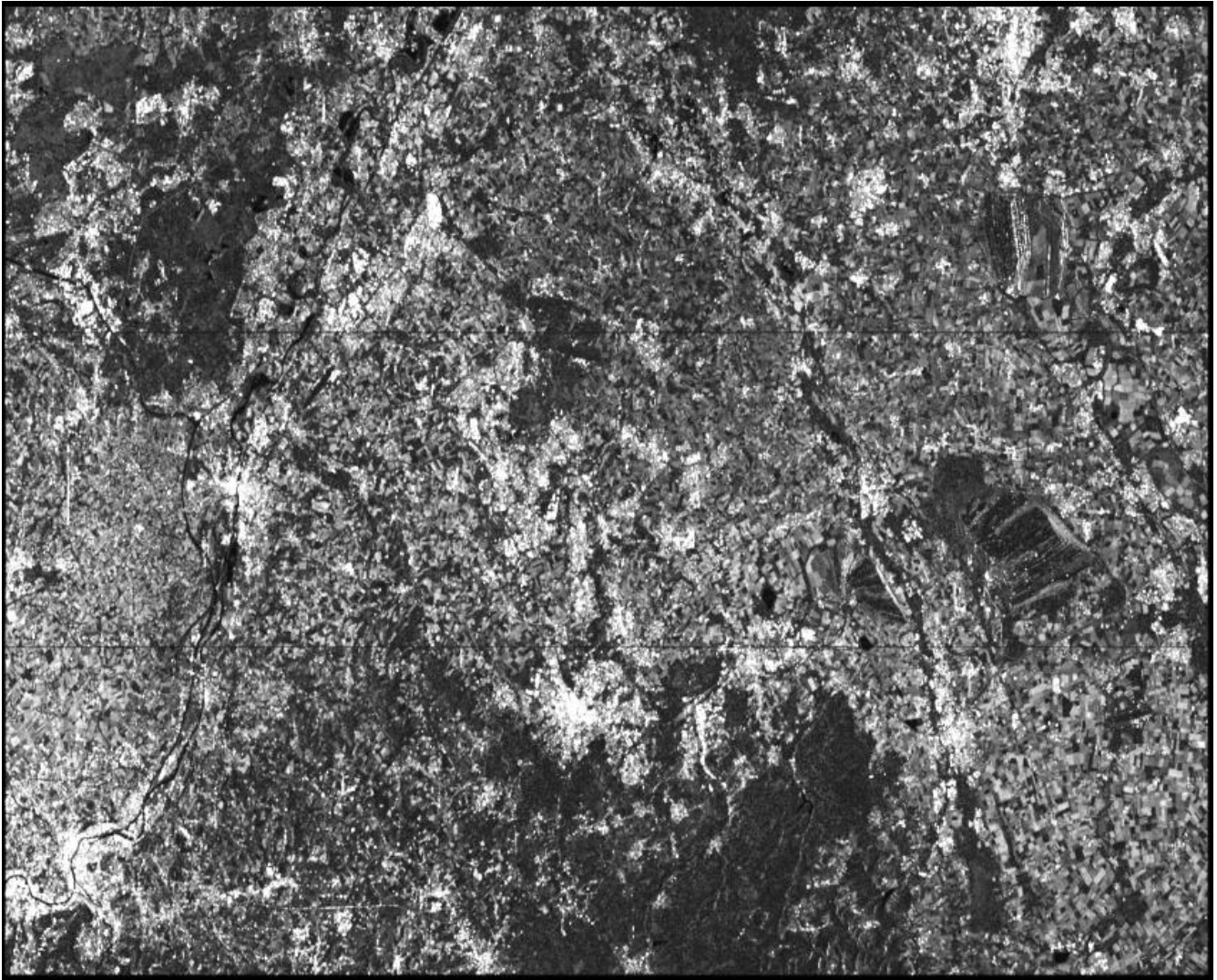
Figure 8. SLC SAR amplitude image acquired using Sentinel-1 over the Rhenish Coalfields.

3.3 Land Cover Data

The land cover dataset used was acquired from the CORINE Land Cover (CLC) inventory. This dataset was initiated in 1985 under the Copernicus program with updates produced in 2000, 2006, 2012 and 2018. As the 2012 update was created to show land cover during 2011 and 2012, while the 2018 update showed land cover for 2017 and 2018, the 2018 CLC product was used due to its temporal proximity to the study period. Unlike previous updates, the 2018 product is classified using Sentinel-2 and Landsat-8 imagery and has a geometric accuracy of less than 10 meters. This dataset uses a minimum

32

mapping unit of 25 ha, consists of 44 classes, has a thematic accuracy greater than 85% and a spatial resolution of 100 meters by 100 meters. These 44 classes were aggregated into a binary urban and non-urban land cover dataset which was later used to assess InSAR capabilities over favorable urban land cover. The 2018 aggregated land cover for the study area is shown in figure 9. The list of aggregated classes is shown in Appendix C.
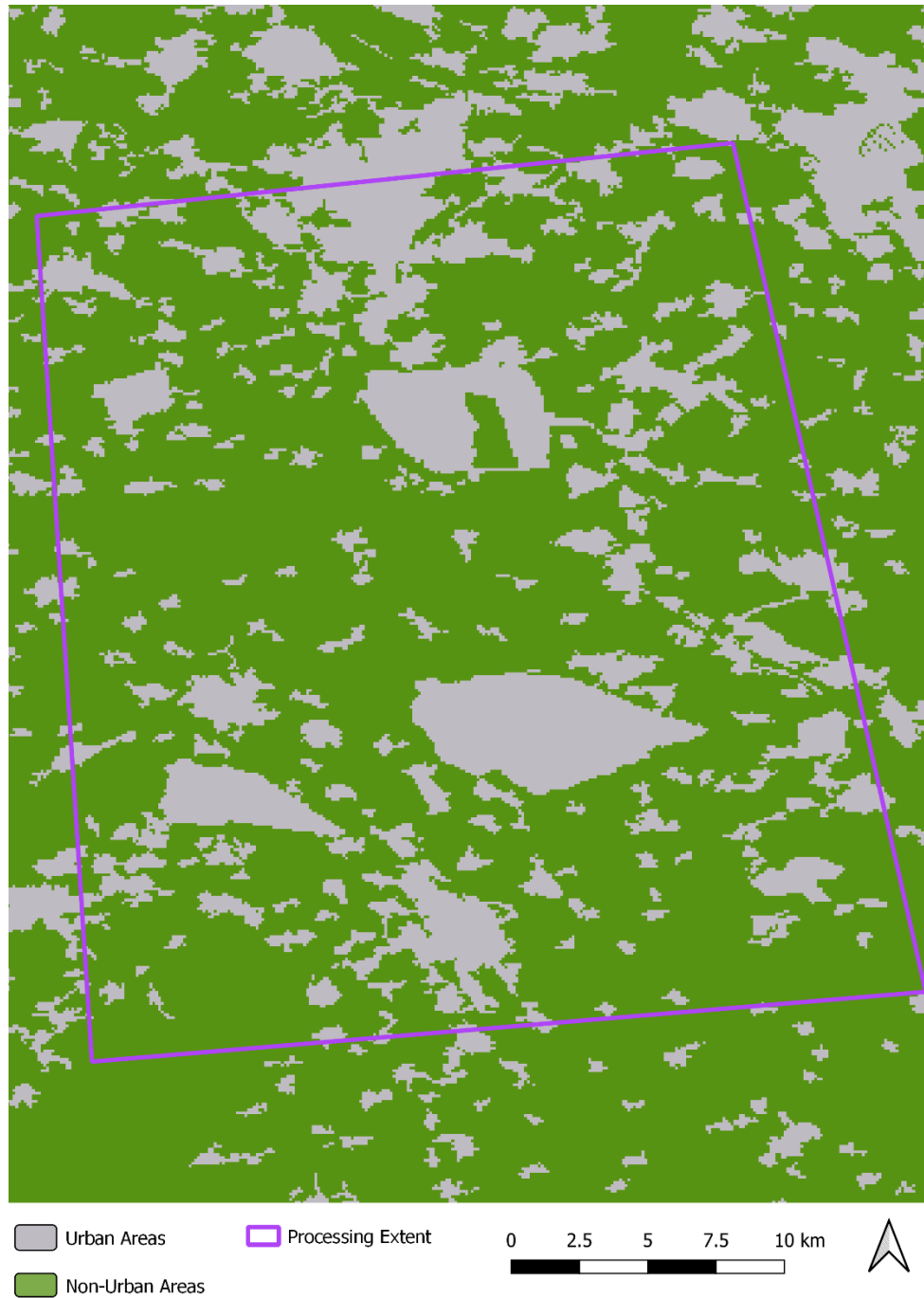
Figure 9. Landcover usage of the study area, classified using the 2018 CLC product

3.4 GNSS Data

Global Navigation Satellite System (GNSS) station data was collected from the EUREF Permanent GNSS Network. This network operates under the International Association of Geodesy (IAG) Regional Reference Frame sub-commission for Europe. It consists of continuously operating GNSS reference stations, data centers providing access to the station data, centers that analyze the GNSS data and a Central Bureau responsible for the daily monitoring and management of the network. The purpose of the network is to provide access to the standard precise GNSS coordinate system used throughout Europe, the European Terrestrial Reference System 89 (ETRS89). The ETRS89 is the foundation for geolocation data on the European territory, on both national and international levels. All contributions to the network are provided on a voluntary basis with over 100 European agencies involved.

As only one of the GNSS stations are within the study region, this station and two nearby stations were selected to evaluate land deformation rates estimated using DInSAR time series analyses. These stations include: Titz, Euskirchen and Eijsden. The locations of these stations used are shown in figure 10. Data were downloaded using a script to collect hourly and daily positional data for each station formatted in a compressed RINEX file. Positional data are stored in decimal degrees for latitude and longitude and meters, relative to ellipsoidal height, for the height. As the hourly height measurements recorded by each station have a relatively high uncertainty, up to 3 cm (NovAtel Inc., 2015), deformation rates were assessed as an annual average velocity from 2014 to 2020 hourly and daily data. While six years of data were collected for the Euskirchen and Eijsden stations, 2014 data was unavailable for the Titz station and only 2015 – 2020 data could be used for this station. In total, 2545 dates were used for Eijsden station, 2483 dates were used for the Euskirchen station and only 2161 dates were used for the Titz station.
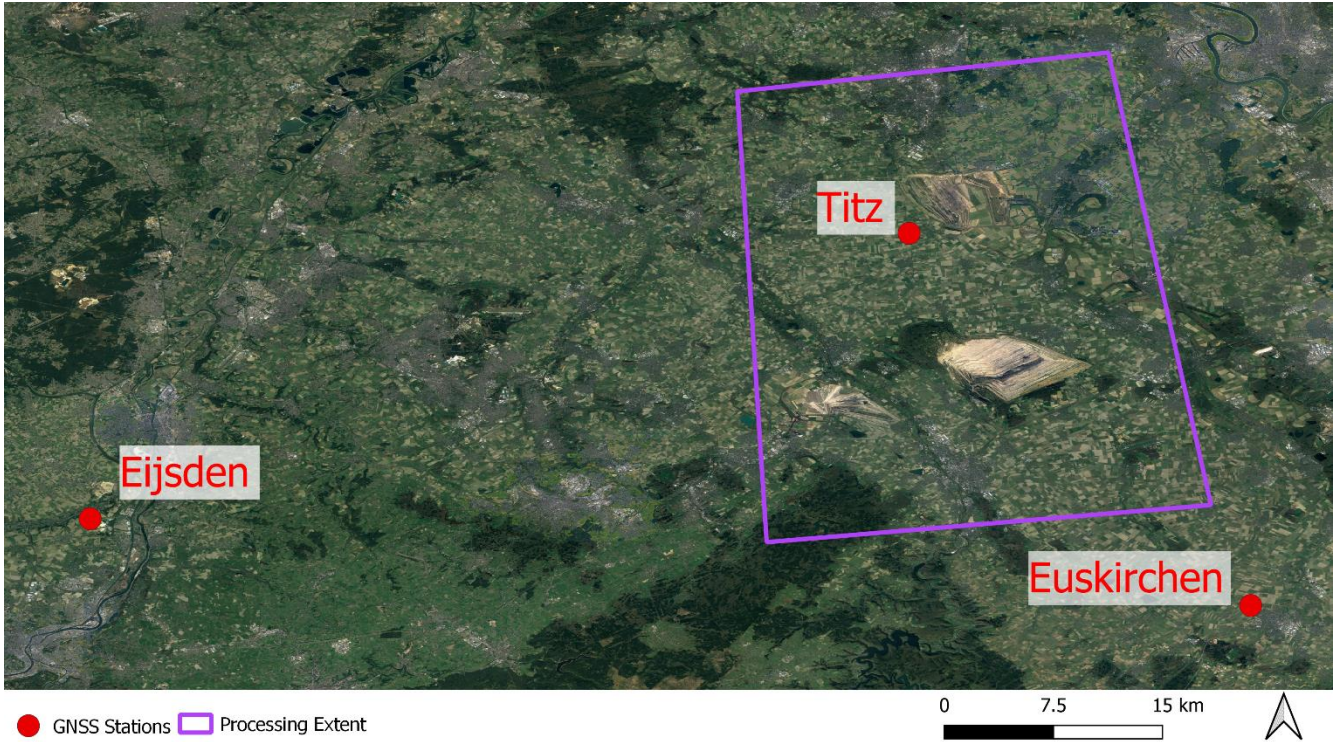
Figure 10. Overview of the three GNSS station locations in the context of the processing extent used in this study.

Chapter 4

Methodology

The processing completed in this study uses a combination of Persistent Scatterers Interferometry (PSI) and Small Baseline Subsets (SBAS) algorithms. Processing for PSI was completed using StaMPS, and SBAS was completed using GMTSAR, with phase unwrapping for both being handled by SNAPHU. Preprocessing of data for PSI was completed using SNAP and the snap2stamps package. Combination of these techniques allows for coherence optimization of individuals interferograms through SBAS while focusing on high-quality pixels selected through PSI. These measurements were later validated by processing GNSS data of three nearby stations and comparing these to the InSAR results.

4.1 Persistent Scatter
4.1.1 Pre-processing

Persistent scatterer interferometry aims to identify pixels with spatially and temporally stable phase throughout the dataset with reference to a master image (Hooper et al., 2007; Ferretti et al., 2011). An optimal master image is selected such that the summation of perpendicular and temporal baselines across all interferometric pairs within the dataset are minimized. By minimizing the total baseline differences between the master images and all the slave images, the average coherence of targets within the scene increases and the phase appears to be more stable. This is achieved by reducing the average change experience by a target in the master-slave image pairs by reducing the average temporal baselines between image pairs, resulting in reduced temporal decorrelation. The coherence is further increased by reducing the perpendicular baselines and therefore the geometrical differences of a target between the master and slave images. Generally, this is completed by selecting an image that was acquired about halfway into the time span of the dataset and with a perpendicular baseline that is about average for the dataset. Selecting a suboptimal master image creates a large loss of coherence within the dataset, leading to higher pixel omission rates, lower confidence in results and longer processing times. Considering this, selecting an optimal master image is a crucial step that impacts the quality of the entire dataset during processing and analysis.

Since the data in this study is split into two datasets, one for each year, two master images are selected. For 2015, data acquired on July 2nd is used as the master image and data from August 1st is selected as the master image for 2016. The master image selections and the resulting interferogram pairs can be seen in figure 11. Once selected, the master images are split and subset around the study area containing a VV polarization. Using the split master images, orbital corrections are applied to all the slave images. During this step, the slaves are split to only contain VV polarized data and to match the spatial coverage of their respective master images.

36

Each split slave image is then co-registered to their respective master images to spatially align the two. This allows features on the Earth's surface to correspond with overlapping pixels in the master-slave image pairs and for the change in a pixel to show change to the feature. This process requires common features to be identified in both images and their locations to be stored as tie points. The slaves are then warped using a polynomial function to align their tie points to those of the master image. Although accurate, a perfect overlap of feature footprints is often not possible. This misalignment may result in incorrect temporal profiles and show change to a pixel not representative of change to a feature. Generally, image co-registration selects a master image based on optimal parameters from the image metadata. This master selection process is superseded by selecting a master image for entire dataset. This may result is sub-optimal image co-registration for some pairs within the dataset. This entire process is handled by the snap2stamps software package.

As the image pairs are co-registered, the interferometric phase is generated and stored in interferograms. These interferograms are generated by cross-multiplying the master image with the complex conjugate of the slave image at the pixel level (Ferretti et al., 2007). The resulting interferogram contains amplitude values which are the product of the master and slave amplitude values, and interferometric phase equal to the difference of phases between the two images (Ferretti et al., 2007).
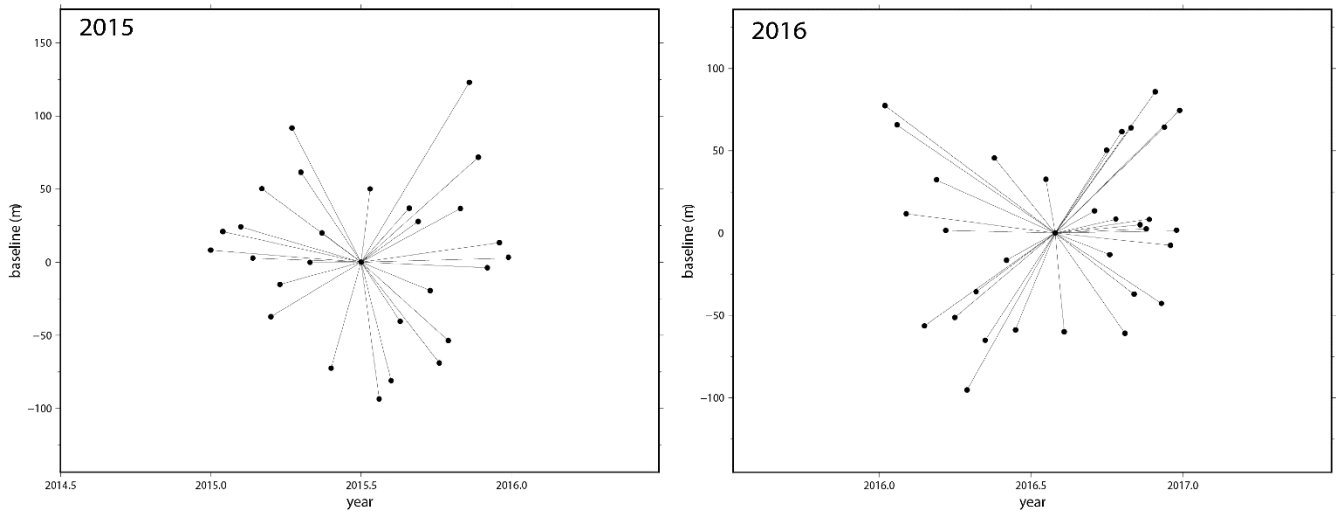
Figure 11. Visualization of the interferometric pairs (connecting lines) formed by PSI for 2015 (left) and 2016 (right) using the master dates of July 2nd, 2015 and August 1st, 2016. The x-axis shows the temporal baselines between acquisitions and the y-axis shows the perpendicular baselines between acquisitions.

The resulting phase information ($\delta\varphi$) contains contributions from viewing the topography from different angles ($\delta\varphi_{topo}$), orbital errors and flat earth corrections ($\delta\varphi_{orbit}$), changes in the distribution of tropospheric water vapor between radar acquisitions ($\delta\varphi_{atm}$), changes to the scattering mechanisms

of a target on the Earth's surface ($\delta\varphi_{pixel}$) and ground surface movements ($\delta\varphi_{defo}$) (Ebmeier et al., 2012). As such, the total interferometric phase is given by:

$$\delta\varphi = \delta\varphi_{topo} + \delta\varphi_{orbit} + \delta\varphi_{atm} + \delta\varphi_{pixel} + \delta\varphi_{defo} \qquad \text{(Eq. 23)}$$

Often, the topographic phase contributions dominate the measured phase shift and need to be removed to isolate phase contributions from surface deformation. In this case, SRTM-3 data are used as an external reference DEM to calculate and subtract the topographic phase from the total phase. Any empty interferograms are omitted from the study at this step. Once the interferograms are generated, they are divided into patches to avoid memory problems and converted to a StaMPS compatible format.

4.1.2 StaMPS
The PS processing is completed using StaMPS software using scripts written in Matlab. This PS process is performed in the 8 steps: 1. Initial PS candidate selection 2. Estimating phase noise and temporal coherence 3. PS Selection 4. PS weeding 5. Phase corrections 6. Phase unwrapping 7. Estimating and filtering nuisance terms (spatially correlated look angle errors and atmospheric noise) 8. Calculating deformation rates.

4.1.2.1 Initial PS Candidate Selection
Pixels are preselected for phase analysis based on their amplitude dispersion index D_A which describes the amplitude stability of a pixel. The amplitude dispersion index is given by:

$$D_A = \frac{\sigma_A}{\mu_A} \qquad \text{(Eq. 24)}$$

Where σ_A is the standard deviation of amplitude values and μ_A is the mean amplitude. As the threshold increases, more pixels will be preselected for phase analysis. Surfaces such as water or vegetation tend to have higher D_A values than man-made structures (Ferretti et al., 2001; Hooper et al., 2007). Although a recommended range for D_A is $0.4 - 0.42$, these values led to oversampling of pixels within the datasets. As a result, a D_A threshold of 0.3 is used to discriminate pixels for the phase analysis, reducing the total noise observed during processing. For 2015, there were 257,782 PS candidates selected, and 145,727 PS candidates selected for 2016.

4.1.2.2 Phase Stability Estimates
To obtain temporal coherence and determine phase stability, the spatially correlated phase is estimated and subtracted. The wrapped phase ($\psi_{x,i}$) of the xth pixel in the ith flattened interferogram can be written as the sum of 5 terms: phase change due to movement in the satellite line-of-sight ($\phi_{D,x,i}$), residual phase due to look angle error ($\Delta\phi_{\theta,x,i}$), atmospheric delays ($\phi_{A,x,i}$), orbital inaccuracies ($\Delta\phi_{S,x,i}$)

and a noise term ($\phi_{N,x,i}$) which considers variable scattering, thermal noise and co-registration errors. This equation is given as:

$$\psi_{x,i} = W\{\phi_{D,x,i} + \phi_{A,x,i} + \Delta\phi_{S,x,i} + \Delta\phi_{\theta,x,i} + \phi_{N,x,i}\} \qquad \text{(Eq. 25)}$$

Using this, the noise is then estimated by using a combined low-pass and adaptive phase filter based on the Goldstein phase filter and removed for each pixel (Hooper et al., 2007). The pixels are filtered with a 50-meter grid spacing and a filter window size of 32 by 32 pixels. To improve accuracy, this filtering is iterated over each interferogram until a mean noise value (γ) change threshold is reached. In this study a γ change threshold of 0.005 is used resulting in 234,384 PS candidates for 2015 and 144,112 PS candidates for 2016.

4.1.2.3 PS Selection

Pixels most likely to be PS pixels are selected based on their noise characteristics using a probability analysis. With a correlation between amplitude variance and phase stability, the probability of a pixel being a PS can be accurately calculated by considering both the phase stability (γ) and the amplitude dispersion (D_A) of the pixel (Hooper et al., 2007). It is expected that the phase stability of a given pixel (γ_x) should linearly decrease with increasing D_A pixel values such that $\gamma_{thresh} = kD_A$ where k is a constant. This process uses a threshold determined by the percentage of random (non-PS) pixels permissible within an area. Thresholding maximizes the number of real PS pixels selected while maintaining the fraction of false positives below the set threshold. In this case, the threshold is set to a maximum acceptable spatial density of pixels with random phase to be 20 pixels per km². Pixels are binned by D_A with at least 10^4 pixels in every bin and then binned by γ_x in increments of 0.01 to create a probability distribution. The PS pixels are then selected by estimating the proportion of pixels that are PS within each bin. A value for γ_{thresh} is calculated for each bin so that the fraction of false positive (non-PS) pixels selected is acceptable. Pixels with γ_x values greater than the γ_{thresh} are then selected for processing. Pixels are also rejected in this step if they are dominated by adjacent PS pixel scatterers or are only found with some interferograms. For the 2015 dataset, 196,822 targets were selected and 124,182 PS targets were selected for 2016.

4.1.2.4 PS Weeding

Pixels selected in the previous step are weeded, removing pixels that are too noisy, dominated by neighboring pixels. A smoothing window for estimating phase noise distribution for each pair of neighbouring pixels is applied using a Gaussian-weighted piecewise linear fit. The smoothing window is set to 730 days which covers the entire period of the dataset and the noise is assumed to be equivalent to the original phase minus the smoothed phase. Selected pixels may demonstrate a period of high phase stability that does not represent the phase stability throughout the entire time period. This is often the

result of areas undergoing change between acquisitions, such as a field being plowed. These pixels are weeded out by estimating the variance of γ_x for each pixel using a bootstrap percentile method with 1000 iterations and dropping pixels with a standard deviation over a defined threshold. A threshold of 1 standard deviation is used for discriminating pixels in this step. Pixels are also dropped by determining the minimum pixel-pair noise for each interferogram then testing the noise of a pixel to this threshold. If the noise value of the pixel is greater the interferogram-specific threshold, the pixel is dropped.

A bright scatterer can dominate neighboring pixels that do not correspond to the physical location of the scatterer. Errors in look angle and squint angle resulting from co-registration errors can result in pixels being offset from their physical location and not be selected as PS. In this case, neighboring pixels often exhibit strong responses corresponding to the same physical scatterer. Assuming adjacent pixels selected as PS are exhibiting stable phase from the same dominant scatterer, neighbours need to be weeded so only the pixel corresponding to the true location of the scatterer is selected. Typically, the pixel with the highest SNR within a group of neighboring pixels and has the highest γ_x value and is selected as the PS. Geocoding issues may also lead to duplicate PS candidate coordinates which are redundant and therefore removed during this step. For 2015, 148,228 pixels were selected as PS and 87,567 pixels were selected for 2016.

4.1.2.5 Phase Corrections

Accurate phase unwrapping is only possible when the absolute phase differences between neighbouring PS pixels is less than π. Generally, this is true for spatially correlated signals if the spatial density of sampled PS pixel is sufficiently dense. Contributions from spatially uncorrelated signal can cause the absolute phase differences between neighbouring PS pixels to be greater than π even when the sampling density is high. Majority of the spatially uncorrelated signal is the result of look angle error or DEM errors, which are estimated in previous steps. The contribution of the master to the spatially uncorrelated part of the signal can also be estimated. These two estimated terms are removed from the wrapped phase of the selected pixels before phase unwrapping. Patches created during the pre-processing are merged after phase corrections are applied. Pixel resampling is skipped during this step, resulting in no change to the number of PS pixels selected.

4.1.2.6 Phase Unwrapping

Before unwrapping the phase, noise within the data is reduced by spatially filtering the data using a Goldstein adaptive phase filter, built into the StaMPS software. For each interferogram, complex phase is sampled into a grid with spacing of 32m. This grid spacing is such that little variation of phase is expected within each grid cell. Phase is aggregated for all PS pixels within each grid cell and then transformed using the fast Fourier transform before being filtering using the Goldstein filter. This results

in the dominant frequency being preserved while omitting much of the noise. Phase noise is also estimated and smoothed using an adaptive Gaussian window with a 730-day window, once again covering the entire period of the study. This is particularly useful for determining the probability that a phase jump occurring between a pair in each interferogram. The grid cells are transformed back to points and used as input for the phase unwrapping.

Phase unwrapping for a single interferogram or a pair of interferograms can be completed by spatially unwrapping the phase differences between neighbouring interferogram pairs. However, as this data contains three dimensions of phase data, the third dimension being time, a three-dimensional unwrapping algorithm is used for more reliable results (Hooper et al., 2007). The results of the unwrapping algorithm can be given by:

$$\hat{\phi}_{x,i} = \phi_{D,x,i} + \phi_{A,x,i} + \Delta\phi_{S,x,i} + \Delta\phi^C_{\theta,x,i} + \Delta\phi_{N,x,i} + 2K_{x,i}\pi \qquad \text{(Eq. 26)}$$

Where $\hat{\phi}_{x,i}$ is the unwrapped phase value and $K_{x,i}$ is the unknown integer phase ambiguity that is associated with each interferogram.

4.1.2.7 Spatially Correlated Look Angle Errors and Atmospheric Noise Filtering

After phase unwrapping, spatially correlated look angle error, $\Delta\phi^C_{\theta,x,i}$, remains as part of the unwrapped phase, and masks the values for movement in the line of sight of the satellite, $\phi_{D,x,i}$. Spatially uncorrelated errors can be treated as random noise, but spatially correlated errors create a bias in the results and must be corrected for. This is most prominent in interferograms with large perpendicular baselines as the larger difference in position correlates with a larger difference in look angle error. This error creates a linear distortion to the phase values across the interferogram that can be detrended. To do this, spatially correlated terms are separated into temporally correlated and temporally uncorrelated contributions using spatial and temporal filters. Temporally correlated contributions are influenced by the master's contribution to the $\phi_{A,x,i}$ and $\Delta\phi_{S,x,i}$ terms and are present in all interferograms. Temporally uncorrelated contributions come from the slaves' contributions to $\phi_{A,x,i}$ and $\Delta\phi_{S,x,i}$ and form look angle errors. Contributions from the master are estimated using a low-pass filter in time while slave contributions are estimated using a high-pass filter in time applied to the phase difference between neighbouring PS pixels. Low-pass spatial filters are then applied to each interferogram using a two-dimensional Gaussian function. Both the temporally correlated and temporally uncorrelated contributions are removed from the unwrapped phase, isolating $\phi_{D,x,i}$.

4.1.2.8 Deformation Rate

The isolated $\phi_{D,x,i}$ term from corrected unwrapped phase is then transformed into the mean displacement velocity for each selected pixel using the process mentioned in Section 2.7. The unwrapped phase is first converted to displacements for each of the PS candidates using the following equation:

$$\phi_{D,x,i} = \frac{4\pi d}{\lambda} \qquad \text{(Eq. 27)}$$

Where $\phi_{D,x,i}$ is the phase contribution from ground deformation, d is the displacement and λ is the wavelength used, in this case 5.6 cm. The displacement between acquisitions is then converted to an average deformation rate using a linear least square method that minimizes the sum of squared error. The deformation rate is calculated for each PS candidate in mm per year.

4.2 Small Baseline Subset

Small baseline subset method aims to limit the spatial decorrelation of a dataset considering both the spatial and temporal information of the dataset (Berardino et al., 2002). SBAS can calculate the average velocity of a pixel by measuring the average displacements estimated from each interferogram within a time series. Unlike PS methods, SBAS utilizes a multi-master approach to generate as many interferometric pairs as possible given temporal and perpendicular baseline thresholds. This process still requires a super master which dictates the spatial extent and processing parameters for the entire dataset. In this case, the super masters chosen are the same images chosen as the masters for the PS processing. This is to improve correlation between the two data sets and ensure the two processes are measuring deformation rates relative to the same reference surface. The SBAS method is completed using GMTSAR, a linux-based program written in C. This process is completed in 10 steps: 1. ROI and DEM definition 2. Precise orbit downloads and organization 3. Baseline generations and Super master selection 4. Pair Selections 5. Interferogram Generation. 6. Swath Merging. 7. Coherence Masking 8. Phase Unwrapping 9. SBAS Time-Series/Deformation Rates 10. Geographical transformations.

4.2.1 Pre-processing

A region of interested is defined using two coordinate pairs, (50.7, 6.6) and (51.1, 6.1), to limit the extent of processing and decrease processing times. Although similar to the swath and burst selection completed in the PS preprocessing, this subset approach is able to span between multiple swaths and bursts at the cost of processing times. An external DEM covering this extent is generated using SRTM3 with a 90-meter resolution. This DEM will be used throughout processing as a reference DEM. Due to the limitations of the program, this boundary cannot span more than 4 longitude by 4 latitude degrees. Precise orbital files are acquired and applied to the SAR images to ensure the images may be aligned properly with each other. During this time, the VV polarized data is selected for processing.

4.2.2 Super Master and Pair Selections

Temporal and perpendicular baselines are calculated for the entire datasets. Using these baselines, a super master for each dataset is chosen. For consistency, the images acquired on June 2nd and August 1st are chosen to match the master images selected for the PSI processing for 2015 and 2016, respectively. This ensures the measurements made by both techniques spatially aligned, minimizing co-registration errors when comparing the two techniques. A comparison between spatial and temporal baselines of the radar images is performed to create interferometric pairs between radar acquisitions with baselines small enough to have high coherence. To create these pairs, thresholds of 50 days and 100-meters are applied to the temporal and perpendicular baselines. This results in 72 pairs for 2015 and 117 pairs for 2016 that will be used to create interferograms. The resulting connection graphs are shown in figure 12. Images that do not cover the entire processing extent are omitted during this step. Baselines are then recalculated using the new super master as a reference image. As the images are in Slant Range format, the slave images are co-registered and geometrically corrected to spatially align with the super masters selected. During this process, the images are resampled with the master image, given the same geometry and formed into an interferogram stack.
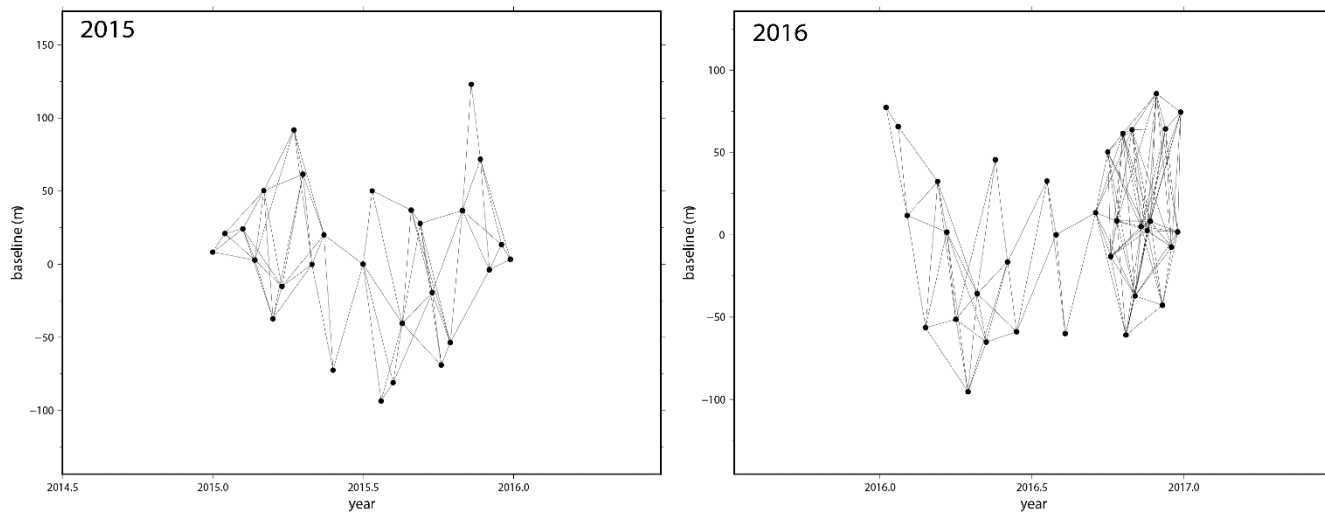
Figure 12. Visualization of the interferometric pairs formed by SBAS for 2015 (left) and 2016 (right) using the master dates of July 2nd, 2015 and August 1st, 2016.

4.2.3 Interferogram Generation

A single interferogram is first generated using the super master image and any slave for each swath used. The interferogram generation is completed using the same process outlined in Section 2.6. In this case, interferogram generation for swath one is skipped as it lies outside the defined region of interest. Alongside the single interferogram, topographic phase is calculated using the SRTM3 DEM and stored to be subtracted from the interferometric phase of all the pairs. This is once again to isolate the contribution of $\delta\varphi_{defo}$ within the total interferometric phase. Following this, interferograms for each

pair defined in the previous step is generated using the SRTM3 data as the reference DEM. The original interferogram is also reprocessed to consider the topographic phase contributions. The stack of interferograms is then flattened using the contributions of the reference DEM and topographic phase calculated by the original interferogram generated. The resulting interferograms are then merged to combine the two swaths, which are processed independently until this point. All merged interferograms are processed to contain the same coordinates and final grid size as the single reference interferogram created using the super master in the first step of interferogram generation. For each interferometric pair, merged coherence, mask and phase files are generated.

4.2.4 Create Coherence Mask

Phase unwrapping is one of the most time-consuming and computationally intensive steps of InSAR processing. Due to the nature of SBAS, this step is intensified by the total number of interferograms that are unwrapped per analysis. To limit the processing the SAR images were subset during the preprocessing to eliminate unnecessary areas or pixels. To further reduce the intensity of processing and to increase confidence of results, a coherence mask is applied to the stack of interferograms generated in the previous step. Lower coherence values can lead to lower accuracy in displacement estimates and significantly increase processing times. A coherence layer representing the entire dataset is created by stacking the coherence of each interferogram and performing a simple averaging on coherence values for each pixel with no scaling applied. The stacked coherence layers for 2015 and 2016 can be seen in Appendix D. A binary mask is created by applying a threshold of 0.075 to the stacked average coherence layer. Pixels with an average coherence less than 0.075 will be omitted from the processing. This value is selected such that only a small portion of pixels is excluded from the study. These pixels mostly include water bodies, such as rivers, and heavily forested areas. The coherence masks can be seen in Appendix E.

4.2.5 Phase Unwrapping

Phase unwrapping is completed for each interferogram within the stack using the Snaphu algorithm (Chen and Zebker, 2000). The general process for phase unwrapping in this step is largely identical to the process shown in Section 4.1.8. To reduce phase noise and improve processing times, a Goldstein adaptive phase filter is applied to the stack and the phase gradients in the range and azimuth directions are calculated. The correlation threshold for the unwrapping is set to a very low value (0.001) to avoid omitting pixels that were already deemed acceptable by the coherence mask. As the surface displacement varies slowly across the scene, except for the mining operations, phase discontinuities are not expected. Thus, the discontinuity threshold of 0 is set to reduce the impacts of ambiguous phase. Resulting cost functions assume that the true unwrapped phases represents a generic surface with no

discontinuities (Chen and Zebker, 2000). Like in the PS processing, a Goldstein adaptive phase filter is applied to smoothen the data, reduce noise and decrease the likelihood of phase discontinuities. An example of the processing chain used to generate an unwrapped interferogram using two Sentinel-1 SAR images and SBAS is shown in figure 13.
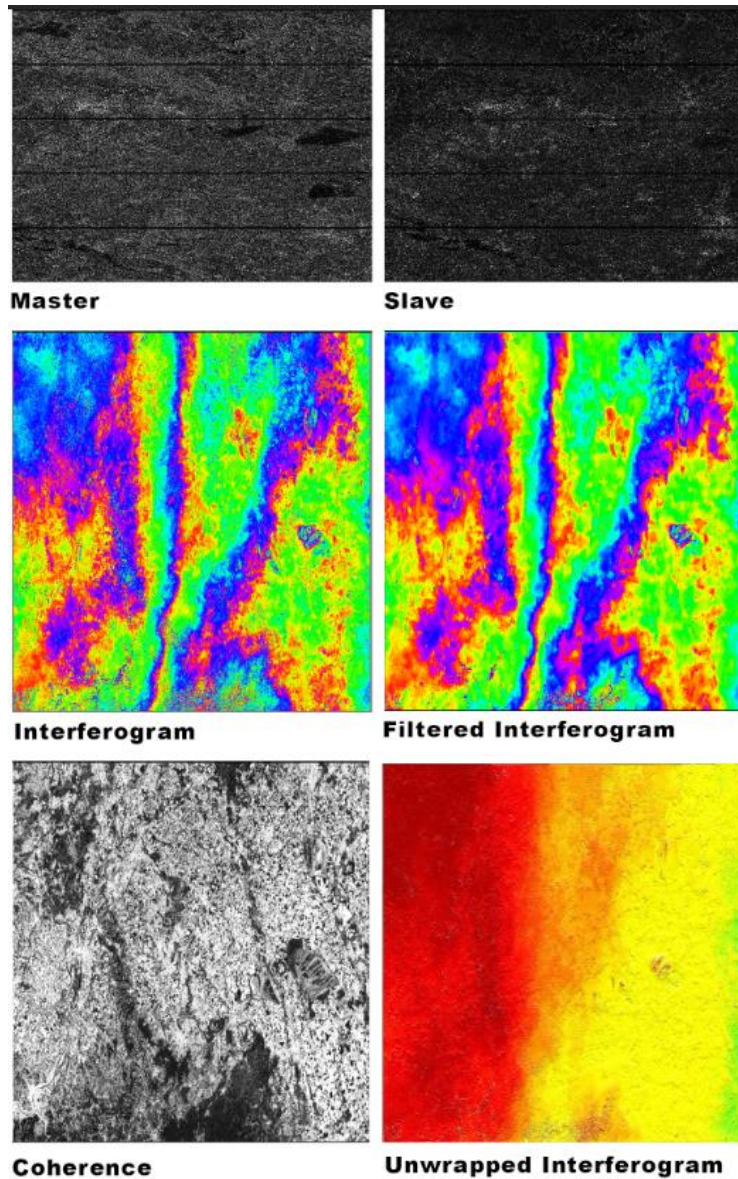
Figure 13. Visualization of the processing chain used to produce an unwrapped interferogram from two SLC SAR images.

4.2.6 SBAS Time-Series

By processing multiple acquisitions in series, interferometric components that corresponded to deformation, topographic error, atmospheric error and orbital errors can be separated from the interferometric phase. The unwrapped phase signal for a coherent pixel in an interferogram formed by

45

SAR images acquires at times tb and ta, after flat earth and topographic phase removal can be written as:

$$\delta\phi_{x,i} = \varphi_x(tb) - \varphi_x(ta) \qquad \text{(Eq. 28)}$$

$$\approx \delta\phi_{def,x,i} + \delta\phi_{\varepsilon,x,j} + \delta\phi_{a,x,i} + \delta\phi_{orb,x,i} + \delta\phi_{n,x,i}$$

$$= \frac{4\pi}{\lambda}[d_x(tb) - d_x(ta)] + \frac{4\pi B_{\perp x,i}\Delta z}{\lambda R \sin\theta} + \delta\phi_{a,x,i} + \delta\phi_{orb,x,i} + \delta\phi_{n,x,i}$$

Where $\delta\phi_{x,i}$ is the differential interferometric phase and $\varphi_x(tb)$ and $\varphi_x(ta)$ are the phases of the two images acquired at times tb and ta, respectively. Phase contributions from cumulative surface deformations $\delta\phi_{def,x,i}$, topographic phase error $\delta\phi_{\varepsilon,x,j}$, atmospheric delay $\delta\phi_{a,x,i}$, orbital error $\delta\phi_{orb,x,i}$ and decorrelation noise $\delta\phi_{n,x,i}$ such as thermal effects or co-registration errors. Deformation rate, v, can be calculated from phase contributions from surface deformation $\delta\phi_{def,x,i}$, assuming that $v_{j,j+1}$ indicates the linear deformation rate between the two images acquired at tb and ta (Liu et al., 2020). The deformation rate across the time series can then be expressed as:

$$\delta\phi_{def,x,i} = \frac{4\pi}{\lambda}\sum_{j=ta}^{tb-1} v_{j,j+1}(t_{j+1} - t_j) \qquad \text{(Eq. 29)}$$

4.2.7 Geocoding

Geocoding transforms the results from the SBAS processing, which is processed completed in radar coordinates (slant range), into images whose distances represent real distances on the ground (Chaabani & Deffontaines, 2020). In this work, the images are geocoded according to the WGS 84 map projection. The final images can show information that represents estimated surface deformation, measured in mm/year, in a latitude/longitude coordinate system.

4.2.8 Post Processing

The results from PSI and SBAS are subset to exclude the mining operations. Mining operations are non-coherent processes where expected change between acquisitions is greater than the maximum change that can be accurately measured using InSAR techniques, as discussed in Section 2.7. This creates generally poor coherence values which are too low to reliably unwrap phase in the area and causes phase ambiguity. Additionally, the physical shape of the mining pits causes phase shadow discontinuities resulting from the steep slopes, and inability to have a synoptic view of the pit due to a singular viewing geometry. For direct comparison to GNSS station data, the LoS measurements are converted to vertical measurements using the following equation:

$$v_{vertical} = V_{LoS}/\cos\theta \qquad \text{(Eq. 30)}$$

Where V_{LoS} is the estimated deformation rates from PSI and SBAS and θ is the incidence angle for that point.

4.3 Uncertainty Estimations

To estimate uncertainty of the PSI and SBAS results, internal and external testing is performed. Internal testing is completed through comparison of deformation rates estimated by PSI and SBAS by extracting values from each dataset and pairing them by geographical location. These pairs are then used to determine the correlation coefficient, the bias and root mean squared error between the two sets of results. The data pairs are also used to generate scatter plots and heat maps showing the distribution of the deformation rates relative to each other. An additional test is completed by selecting only the pixels that are within areas classified as urban. Urban area measurements are extracted as hard targets have relatively consistent scattering properties with minimal seasonal variation. This classification is determined by the aggregated CLC classes mentioned in Section 3.3. Boxplots are used to show the total variation and averages of the datasets.

External testing is completed by comparing the PSI and SBAS displacement estimates with the EUREF GNSS station data. GNSS data were processed using the Canadian Spatial Reference System Precise Point Positioning (CSRS-PPP) service provided by National Resources Canada (National Resources Canada, 2020). The service transforms RINEX data files, into positional data for a single station. Each file contains data for one day for a particular station, containing coordinates and elevation for that point. As the precision of this technique yields 3 cm of positional accuracy per file, the uncertainty of these measurements is too great to reliably compare to the long-term sub-centimeter results of the PSI and SBAS processing. To combat this, a least squares regression-based approached is used to calculate the estimated deformation rate measured by the GNSS station, rather than using a cumulative difference between each date. Annual deformation rates for each station for 2015 and 2016 are calculated by multiplying the slope of the linear regression by the total days within the time span. By using the slope of the line of best fit for the deformation estimations, the variability of each measurement is averaged, reducing the impact on the final measurements. To further reduce the impacts of the positional uncertainties in the GNSS data, the time span of collected data is increased to six years (2014 – 2020) for the Euskirchen and Eijsden stations, and five years for the Titz station (as 2014 data was unavailable). To help determine whether the measured change for a station, is real or the result of noise, one-sided Mann-Kendall trending testing is performed. This is a non-parametric test used to determine whether a time series has a monotonic upward or downward trend.

Chapter 5

Results

5.1 PSI Deformation Measurements

Annual deformation rates along the LOS direction are measured for 2015 and 2016 using StaMPS, applied to Sentinel-1 SLC ascending imagery. Figure 14 and Figure 15 show the surface deformation rates in the LOS direction in mm/year, for 2015 and 2016, respectively. Negative values indicate that the surface deformation is moving away from the LOS direction, representing surface subsidence. Similarly, positive values indicate a surface motion towards the LOS direction, representing surface uplift. Individual contrast figures for the 2015 and 2016 PSI results can be found in Appendix F and Appendix G. As the mining pits themselves were masked out from the processing results, there are no deformation measurements available in these areas. Different regions of interest within the study area are identified in Figure 14 and Figure 15.

Although the 2015 data set has significantly more detected persistent scatterers (148228) than 2016 (87567), both data sets show similar deformation patterns overall. As expected, most of the detected persistent scatterers are in urban areas, with a large number being detected over road networks and some detected in agricultural fields. For both years, the landscape shows a general trend of small surface uplift, with subsidence occurring closer to the mining operations. Areas of heavy vegetation coverage tend to show moderate rates of surface uplift. Conversely, built-up and urban regions experienced little to no surface movement, with built-up areas nearest to the mines experiencing more surface subsidence.

The most pronounced subsidence is measured east of the Hambach mine (R1 in Figure 14) with deformation rates up to -61 mm/year and -67 mm/year for 2015 and 2016, respectively. The 2015 results so an average displacement of -23 mm/year and a standard deviation of 13 mm/year, while the 2016 results show an average displacement of -25 mm/year and a standard deviation of 12 mm/year. Within this region, land subsidence rates increase towards the south eastern portion of the mine and decrease in magnitude with increased distance from the eastern part of mine.

A similar but less pronounced pattern is observed in the region northeast of the Inden mine (R2). Here, subsidence up to -27 mm/year for 2015 and -25 mm/year for 2016 are observed close to the mining operation. Average deformation rates of -8 mm/year and -9 mm/year are measured in this region for 2015 and 2016, respectively, with standard deviations of 4 mm/year for both. Compared to the region east of the Hambach mine (R1), there is a less prominent radial pattern of decreasing subsidence rates. The extent of subsidence is more localized around the Inden mine, with most subsidence occurring only in the eastern portion (R2) whereas subsidence around the Hambach mines stretches from north of the mine, around the east and to the south. To the west of Inden mine there is a small region of subsidence detected

in the 2016 data set only, measured over agricultural fields very close to the mining operation. South of this is a small mining operation (R3) with localized subsidence, detected by both data sets, that does not exhibit the same radial deformation pattern as the Inden and Hambach mines.

Subsidence rates around the Garzweiler mines are also most pronounced close to the mines, primarily between Garzweiler I and Garzweiler II and to the west of Garzweiler II. Between the mines (R4) there are only a few persistent scatterers detected (180 for 2015 and 32 for 2016) but show deformation rates up to -44 mm/year for 2015 And -27 mm/year for 2016, with average deformations of -12 mm/year and -6 mm/year. The area west of the Garzweiler II mine (R5) shows a discrepancy between the two data sets, as the 2015 data set shows significant subsidence, up to -34 mm/year, while 2016 shows primarily uplift. The 2015 results here show an average deformation rate of -14 mm/year and a maximum uplift of 4 mm/year with a standard deviation of 6 mm/year. Comparatively, the 2016 results show that on average, the area is experiencing 1 mm/year of uplift, with a maximum uplift rate of 15 mm/year, a maximum subsidence rate of only -8 mm/year and a standard deviation of 3 mm/year. Even with this discrepancy, both data sets show the same radial pattern discussed with higher subsidence rates or lower uplift rates closer to the mining pit, gradually showing increased surface uplift as you progress away from the mine.

In Mönchengladbach (R6), the city north of the Garzweiler mines, there is a high density of detected persistent scatterers, showing pattern of surface uplift for both years. The 2015 data sets show a gradient of deformation, progressing from surface subsidence to surface uplift as you move away from the mines and from the region of subsidence to the west of the mine (R5). The average displacement observed here for 2015 is 4 mm/year with rates ranging from -14 mm/year to 19 mm/year and a standard deviation of 3.9 mm/year. The 2016 data shows similar values with an average of 4.9 mm/year, deformation rates ranging from -15 mm/year to 18 mm/year and a standard deviation of 2 mm/year. Although the two year share similar statistics, the 2016 data set does not show the same pattern of surface subsidence in the southern part of the region.

Similarly to the small mining operation west of Inden (R3), there is a small mining operation south east of the Garzweiler mines (R7) that shows prominent subsidence. The subsidence here is detected more within the 2015 data set, with only a few persistent scatterers identified here in the 2016 data set. For 2015, there are 501 persistent scatterers identified, with an average deformation of -5 mm/year, a max deformation rate of -47 mm/year and a standard deviation of 12 mm/year. Comparatively, the 2016 shows only 97 persistent scatterers with a maximum deformation rate of -29 mm/year, an average of -6 mm/year and a standard deviation of 8 mm/year. The deformation patterns in this area are similar to the radial patterns observed around the other mining activities, with subsidence

being localized to one side of the mine, decreasing in magnitude as you move away from the south portion of the mine.
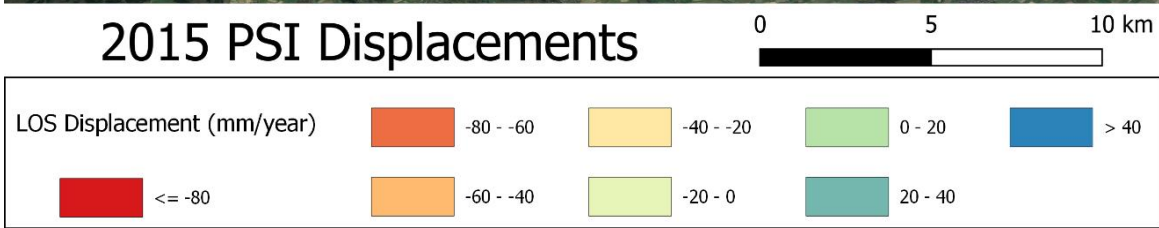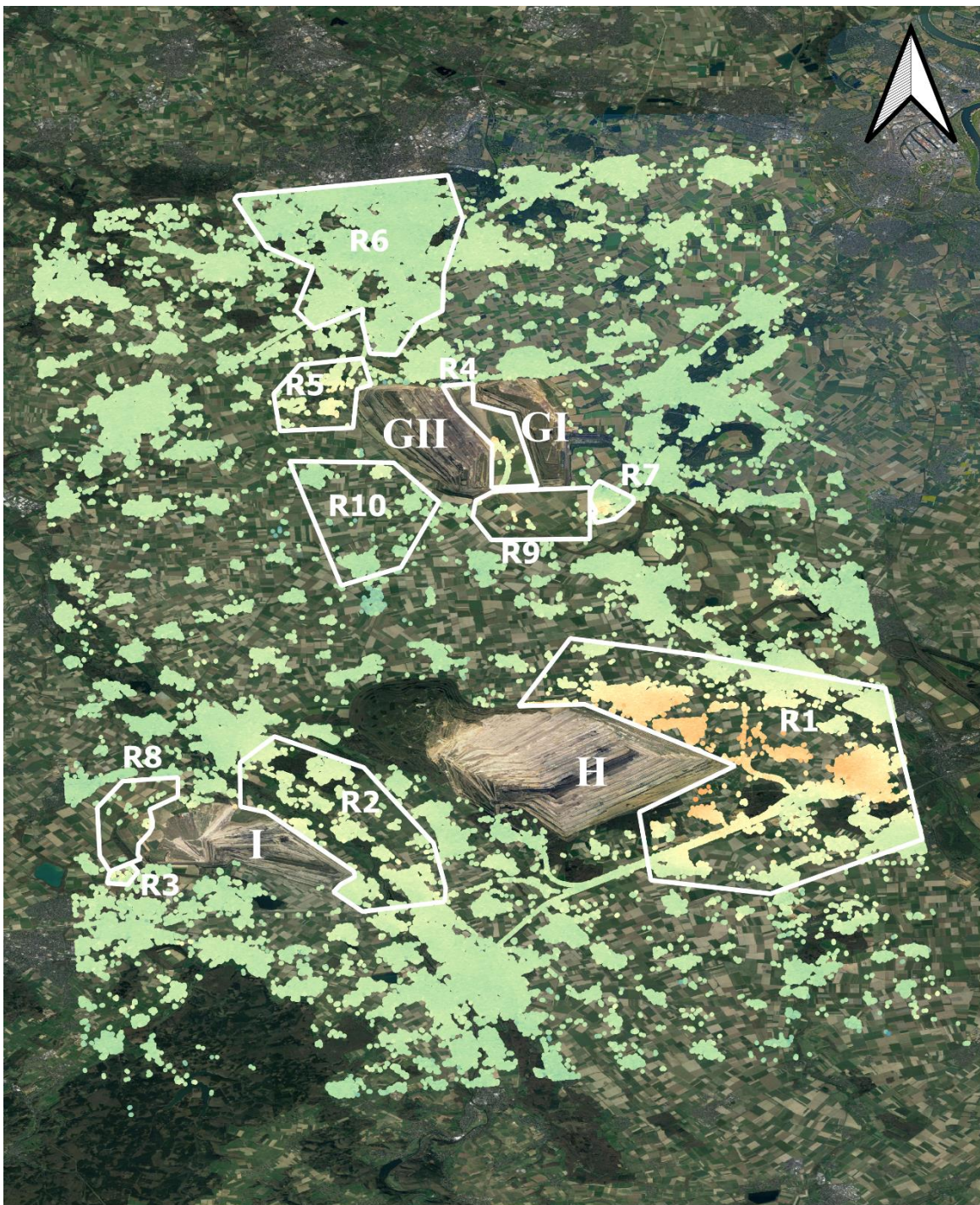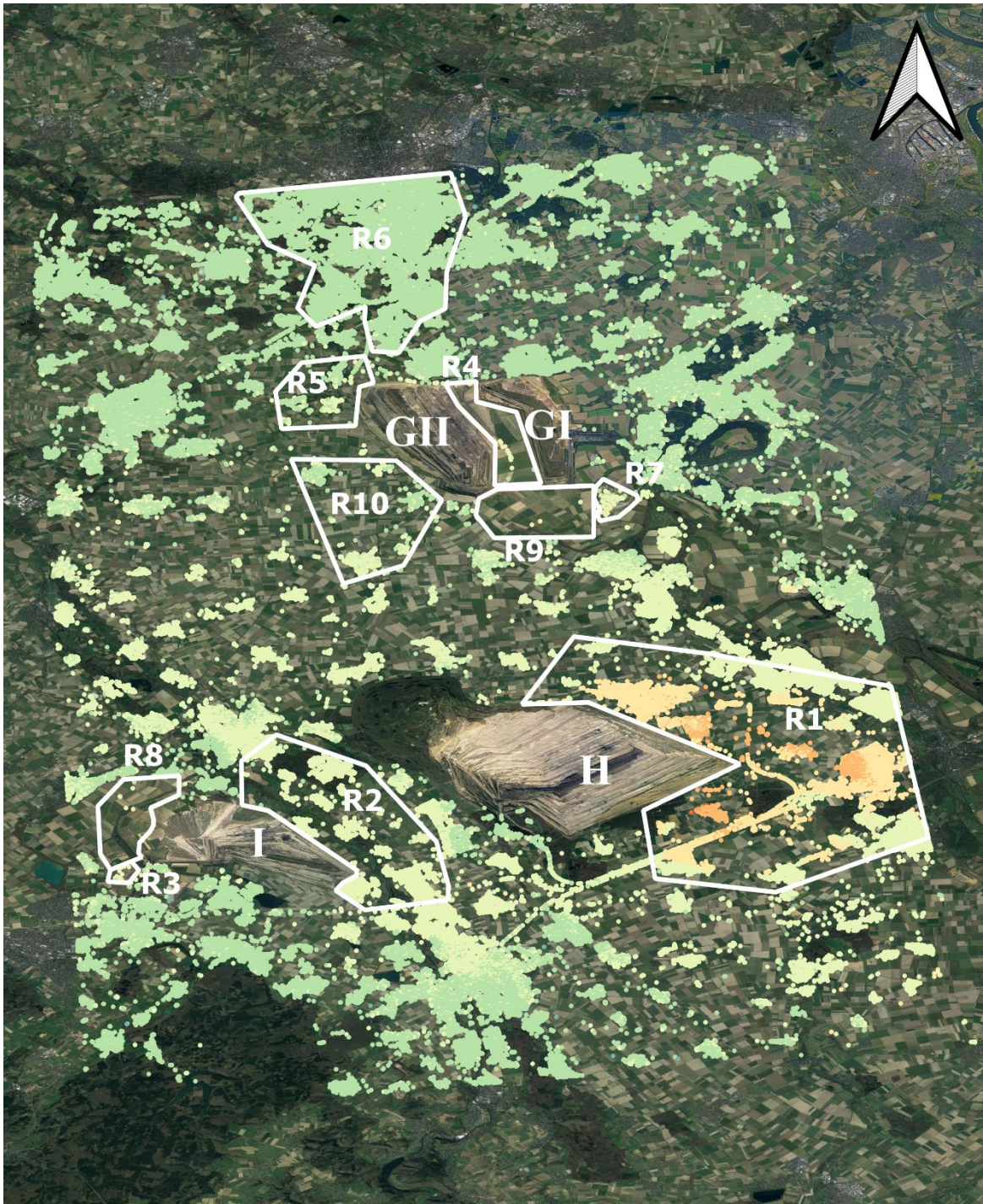
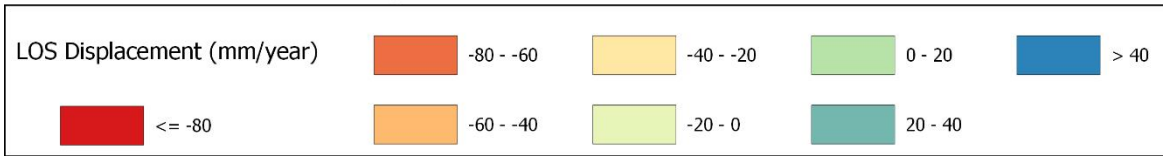*Figure 14. Deformation rates in the LoS measured by PSI for 2015 with regions of interests overlaid.*

Figure 15. Deformation rates in the LoS measured by PSI for 2016 with regions of interests overlaid.
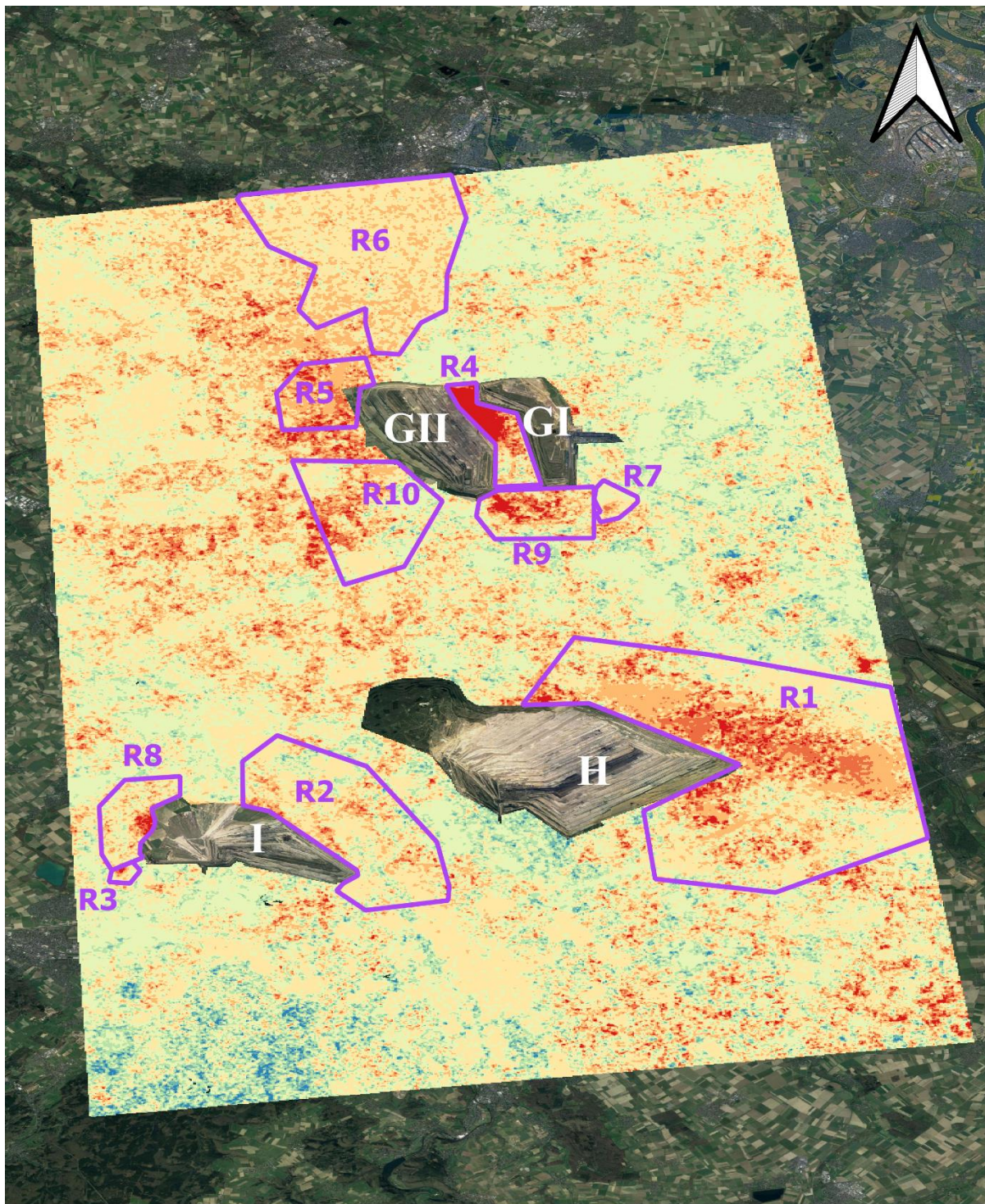
5.2 SBAS Deformation Measurements

Annual deformation rates along the LOS direction were also measured from 2015 and 2016 using Sentinel-1 imagery and SBAS applied through GMTSAR. Figure 16 and Figure 17 shows the deformation rates in the LOS direction in mm/year for 2015 and 2016, respectively. Similarly with the PSI results, negative values indicate that the surface deformation is moving away from the LOS direction, representing surface subsidence while positive values indicate movement towards the LOS direction, representing surface uplift. Once again, the mining pits are masked out during the processing and no deformation measurements are available in these areas. The regions of interest defined in Section 5.1 are shown with the SBAS results in Figure 16 and Figure 17.

A similar pattern of deformation seen in the PSI results is observed in the 2015 and 2016 SBAS results, with mostly small rates of land subsidence and hotspots of surface uplift or large subsidence deformation. Additionally, heavily vegetated areas showed predominant surface uplift while urban and built-up areas show little to no deformation. However, urban and built-up areas near the mining activities show significant surface subsidence. The 2015 displacement measurements showed an average deformation rate of -25 mm/year, a median of -23 mm/year and a standard deviation of 22 mm/year. Comparatively, the 2016 displacement measurements had lower rates of change with an average deformation rate of -19 mm/year, a median of -14 mm/year and a standard deviation of 24 mm/year. The maximum surface subsidence measured for 2015 and 2016 was -250 mm/year and -260 mm/year, respectively. For both years, the maximum surface subsidence was mainly distributed between Garzweiler I and Garzweiler II mines (R4 in Figure 16). The maximum surface uplifted measured for 2015 and 2016 were 73 mm/year 71 mm/year, respectively.

Similarly to the PSI estimates, prominent large-scale subsidence is observed east of the Hambach mines (R1) with subsidence becoming less extreme as you move away from the eastern portion of the mine. In this region, the largest subsidence rates, up to -143 mm/year for 2015 and -181 mm/year for 2016 are measured mostly over agricultural fields. Although there is a large difference between maximum deformation rates, the differences in average deformation rates and standard deviations are less significant. For 2015, an average deformation rate of -39 mm/year with a standard deviation of 20 mm/year is observed while 2016 shows an average rate of -42 mm/year and a standard deviation of 22 mm/year. Urban areas in the same region show similar average deformation rates of -40 mm/year and –33 mm/year for 2015 and 2016. However, they show lower maximum rates of deformation and lower standard deviations. A maximum subsidence rate of -106 mm/year is observed for 2015 with 12 mm/year of standard deviation while a maximum rate of -76 mm/year and a standard deviation of 17 mm/year is seen in the 2016 results.
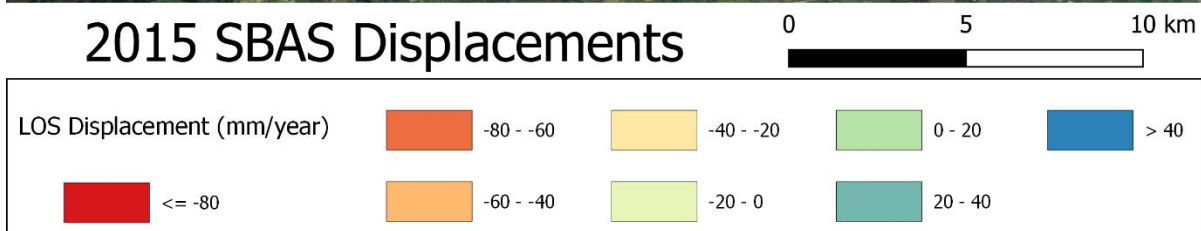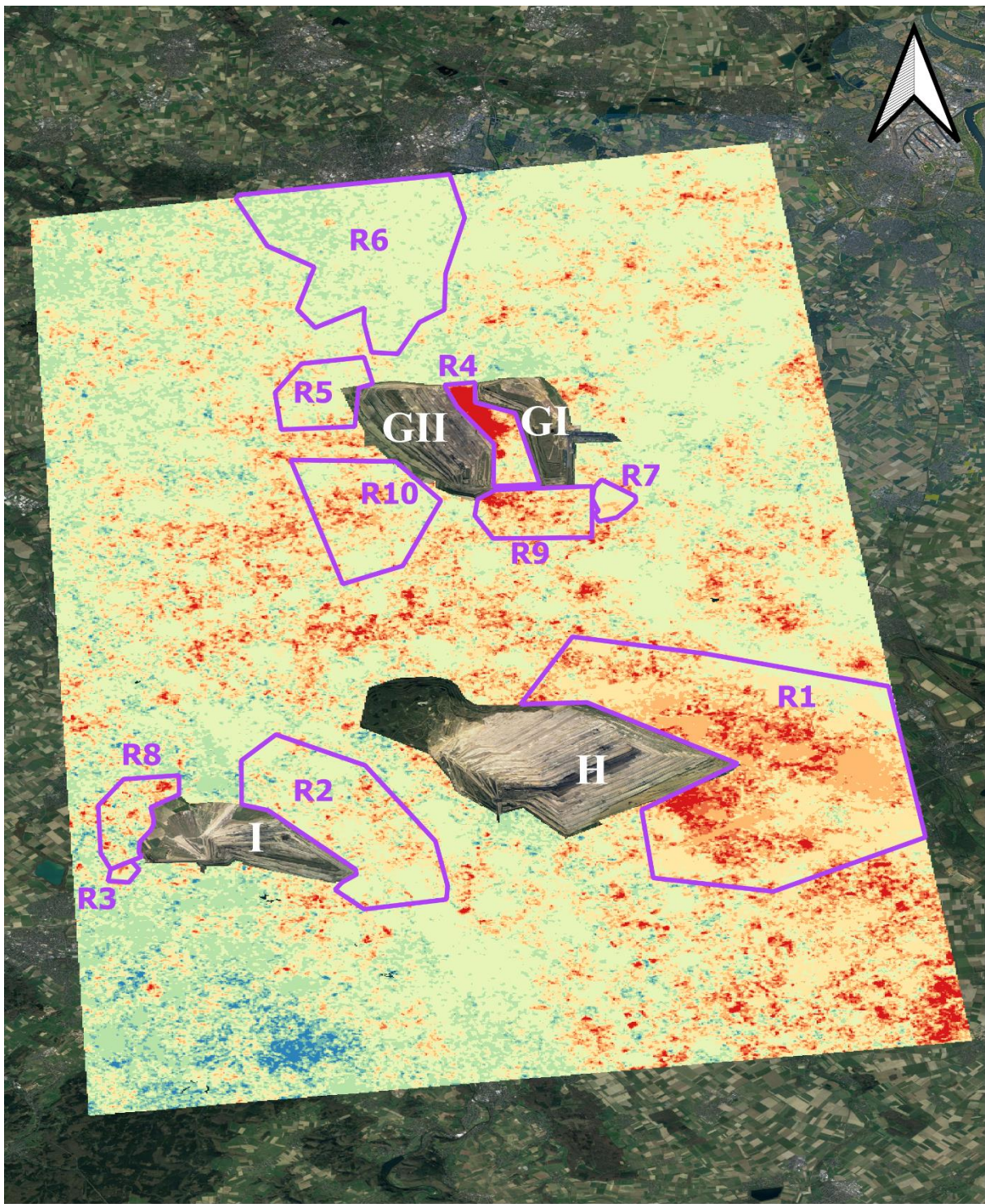
Figure 16. Deformation rates in the LoS measured by SBAS for 2015 with regions of interests overlaid.

Figure 17. Deformation rates in the LoS measured by SBAS for 2016 with regions of interests overlaid.

The region east of the Inden mine (R2) shows more significant land subsidence in 2015 than 2016. Both the 2015 and 2016 data sets show high maximum deformation rates of -107 mm/year and -108 mm/year, respectively, and similar standard deviations of 18 mm/year and 17 mm/year. However, a larger average deformation rate of -27 mm/year is observed in 2015, compared to the average rate of -17 mm/year measured in 2016. These deformation rates show a significantly less distinct pattern of land subsidence compared to the pattern seen in the region east of the Hambach mine (R1). A more comparable pattern of subsidence is observed west of the Inden mine (R8) with maximum subsidence rates of -130 mm/year and -141 mm/year for 2015 and 2016. Although a higher maximum rate is seen here in 2016, a higher average rate is observed in 2015. The average subsidence rate for 2015 is -34 mm/year while the average rate for 2016 is -23 mm/year. Additionally, the average deviation of measurements is lower for 2015, 22 mm/year, than for 2016, 26 mm/year. South of this region, in the area around the smaller mine (R3), high subsidence rates are observed for both years with a higher average rate being measured in 2015. The maximum subsidence rates for the two years are -101 mm/year and -96 mm/year and the average deformation rates are -35 mm/year and -21 mm/year, for 2015 and 2016 respectively. Comparing the 2015 and 2016 subsidence rates around the Inden mine, 2015 shows more significant subsidence immediately beside the mine, both in the eastern (R2) and western (R8) portions. This pattern is not prominent in the 2016 estimates around the Inden mine.

The region between the Garzweiler I and Garzweiler II mines (R4) exhibits the highest amount of subsidence for both datasets. The 2015 data shows an average subsidence of -81 mm/year with a maximum deformation rate of -261 mm/years in this region. The 2016 dataset shows a smaller average displacement rate of -72 mm/year but a much larger maximum rate of -277 mm/year for the same area. This region consists mostly of agricultural fields with a highway running through. South of this area, and south of the Garzweiler I and Garzweiler II mines (R9), is another common hotspot for subsidence for both datasets. This region is almost entirely agricultural fields with a sparse road network. At this location, the 2015 results show an average land subsidence rate of -44 mm/year with a maximum rate of -187 mm/year. Showing less deformation, the 2016 results show an average deformation rate of -39 mm/year and a maximum rate of -122 mm/year. The small mining site east of this region (R7) shows a similar pattern as the small mining site west of Inden (R3) with higher deformation rates observed in 2015. For 2015, this region shows an average surface deformation rate of -28 mm/year with a maximum rate of -78 mm/year and a standard deviation of 14 mm/year. Meanwhile, the 2016 measurements show lower deformation rates with an average of -21 mm/year and a maximum rate of -66 mm/year but a higher standard deviation of 19 mm/year. Additionally, the land deformation around this small mine follows the pattern of land subsidence occurring more prominently on one side of the mining operation

as seen around the other mines in the area. In this case, the area south of the small mine shows prominent land subsidence for both years.

The largest discrepancy between the 2015 and 2016 SBAS datasets is observed west of the Garzweiler mines (R5) and over the city north of the Garzweiler mines (R6). The prominent subsidence west of the mine shows the same pattern discussed above. However, this pattern is significantly more dominate in the 2015 results, showing an average deformation rate of -55 mm/year and a maximum rate of -128 mm/year. Comparatively, the 2016 measurements show only -17 mm/year as the average deformation rate and a maximum rate of -87 mm/year. A similar but more pronounced trend between the two years is observed around the city to the north (R6). Here, the 2015 results show much higher deformation rates, averaging -35 mm/year with a maximum rate of -91 mm/year, compared to the -3 mm/year average and -70 mm/year maximum measured in 2016.

5.3 Internal Uncertainty

The SBAS process also produces a map for each year showing the root mean squared (RMS) value for each pixel. Figure 18 shows the RMS maps created during the SBAS process for 2015 and 2016, respectively. Since precise surveying data of land deformation in the area is not available, the RMS can be used to represent the uncertainty of the velocity measurements made by SBAS. Areas with larger RMS values can indicate nonlinear deformation or large errors caused by unwanted phase contributions or phase unwrapping errors. Both the 2015 and 2016 results show an average RMS of 6 mm across the entire scene. However, the 2015 data set shows a higher maximum RMS of 24 mm and standard deviation of 2 mm/year, compared to the 15 mm average and 1 mm/year standard deviation seen in the 2016 measurements. For both years, the highest RMS values observed are over agricultural areas while the lowest values are seen over heavily forested areas or small water bodies. This relationship is more prominent in the 2015 results, particularly when viewing the RMS values over agricultural lands. Areas experiencing little deformation showed homogenous RMS values that were low in magnitude. Urban areas show moderate RMS values that tend to be higher than their surrounding regions. This trend is more prominent in the 2016 results as the RMS over agricultural lands is significantly smaller for this year, causing the proportional difference between urban areas and the surrounding land less to be more pronounced. In both years, the RMS over urban areas has less spatial variation. This is especially true when observing RMS over cities for 2016.
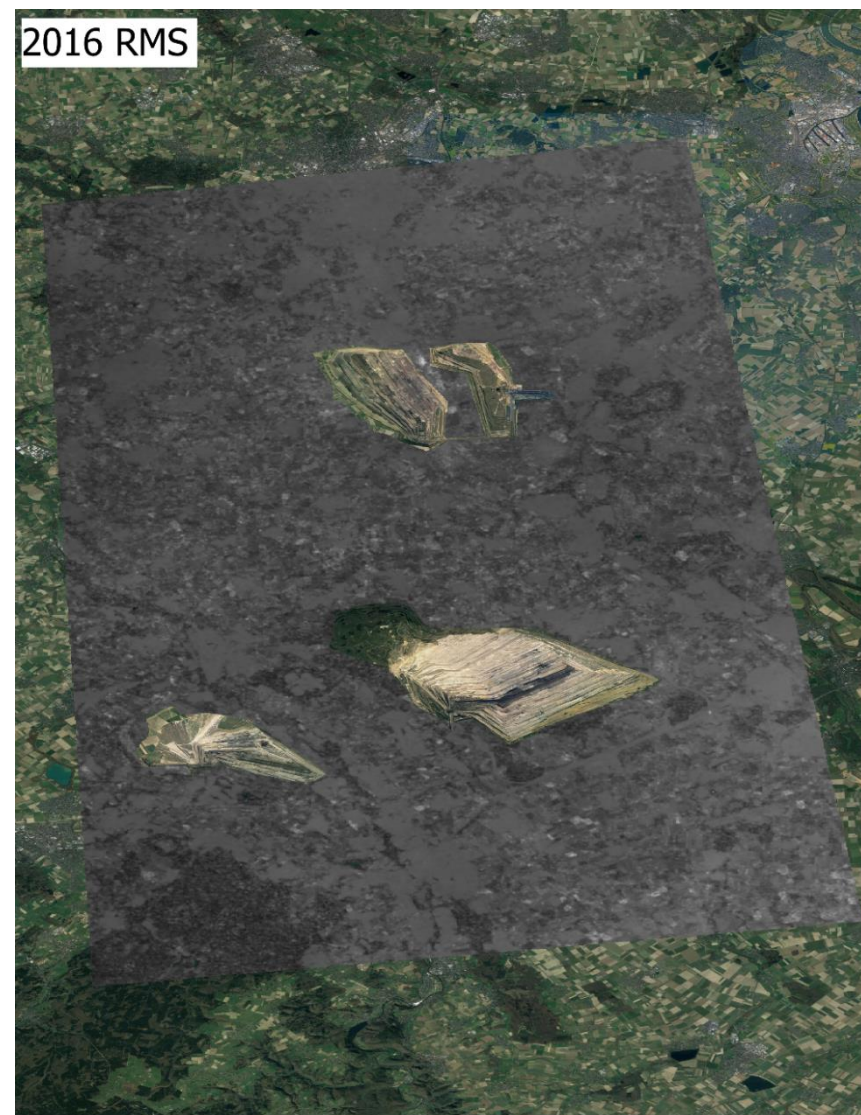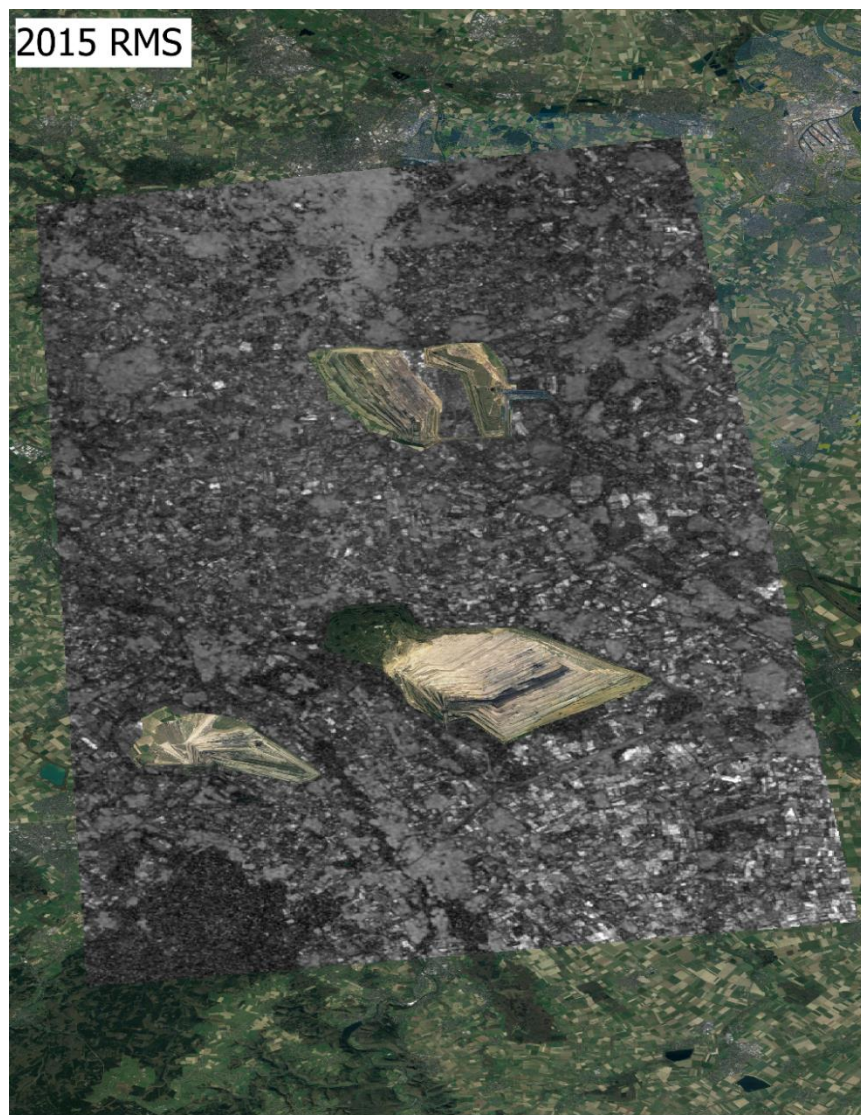
Figure 18. Maps of the Root Mean Squared of deformation estimates generated by GMTSAR during SBAS processing for 2015 (left) and 2016 (right).

For both years, deformation rates corresponding to the same geographical location in the PSI and SBAS results were paired together to measure agreement between the two methods. Scatterplots showing the point pairs for 2015 and 2016 are shown in figure 19, respectively. Overall, the 2015 datasets show less agreement than the 2016 datasets. The 2015 PSI and SBAS values have a 0.597 correlation coefficient, showing reasonable agreement between the two. Comparatively, the 2016 results have a correlation coefficient of 0.89, showing a more significant correlation between the measurements made by the two methodologies. This pattern is also reflected in the bias and root mean squared error (RMSE) of both years. For 2015, there is a -24 mm/year bias, indicating that the SBAS measurements tend overestimate land subsidence when compared to the PSI results. More importantly, the SBAS measurements indicate certain areas are experiencing surface subsidence while the PSI measurements show those areas to be experiencing uplift. This is also true for the 2016 results, which have a bias -6.9 mm/year. Although the bias seen in 2016 is less significant compared to 2015, the same overall trend is observed between both years. Furthermore, the 2015 comparisons show a higher RMSE of 26 mm/year, compared to the 9 mm/year seen in the 2016 results. This indicates a larger variability is observed between the SBAS and PSI measurements for 2015 than for 2016.
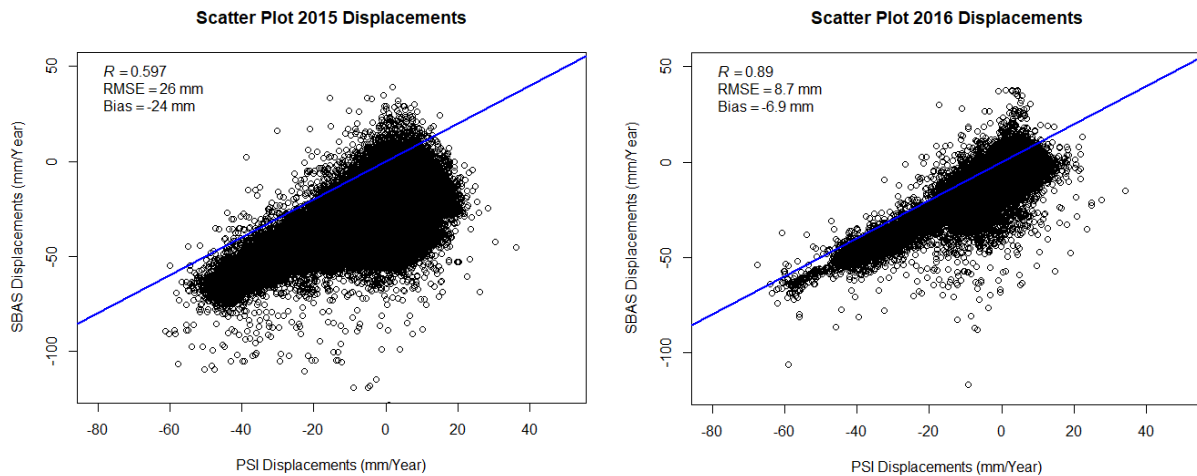
Figure 19. Scatterplots of PSI measurements (x-axis) and SBAS measurements (y-axis) for 2015 (left) and 2016 (right). The line of equality is denoted as the blue line.

In general, the SBAS measurements show much higher variability than the PSI measurements. This is reflected not only in the upper and lower bounds of the measured displacements but also in the standard deviation of values. The standard deviations of measured displacements are similar between the two years, varying mostly by the method used. Boxplots showing the variability of each data for 2015 and 2016 is shown in Figure 20. The PSI measurements showed standard deviations of 10.65 mm/year

for 2015, and 10.36 mm/year for 2016. Comparatively, the SBAS measurements showed significantly higher standard deviations of 22.50 mm/year for 2015 and 23.77 mm/year for 2016. For all four data sets, there is a larger distribution of measurements showing increased levels of surface subsidence, relative to the median. This is most prominent when observing the variability of the SBAS measurements.
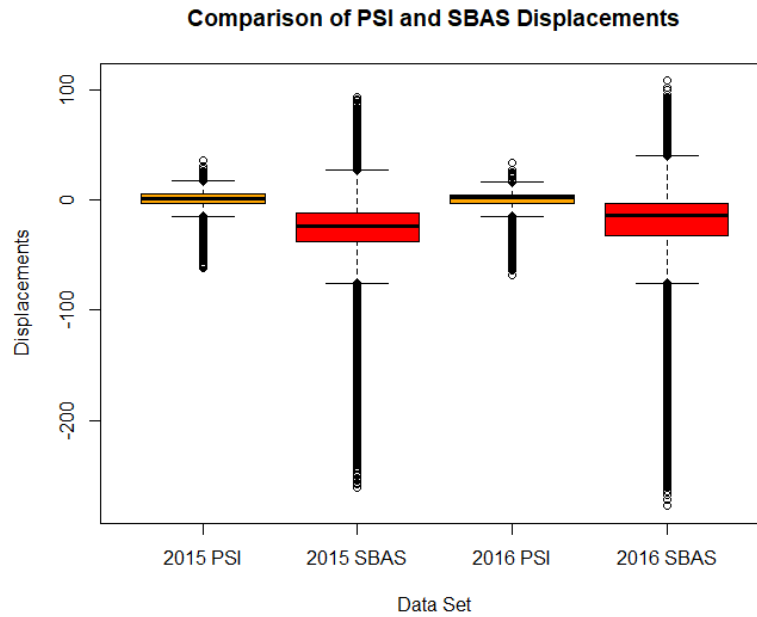
Figure 20. Boxplots showing the variation and average deformation rates measured by the PSI and SBAS methods for 2015 and 2016.

Figure 21 show heat maps associated with the scatterplots shown in figures 19 above. In both figures, there is an identifiable hot spot of points where the PSI measurements show little to no change (- 10 mm/year to 10 mm/year). The main difference in these hotspots is where they correlated with the
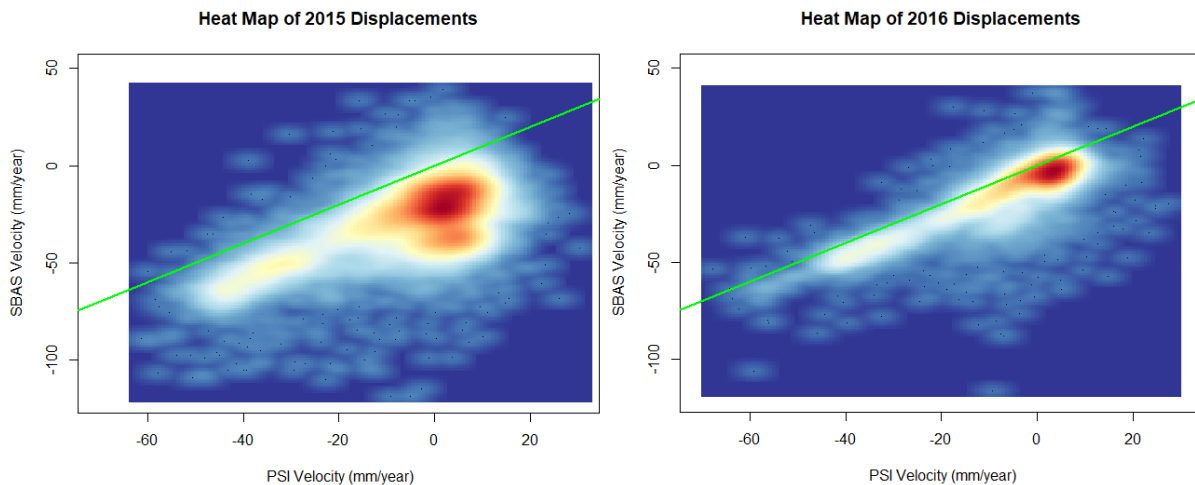
Figure 21. Heat maps showing point density on the scatterplots of PSI and SBAS measurements for 2015 (left) and 2016 (right).

60

SBAS measurements. For 2015, the hot spot shows points experiencing moderate surface subsidence according to the SBAS measurements (-5 mm/year to -45 mm/year). For 2016, the hot spot shows points experiencing little to no change (10 mm/year to -15 mm/year) according to the SBAS, closely resembling the PSI measurements. In addition to the hot spot observed in 2015 showing more subsidence in the SBAS measurements, the hotspot also has more spread across the PSI and SBAS values. Comparatively, the hotspot observed in 2016 shows a tighter grouping of values centered around no change for both datasets.

A similar trend is observed when comparing the displacement measurements made by PSI and SBAS over only urban areas, as classified using the CLC classes. The resulting scatter plots are shown in figure 22 for 2015 and 2016, respectively. Although the overall pattern of measurements does not change, the correlation between measurements shows minor improvement when assessing only urban areas. For 2015, the RMSE and the bias remain the same, however the correlation coefficient increases to 0.606 from 0.597. The 2016 data sets show more improvement, as the bias and RMSE both decrease slightly, to 8.2 mm/year RMSE and -6.7 mm/year bias, relative to the 8.7 mm/year RMSE and -6.9 mm/year bias observed across the entire dataset. There is also a slight improvement to the correlation between measurements, increasing to 0.91 from 0.89, as seen with the 2015 results. The hotspots of points for both scatterplots do not change when assessing only urban areas. The hot spot maps showing the PSI and SBAS measurements for only urban areas are shown in figure 23, for 2015 and 2016, respectively.
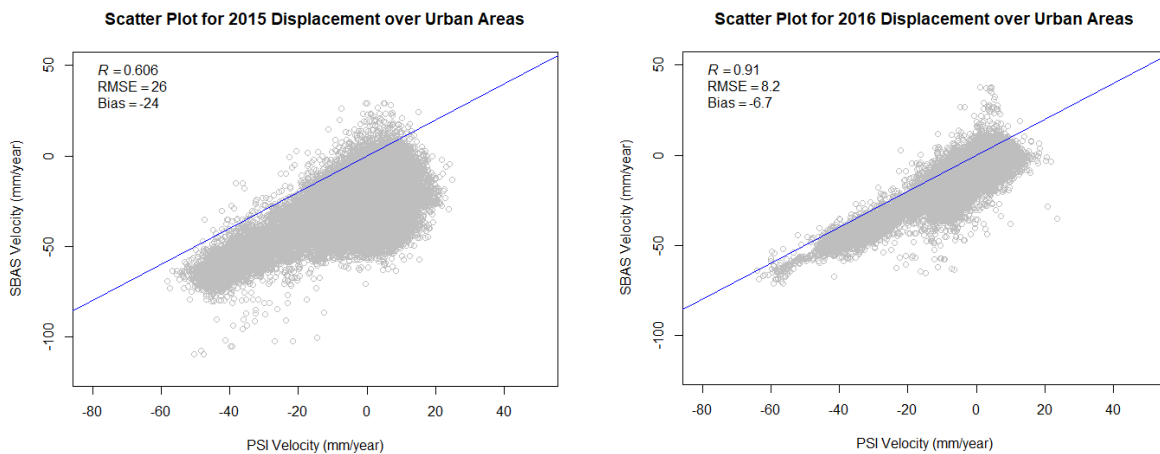
Figure 22. Scatterplots of PSI measurements (x-axis) and SBAS measurements (y-axis) over areas classified as urban using the CLC product for 2015 (left) and 2016 (right). The line of equality is denoted as the blue line.
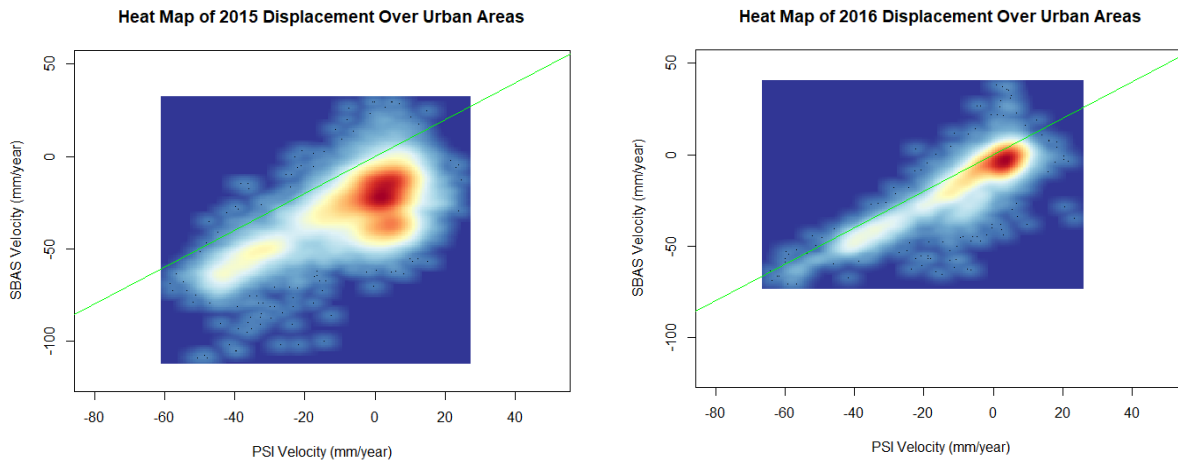
Figure 23. Heat maps showing point density on the scatterplots of PSI and SBAS measurements over areas classified as urban using the CLC product for 2015 (left) and 2016 (right).

5.4 External Uncertainty

Deformation rates in the vertical direction for three GNSS stations are estimated using a regression-based approach. One of these three stations, Titz, is located within the processing extent whereas the other two are outside the extent, as shown in figure 10. Long-term vertical positional changes for the Titz GNSS station are shown in Figure 24, Figure 25 and Figure 26. The Titz station showed a change of -7.6 mm/year for 2015, 0.8 mm/year for 2016 and 3.9 mm/year for the 2015 – 2020 period. Although Mann-Kendall one-sided trend testing showed an insignificant trend for 2016, with a p-value of 0.08, the 2015 and 2015 – 2020 showed significant trends, with p-values significant at the 99% level. However, the direction of trend for the two do not correlate, with 2015 showing a significant downwards trend and the 2015 – 2020 results showing an upwards trend. Although this point is within the processing extent, there are no detected persistent scatterers identified directly over the GNSS station. Therefore, persistent scatterers around the station (R10) are averaged to determine a correlation between deformation rates measured by the GNSS station and the PSI results. The PSI results are converted from LOS displacement to vertical displacements, using equation 30, to correspond with the GNSS measurements. The 2015 PSI results show an average change of 4 mm/year for the area, while 2016 shows an average change of -0.2 mm/year. Neither of these two datasets show a significant downwards trend as indicated in the 2015 Titz station measurements. However, the 2016 PSI results show a sub-millimeter annual deformation rate as reflected in the 2016 and 2015 – 2020 Titz station measurements. Conversely, the 2015 and 2016 SBAS results both show significant downwards trends for the area and for the precise location. The 2015 SBAS results show a deformation rate of -34 mm/year for the precise location and an average rate of -33 mm/year for the area. For 2016, a deformation rate of -4 mm/year is

observed for that location with an average rate of -24 mm/year for the nearby pixels. The significant downward trend as seen in the 2015 Titz station measurements is reflected for both years of the SBAS analysis.
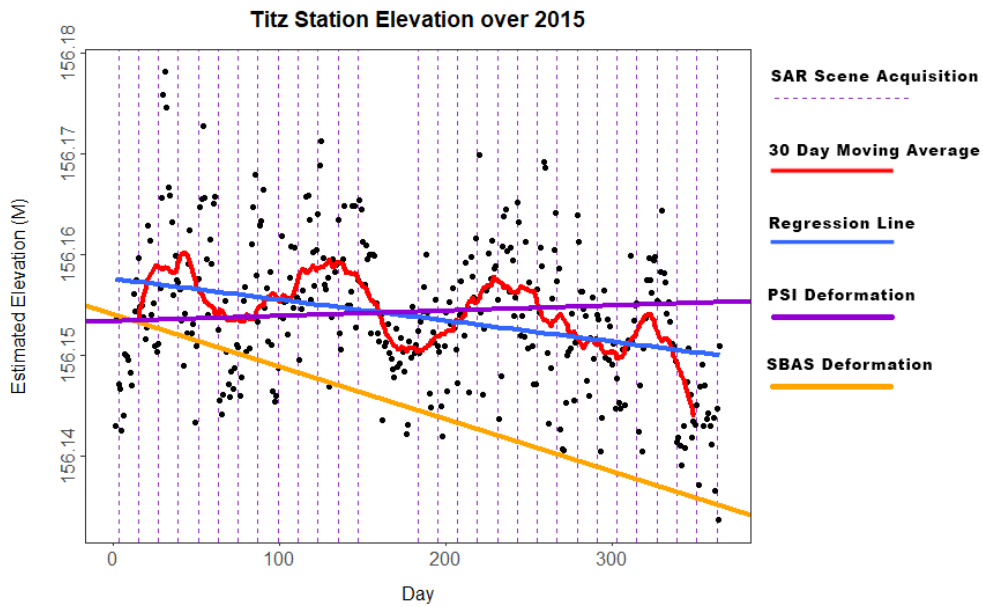
Figure 24. Titz station positional data over 2015 with estimated PSI and SBAS deformation rates superimposed, originating at the 30-day moving average.
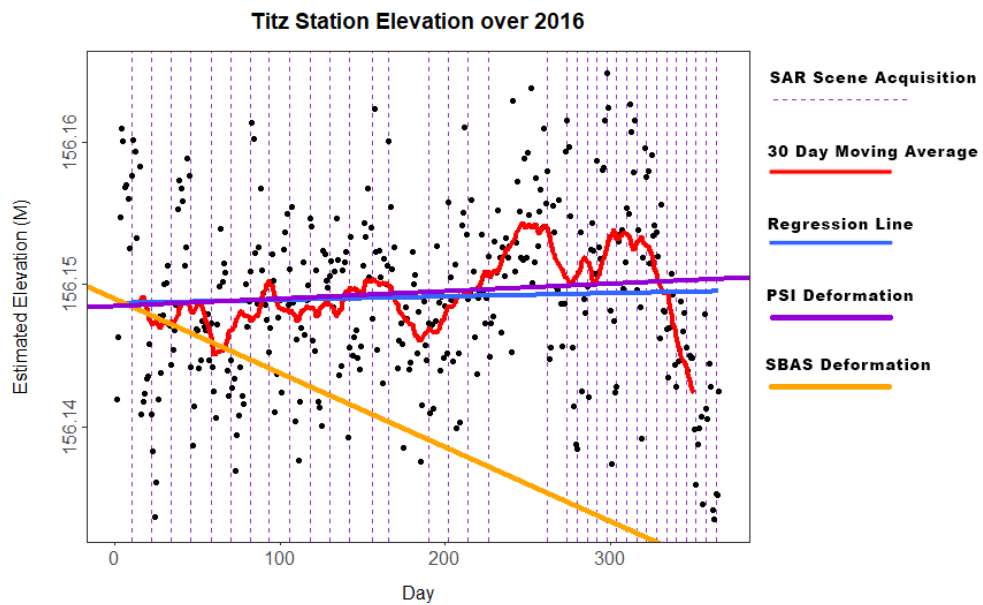
Figure 25. Titz station positional data over 2016 with estimated PSI and SBAS deformation rates superimposed, originating at the 30-day moving average.
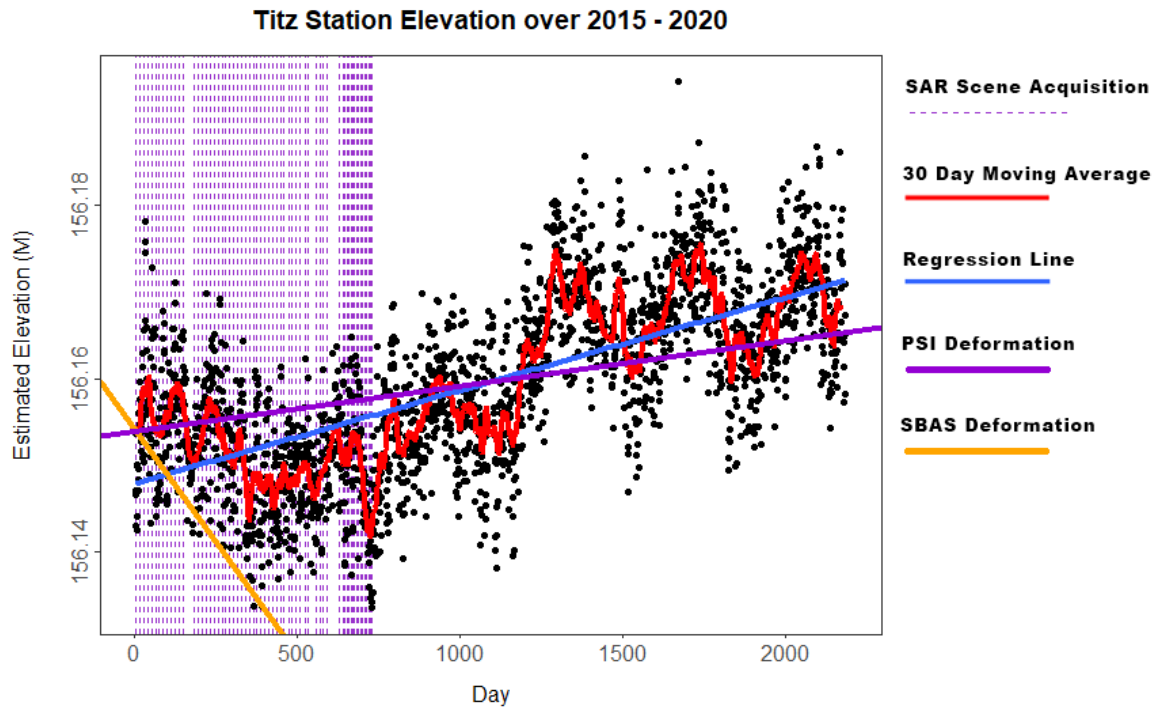
Figure 26. Titz station positional data from 2015 - 2020 with average estimated PSI and SBAS deformation rates from 2015 and 2016 superimposed, originating at the 30-day moving average.

Both the Euskirchen and Eijsden are located outside of the processing. Therefore, the comparison of deformation rates for those two GNSS station are compared to the average displacements of the two techniques used. The Euskirchen station shows upwards movement of 7 mm/year for 2015, and downwards movement of -3.8 mm/year for 2016 and -0.3 mm/year for 2014 – 2020. The trends are shown to be significant using the Mann-Kendall one-sided test with p-values significant at 99%, 95% and 99% for 2015, 2016 and 2014 – 2020, respectively. These deformation trends can be seen in Appendix H. With average deformation rates of -23 mm/year for 2015 and -25 mm/year for 2016, the PSI results do not show good agreement with the 2015 Euskirchen GNSS deformation rates. Although the magnitude of change differs significantly between the two datasets, the average PSI direction of deformation agree well with the 2016 and 2014 – 2020 Euskirchen GNSS deformation. As the SBAS results show average displacements of -25 mm/year for 2015 and -19 mm/year for 2016, the same relationship is observed between the SBAS and Euskirchen measurements.

Similarly, the Eijsden stations shows upward movement of 3.8 mm/year for 2015 and downward movement of -1 mm/year for 2016. Unlike the Euskirchen, an upwards movement of 0.6 mm/year is observed for 2014 – 2020. However, only the 2015 and 2014 – 2020 trends are shown to be significant with p-values significant at the 99% level. Conversely, the 2016 deformation trend is shown to be

insignificant with a p-value of 0.47. Appendix I shows the long-term vertical deformation trends for the Eijsden station. These deformation trends do not agree well with either the SBAS or PSI measurements, showing average movements in the opposite direction for 2015 and 2014 – 2020. The direction of deformation measured by the multi-temporal DInSAR techniques only agree well with the 2016 Eijsden station measurements, which are insignificant. Therefore, the Eijsden station deformation measurements do not agree with the multi-temporal DInSAR observations. However, the variability observed in the Eijsden and Euskirchen stations agree with the variability in measurements observed with the Titz station. This indicates the amount of variability in height measurements of the Titz station seem to be within reason.

Overall, both techniques show similar deformation patterns across the landscape. The SBAS results have a wider coverage of measurements, compared to PSI but also have a higher level of uncertainty. Both techniques were able to identify that the region east of the Hambach mine (R1) exhibits the most significant pattern of deformation across the entire study period. The area of the largest discrepancy between results is observed over Mönchengladbach (R6), primarily when assessing the 2015 SBAS results. In this region, the PSI results show small surface uplift for both years whereas the SBAS results show significant surface subsidence for 2015 and slight surface subsidence for 2016. When comparing the measurements made by the two techniques over only urban regions, the relationship between the two datasets only slightly improves, primarily due to the low omission rate when excluding non-urban scatterers.

Chapter 6

Discussion

The aim of the study was to evaluate the capability of using multi-temporal DInSAR methods to monitor landscape deformation around the Rhenish coalfields in Germany using Sentinel-1 SAR imagery. With this, the goal was to measure and characterize land surface movements around the mine, evaluate the uncertainty in the measurements and compare the results of the two methods used, PSI and SBAS.

6.1 Surface Deformation Measurements

Surface deformation around the Rhenish coalfields was successfully measured for 2015 and 2016 using PSI and SBAS. It was expected that the most severe surface deformation would occur closest to the mining activity due to the large on-going topographic changes resulting from surface extraction. Although this is largely true in the observed deformation patterns, the most severe surface deformation rates are measured usually only on one side of the mining activity. For the Hambach and Inden mines, this deformation is observed to the east of the mining operations, and for the Garzweiler mines, it is observed between the mines and to the west of the operation. This behaviour is caused by the active excavation of over burden moving in the directions of observed surface deformation (Tang et al., 2020). In this case, the active parts of the Inden and Hambach mines are in the eastern portions of the mining pits, whereas the Garzweiler mine is actively excavating overburden from the western portion of the mine. The direction of surface deformation, for the areas close to the mines but not within the mining operation, was expected to be upwards as the removal of nearby overburden would allow the land surface uplift. However, this land experiences significant subsidence due to the compaction process of unconsolidated soil materials and extensive groundwater pumping, which is required for the lignite to be extracted (Tang et al., 2020). Areas of heavy vegetation coverage tend to show moderate rates of surface uplift. This is likely caused by the vegetation canopies being the main source of scattering in these areas, rather than the soil surface below. As a result, the multi-temporal DInSAR techniques are measuring the growth of a vegetation canopy and not the surface movement of the land surface. Much of the urban and built-up parts of the study area experience little to no surface movement, with built-up areas nearest to the mines experiencing the corresponding surface subsidence.

InSAR measurements within the perimeter of the open mining pits are likely to suffer from phase discontinuities as large elevation drops, notably from steep boundary cliffs, are not modeled well in the cost functions used for phase unwrapping (Chen & Zebker, 2000). Such discontinuities are present in the data sets as the extents of the mining pits cannot be omitted from the datasets until several processing

steps have occurred. Phase discontinuities are also expected as the ground displacement within the mine will exceed the limit of change that can occur between image acquisitions (Werner et al., 2002; Pawluszek-Filipiak and Borkowski, 2020). Despite the fast-changing environment, both the PSI and SBAS techniques were able to identify a sufficient number of scatterers across the scene. Further error is introduced with the assumption of spatially correlated nuisance terms (spatially correlated look angle errors and atmospheric noise) not being temporally correlated. In practice, these terms may be spatially and temporally correlated, in which case they are not correctly estimated and removed by image stacking (Hooper et al., 2007). Phase residuals may also contribute unwanted phase signal due to topographic changes occurring from the ongoing production that are not reflected in the DEM used during processing (European Space Agency, 2007; Tang et al., 2020). Although these residuals are often mitigated by stacking the interferograms, the residuals can still propagate to phase unwrapping causing phase ambiguity (Ferretti et al., 2001; Berardino et al., 2002; Fattahi & Amelung, 2015). Improved mitigation against these residuals can be accomplished by using a DEM with higher spatial resolution and less temporal decorrelation from the SAR scenes used (Berardino et al., 2002; Lauknes et al., 2006; Tang et al., 2020). However, even with an up to date DEM available, temporal decorrelation is present in all DInSAR processing as it is a vital component to measuring change. Without any temporal decorrelation between acquisitions, coherence may be very high but there is exists no change to be measured.

The same overall pattern of surface deformation was measured by the PSI and SBAS over the two years. Both techniques measured small scale deformation across the landscape with a prominent area of moderate subsidence observed east of the Hambach mine (R1). The SBAS technique also identified an area of heavy subsidence occurring between the Garzweiler mines that are not measured by the PSI technique. Although similar patterns of surface deformation were observed, the actual measurements of deformation varied substantially between the datasets, as commonly seen in other studies (Lauknes et al., 2006; Lazecký et al., 2010; Liu et al., 2020). This supports the claims of Lazecký et al. (2010), Fárová et al. (2019) and by Pawluszek-Filipiak and Borkowski (2020) that multi-temporal DInSAR techniques may be best suited for the detection of surface deformation and for identifying hot spots of movements but may not be suitable as a stand-alone technique for deformation monitoring. This is further reflected when comparing the measured deformation rates of this study to the deformation rates measured by Tang et al. (2020) over the same area using TerraSAR-X and Sentinel-1 data. Although the patterns of deformation observed in our study closely match those identified by Tang et al. (2020), the maximum subsidence rates differ significantly. In this study, maximum rates of -61 mm/year and -67 mm/year were measured using PSI and rates of -250 mm/year and -260 mm/year were measured using SBAS for 2015

and 2016. Comparatively, Tang et al. (2020) measured rates up to 500 mm/year from 2017 to 2018. It should be noted, the most severe deformation rates measured in that study were observed within the mining pits, which are excluded from processing in this study. However, the deformation rates, primarily around the Hambach mine, measured by Tang et al. (2020) show higher levels of surface subsidence than is measured in this study. The European Space Agency (2020) also measured surface deformation in the region using PSI applied to 2014 – 2019 Sentinel-1 imagery. Although exact deformation rates and details are not reported, the general deformation patterns observed in their study agree well with those measured in this work.

The agreement of deformation directionality is not seen when comparing the deformation measurements to the in-situ GNSS data within the processing extent. The direction of surface movement, along the LoS, for the SBAS and PSI measurements are not the same for the area around the Titz GNSS station (R10). However, the directionality of deformation does agree well with the Euskirchen GNSS station showing significant downwards trends for 2015 and 2014 – 2020. As this station is located outside of the processing extent, direct comparison to the PSI and SBAS measurements over the area is not possible. The Eijsden station does not show strong agreement between the directionality of deformation when compared to the multi-temporal DInSAR measurements. This disagreement is likely caused by spatial decorrelation, as the Eijsden GNSS station is far beyond the processing extent of this study. Thus, comparisons to the Eijsden station may be unreliable.

The Titz station only shows a downwards trend of surface subsidence for 2015 and shows upward trends of surface uplift for 2016 and 2015-2020. For 2015, the PSI measurements show an average surface uplift of 4 mm/year in the region surrounding the station and minimal subsidence of -0.2 mm/year for 2016. Although a slight surface subsidence is observed in 2016 as the average deformation in the area, many of the detected scatterers show surface uplift or little change occurring. Additionally, the lack of persistent scatterers identified in the area means the deformation rate of the precise location of the GNSS station is not measured by the PSI method. Comparatively, the SBAS results have coverage over the GNSS station and show deformation rates of -34 mm/year and -4 mm/year over the precise location. The SBAS results also show average deformation rates of -33 mm/year and -24 mm/year in the surrounding area for 2015 and 2016, respectively, with less variation of LoS directionality. This large discrepancy between datasets is likely the result of agricultural land cover in the area. SBAS tends to perform better than PSI over agricultural areas and can identify a higher density of scatterers (Hooper et al., 2007; Ferretti et al., 2011; Chaabani & Deffontaines, 2020; Pawluszek-Filipiak & Borkowski, 2020).

As a result, the PSI estimates in the area probably accurately capture the displacement of built-up areas while the SBAS technique is measuring surface movement of the agricultural lands.

Both the SBAS and PSI estimates show surface movement in the opposite direction observed by the Titz GNSS station, except for the station's 2015 deformation. However, the PSI for 2015 show a movement in the opposite direction of the station for 2015. This is also true when comparing the observed deformation of the Titz GNSS station to the deformation averages of the PSI and SBAS results for the entire study region. The direction of deformation only matches for the rates measured by the station in 2015 and do not correlate with the GNSS measurements across the 2015-2020 period. Although there remains a discrepancy between the PSI and SBAS measurements in the area, specifically for 2015, the discrepancy between the multi-temporal DInSAR measurements and GNSS station may be caused by the relative vertical accuracy of the GNSS measurements. As the GNSS vertical measurements have a relative accuracy of 3 cm (NovAtel Inc., 2015), the measurements had to be averaged over a longer time span in attempts to mitigate the inaccuracy. However, the overall deformation rate measured by the GNSS station may still largely be the result of this vertical relative accuracy and not the result of actual vertical movement. Thus, it is difficult to state whether the observed deformation rate at the GNSS station is reflective of the real deformation rate occurring at a millimetric scale.

A large portion of the data gathered for each station falls beyond the period of the collected SAR data scenes. As land surface change around mining activities are expected to be non-linear and not exhibiting a constant rate of change, it is possible that some of the observed change to a GNSS station's vertical position may not be reflective of the entire timespan (Pawluszek-Filipiak and Borkowski, 2020; Tang et al., 2020). Without additional in-situ information, it is difficult to determine if the long-term data trends from 2015 – 2020 and 2014 - 2020 are representative of the ground surface phenomena occurring between 2015 and 2016. Therefore, comparison between the multi-temporal DInSAR measurements and the GNSS stations may not be effective due to the vertical inaccuracies of the GNSS measurements and the non-linear nature of the surface deformation.

6.2 Comparison of PSI and SBAS Measurements

It was expected that the PSI results would have significantly less coverage, compared to the SBAS results, but would have a higher confidence in measurements due to the more robust scatterer selection process (Lazecký et al., 2010; Ferretti et al., 2011). This is caused by the requirements of a persistent scatterer to have high coherence across the entire dataset whereas a distributed scatterer only needs to have moderate coherence across most of the dataset (Berardino et al., 2002; Hooper et al., 2007). Additionally, a PSI dataset only needs a minimum of 5 interferometric pairs to be able to produce reliable

results (Hooper et al., 2007). Comparatively, SBAS requires a large amount of SAR scenes and interferometric pairs to accurately measure deformation, even with ideal baselines (Pawluszek-Filipiak and Borkowski, 2020). This is most evident in the comparison between the 2015 and 2016 SBAS deformation measurements. By having the additional 6 SAR scenes in the latter half of 2016, SBAS was able to leverage an additional 45 interferometric pairs. The increased number of pairs helped mitigate against atmospheric effects, temporal decorrelation and orbital artefacts by further reducing the average baselines between interferometric pairs (Berardino et al., 2002; Lauknes et al., 2006; Fattahi & Amelung, 2015). As a result, the 2016 SBAS deformation measurements show less variation in estimated rates and less deviation from the PSI measurements. It also shows a lower average deformation rate across the entire scene, which is expected. Although the inclusion of additional SAR scenes within the given time also improves the PSI estimates, allowing for further discrimination against non-persistent scatterers, the observed impact on the final deformation estimates is less significant.

The two techniques were able to identify a similar overall pattern of deformation across the study area, with a hotspot of surface deformation observed east of the Hambach mine (R1) in all four data sets. This region of moderate subsidence agrees well with the deformation patterns observed by the European Space Agency (2020) and Tang et al. (2020). The city north of the Garzweiler mines (R6), Mönchengladbach, shows the most pronounced difference between the four produced deformation estimates. At this location, the PSI measurements show little change between the two years, exhibiting vertical movement in the upwards direction for both years. Comparatively, the SBAS measurements shows a high amount of change between the two years, with average rates of -35 mm/year and -3 mm/year for 2015 and 2016, respectively. Although both SBAS datasets show an average downwards movement in this area, the 2016 dataset shows more moderate deformation rates with many pixels showing upwards movement. For the 2016 results, the mixture detected targets showing upwards and downwards movement may be caused by the contribution of the 2π phase ambiguity while phase unwrapping (Chen & Zebker, 2000). As for the 2015 SBAS measurements over this region, the large downward movement observed may be caused by atmospheric contributions to the phase propagating through the interferometric pairs.

As increasing the number of interferometric pairs improves the estimates of atmospheric noise for removal, the decreased number of available SAR scenes for 2015 increases the phase contributions of atmospheric artefacts. A similar phenomenon is observed by Tang et al. (2020) resulting in a large area showing downwards movement close to the Garzweiler open mining pits. This behaviour in the SBAS dataset is the result of the multi-master approached used, allowing atmospheric signal delays within a

single image to be propagated through several interferometric pairs. By comparison, unless the atmospheric contributions are present in the master image using in PSI, the atmospheric artefacts will only be present in one interferometric pair and then reduced throughout the image stack. These atmospheric artefacts could be further mitigated by extending the study period of the data sets to include more SAR dates, but this would likely result in a loss of data (Lazecký et al, 2010). Additionally, this would introduce more temporal decorrelation within the datasets, primarily for the PSI which uses a single reference image for all interferometric pairs. SBAS would be less impacted by the temporal decorrelation by applying temporal baseline thresholds to the interferometric pairs.

A notable difference between the two techniques used is the difference of coverage for deformation estimates. As PSI has a more discriminatory scatterer selection process, the resulting deformation estimates omit many agricultural fields and heavily forested areas. As expected, the PSI technique, like traditional DInSAR, was not able to detect persistent scatterers over water bodies and heavily vegetated regions due to decreased backscattering and lower coherence stability across the study period. By contrast, most of the water dominated or heavily vegetated areas were detected by SBAS because of lower coherence requirements used for target selection. As a result, the SBAS technique was able to produce deformation estimates of nearly full coverage across the scene. However, although a larger coverage was produced, the confidence of deformation estimates over these areas is reduced due to the inherently low coherence. This is reflected in the high RMS values observed over the agricultural regions, indicating large errors typically attributed to atmospherics or unwrapping errors (Simons et al., 2002; Tang et al., 2020). This increased coverage does, however, provide additional information that can be used to fill in the gaps of PSI and in-situ measurements and provide a larger synoptic view of land deformation patterns in the region, as discussed by Pawluszek-Filipiak and Borkowski (2020). It should be noted that a higher D_A value for the PSI preprocessing could be used to increase the number of detected scatterers in the final PSI estimates. However, this would decrease the reliability of deformation measurements made with this technique and introduce more overall unwanted phase contributions from error sources.

When comparing the measurements of PSI and SBAS over urban areas, the relationship between the two datasets only becomes slightly improved. It is expected that when comparing over preferable landcover, the agreement between the two datasets would significantly improve. However, majority of the detected persistent scatterers were over areas classified as urban by the CLC product, resulting in a low omission rate when excluding non-urban scatterers. Thus, this comparison provides little insight to the accuracy of the SBAS measurements over the agricultural portions of the landscape. Majority of the

detected persistent scatterers that are not located over classified urban areas are still built up targets surrounded by non-built up areas. The spatial resolution of the CLC product, which is 100 meters, and the thematic accuracy of 85% means that a lot of the smaller built-up areas within agricultural regions are not classified as urban within the classification schema used and therefore are omitted from the urban comparisons. However, the agreement between the two datasets still improved even with this consideration as the SBAS technique is likely detecting distributed scatters around the built-up region and averaging the phase through a low-pass moving window as part of the cost pathway function used for unwrapping. As a result, the two techniques could be measuring the deformation of different targets over the same geographical location causing a discrepancy between the measurements, so the omission of these targets increases the agreement between the techniques. This behaviour is not well reflected in the 2015 urban comparisons due to the 2015 SBAS over estimation of land subsidence occurring in the northern city (R6) likely caused by atmospheric contributions. As such, omitting this region from the urban comparisons would likely show a stronger agreement between the 2015 datasets.

Generally, when no a priori knowledge is available, a constant-rate model of phase variation in time is commonly applied, assuming a simplified linear change is being detected (Pawluszek-Filipiak & Borkowski, 2020). Although this assumption allows for multi-temporal DInSAR to be completed without up to date DEM data, mining-relating subsidence tends to be highly non-linear. As SBAS has the capability to measure non-linear deformations, whereas PSI is focused on measuring linear deformation trends, the SBAS technique is expected to perform better when measuring mining-induced land subsidence (Anderssohn and Riedmann, 2014). This was not found to be true in this study, likely due to the lack of SAR data needed for the data driven SBAS approach to measure deformation rates to a high level of accuracy (Lazecký et al., 2010; Pawluszek-Filipiak & Borkowski, 2020). Therefore, even when assuming a linear deformation rate over an area which likely has a non-linear deformation pattern, the PSI results showed higher precision over the study area. The high precision of the PSI results may also be attributed to the presence of desirable landcover in the area, with a large amount of urban and built up areas being scattered across the landscape.

6.3 Limitations

Although the launch of Sentinel-1 B on April 25th, 2016 decreased the revisit period of the project from 12 days to 6 days, much of this study relies on the longer revisit time of 12 days. During this time, temporal gaps exists within the time series, limiting the number of interferometric pairs that can be generated for a given time, especially with the SBAS techniques, and increasing the temporal decorrelation between acquisitions. Although some temporal decorrelation is required to detect long-term

change, the expected ground displacement within the open mining pits exceed the limits of change that can occur between acquisitions (Werner et al., 2002; Pawluszek-Filipiak and Borkowski, 2020). As a result, the mining pits were excluded from the processing and only the regions around the open pits were analyzed. Additionally, by not having access to more data scenes, the SBAS technique cannot effectively minimize the temporal baselines between all pairs to reach a high level of accuracy. These relatively large temporal baselines, along with the small perpendicular baselines, make Sentinel-1 not an ideal platform for DEM generation using InSAR techniques. As such, the available data could not be used to produce more up-to date DEMs of the region, representative of the topographic changes occurring from the ongoing production (European Space Agency, 2007; Tang et al., 2020). Instead, the SRTM-3 DEM which was developed using 2009 data was used as the external reference data source. With this, there remains significant unwanted phase contribution from phase residuals and unaccounted topographic changes that are propagated through to the unwrapping process.

The small perpendicular baselines of Sentinel-1 data cause very small DEM errors in the deformation results, even when assessing active mining operations where the topography is constantly changing, and mitigate against most of the phase residuals caused by using out of date DEM data. However, the short wavelength of Sentinel-1 caused a loss of coherence, especially over areas with heavy vegetation or water coverage. As a result, measurements over urban areas are expected to be considerably more reliable. Fortunately, the region studied has a lot of preferable landcover for InSAR, such as built-up areas or areas with light vegetation. However, preforming the same analysis over a more arid environment is likely to increase the average coherence of interferograms, aiding with the phase unwrapping and improving the confidence of results.

Another limitation of using Sentinel-1 data is the available spatial resolutions. As ground range resolution represents the ability to discriminate features that are on the Earth's surface, higher spatial resolutions allow for higher confidence of a particular target being detected within a pixel (Woodhouse, 2006). By having a pixel size of 2.3 meters by 14.1 meters, the likelihood of containing mixed pixels increases significantly over regions where built-up areas are surrounded by agricultural lands, as seen in this study area. This becomes a further issue after filtering which reduces the spatial resolution and can make phase unwrapping in areas of large deformation gradients challenging (Samsonov et al., 2015). A similar issue arises with the 90-meter resolution of the reference DEM used, SRTM-3, as the large differences in resolution compared to the Sentinel-1 data is likely to result in co-registration issues and incorrect reference heights being assigned to Sentinel-1 pixels. The 100 meters spatial resolution of the CLC data product raises a similar concern. It is difficult to properly determine the proper classification

of a given pixel or detected scatterer when the CLC resolution is much greater than that of the Sentinel-1 data.

The limited in-situ data available made external validation of results difficult to complete. The 3 cm vertical relative accuracy of the GNSS data creates significant uncertainty when analyzing millimetric-scale vertical displacement. Therefore, direct comparison to these stations may not reliable for the scale of measurements made. Additionally, there is not enough GNSS station data available, with only one station being located within the processing extent. Preferably, more GNSS station data alongside surveying or LiDAR data would be available for external validation of measurements. As groundwater pumping due to mining activities were shown to be a major cause of surface subsidence around mining activities, the availability of ground water data could prove useful for external validation of deformation trends (Chaabani and Deffontaines, 2020; Liu et al., 2020; Tang et al., 2020).

6.4 Future Work

Further work should focus on an expanded set of in-situ measurements mentioned above, increased SAR scenes used (both Sentinel-1 and TerraSAR-X) and installation of a large GNSS network to characterize widespread surface deformation. In-situ measurements can be expanded by including ground water data from piezometric data. This would provide insight to the relationship between ground surface displacements and mining-relate excessive ground water extraction. This data coupled with detailed overburden extraction rates would allow for a better understanding of the correlation between the mining production and the subsidence in the region and could provide insight to geotechnical risks of the mines. High accuracy leveling or LiDAR data could also be used to validate deformation rates across a larger area than the single point GNSS data available in this study. The techniques used in this study should be compared and calibrated using this additional in-situ measurements when available. Increasing the amount of SAR scenes used would increase the robustness of both the PSI and SBAS techniques. This impact should be more prominently observed in the SBAS processing, as seen when comparing the 2015 to the 2016 results. Although the short perpendicular baselines of Sentinel-1 help minimize the DEM error, a more up-to date DEM would reduce the phase residuals in processing. Additionally, a DEM with a finer spatial resolution would reduce the coregistration errors that may be present and improve the reliability of measurements.

Ideally, a DEM would be generated at the start of the study periods with pixel spacing matching the Sentinel-1 data. Although the matching pixel spacings cannot be achieved, the temporal decorrelation of the DEM can be reduced by using TerraSAR-X and TanDEM-X bi-static data. A series of DEMs could be generated using the TanDEM-X CoSSC image pairs across the study period. This would allow for the

ability to use a differencing of DEMs approach to create a time series of displacements that could be used as another validation dataset. The bi-static nature of the TanDEM-X data could be also be used to include the open mining pits in the processing as the minimal temporal difference between acquisitions would not suffer from the same temporal decorrelation issues faced with the Sentinel-1 data. This would expand the capabilities of the study to also monitor slope instability within the mining pits. Access to TanDEM-X data would also provide higher spatial resolutions that can be leveraged to provide more detailed information of ground displacement in the region. The shorter wavelength of this data would also provide higher sensitivity to slow and small displacements but would also be more sensitive to temporal decorrelation as a result (Tang et al., 2020). Lastly, improved GNSS coverage would allow for a more detailed understanding of ground surface deformations in the region that could be directly compared to the DInSAR measurements.

6.5 Applications

The research preformed in this study provide an insight to the benefits and limitations of using multi-temporal DInSAR techniques to monitor mining-induce land surface changes. The major benefit of these techniques is the ability to measure large scale deformation rates at high spatial resolutions with limited in-situ data. Traditionally, monitoring of surface movement is completed using tilt meters and GPS meters deployed at predefined areas of high risk (Paerse et al., 2014). Remote sensing techniques allow for surface monitoring in hard to access regions where deployment of such instruments can be difficult or impossible. Even when traditional monitoring techniques are used, multi-temporal DInSAR can be used to bridge the measurement gaps and provide a more detailed insight to the large-scale land deformation patterns. This is particularly true over preferable environments, such as arid landscapes, where the expected coherence is high and omission rates of scatterers is low. However, these methods are limited when used to monitor land surface deformation over heavily vegetated areas, or regions that experience very high seasonal fluctuations due to the high loss of coherence.

This gives way to large-scale ground stability assessments that are otherwise costly, laborious and time consuming using traditional methods. In cases where bi-static data, such as TanDEM-X data, is available, these techniques can be used to monitor changes occurring within the mining pits. This can be used not only to monitor extraction but also for monitoring slope instability and landslide hazards (Tang et al., 2020). This information provides decision makers with quantitative data that can aid with policy and safety regulations regarding extractive industries and excessive ground water pumping. This indicates that multi-temporal DInSAR techniques can be used a cost-effective and complementary method to conventional techniques for monitoring fast mining subsidence over preferable landscapes.

However, it should be noted that InSAR is not a suitable replacement for real-time monitoring applications for extractive operations due to the long repeat time between image acquisitions and the time required to process the data (Paerse et al., 2014). Additionally, without the inclusion of accurate in-situ data, multi-temporal DInSAR techniques are often not able to accurate measure surface deformation rates. Even when deployed over preferable landscapes, these techniques are best suited to provide insight towards whether a given area is experiences subsidence or surface uplift and can be used to identify regions of severe ground displacement. As such, multi-temporal DInSAR methods are not suitable as a stand-alone replacement for conventional in-situ techniques (Paerse et al., 2014; Pawluszek-Filipiak and Borkowski, 2020).

Chapter 7

Conclusion

The conclusions are articulated to address the original objectives described in Chapter 1.2. The following three sections address each of these objectives.

7.1 Land Surface Movement

Ground surface deformation is one of the most essential issues when assessing safety and environmental impacts of open-pit mines. Due to the logistical issues commonly present with traditional monitoring techniques, remote sensing solutions have become increasingly popular to handle such tasks (Lazecký et al., 2010; Ji et al., 2016). These ground surface deformations were measured in the Rhenish coalfields in Germany, using Sentinel-1 data for 2015 and 2016. For both years, there is a consistent pattern of large scale, small surface deformation across the scene with the PSI technique showing small scale surface uplift and the SBAS showing small scale surface subsidence. All four sets of results show moderate amounts of surface subsidence occurring close to the active parts of each mining pit. For the Hambach and Inden mines, this is the eastern side, and for the Garzweiler mine, this is the western side. Both techniques identified a similar hotspot of surface deformation, exhibiting significant subsidence, east of the Hambach mine. The SBAS technique also identified another hotspot of heavy subsidence occurring between the two Garzweiler mines that was not measured by the PSI technique. The deformation patterns observed in this study agree with those measured by Tang et al. (2020) and the European Space Agency (2020).

7.2 Performance Differences Between PSI and SBAS

Deformation measurements over the Rhenish coalfields using multi-temporal DInSAR techniques, namely SBAS and PSI, were compared to determine the performance difference between the two methods. The PSI results showed significantly lower variation in measurements but had a severely limited spatial coverage when compared with the SBAS measurements. Comparisons of annual deformation estimates between the two techniques showed that 2015 exhibited high RMSE and bias values of 26 mm/year and -24 mm/year for SBAS and PSI methods respectively. Comparatively, the 2016 comparisons only showed RMSE and bias values of 8.7 mm/year and -6.9 mm/year. This discrepancy between performance differences is mainly caused by a large clustering of points with surface subsidence rates that are overestimated by the 2015 SBAS measurements. This overestimation is likely the result of atmospheric artefacts that propagated through the image stack into the phase unwrapping (Tang et al., 2020). The atmospheric contributions may have had a larger impact in this year due to the decreased availability of SAR scenes which will have reduced the atmospheric mitigation capacity of the approach,

since the Sentinel-1B mission had not yet launched. By having access to an additional 6 SAR scenes across the year, the 2016 SBAS process was able to produce an additional 45 interferograms. The additional 45 interferograms helped mitigate the contribution to atmospheric effects by the averaging them out across the entire data set.

The atmospheric effects are also significantly more prominent in the SBAS results than the PSI results due to the nature of the interferometric pairing completed by both techniques. As PSI only creates interferograms using a single master, any atmospheric contributions (unless present in the master image) can only be observed in one interferogram. Comparatively, the SBAS process can use a single slave image to form multiple interferograms, further propagating the atmospheric artefacts to the phase unwrapping. As such, the SBAS techniques benefits more heavily from additional data, within a given temporal period, than the PSI technique. When data is limited, the PSI technique proves to be more reliable for measuring annual deformation rates. Despite these challenges, both techniques observed the same overall deformation patterns across the scene. Although the direction of surface movement agreed well between datasets, the exact deformation values varied; this has been observed in previous studies (Lauknes et al., 2006; Lazecký et al., 2010; Liu et al., 2020).

Assessing the performance differences between the two techniques only over areas classified as urban using the CLC product showed little improvement. The 2015 comparisons showed an RMSE of 26 mm/year and a bias of -24 mm/year while the 2016 comparisons showed an RMSE of 8.2 mm/year and a bias of -6.7 mm/year. This small performance improvement is mainly contributed to the poor spatial resolution of the CLC product and the target selection process of the PSI method. Due to the coherent nature of persistent scatterers, the targets detected by PSI are primarily over urban areas. Therefore, exclusion of non-urban areas from the measurement comparisons does not omit a significant portion of the datasets.

7.3 Comparison with GNSS Measurements

Although there is not a strong agreement between the external GNSS station data and the multi-temporal DInSAR deformation estimates, there is a large amount of uncertainty of the GNSS measurements. As the GNSS measurements have a relative vertical accuracy of 3 cm (NovAtel Inc., 2015), the uncertainty in these measurements may be too large to meaningfully compare to the millimetric-scale deformation measurements made by the multi-temporal DInSAR techniques. Furthermore, detailed ground surveying data and ground water table measurements would be useful to improve the external validation process. As the mining operations present non-coherent processes, DInSAR observations over the area using repeat-pass monostatic systems poses challenges relating to

decorrelation and phase ambiguity. Using single-pass InSAR data, such as TanDEM-X, would resolve this issue and facilitate increased height and spatial resolutions and improved coverage of the study area.

The results of the multi-temporal DInSAR deformation measurements over the Rhenish coalfields show the potential of using InSAR techniques for monitoring large scale mining-induce surface changes. These techniques offer a solution for measuring surface displacements in hard to access areas, with lower cost and labour requirements compared to traditional monitoring techniques. InSAR measurements can also be used to fill the measurement gaps of the traditional monitoring techniques that tend to have limited spatial and temporal coverage. However, due to the relatively long repeat times between image acquisitions and the time required for processing data, InSAR is not a suitable replacement for real-time monitoring of extractive operations (Paerse et al.; 2014). Due to the capability of identifying areas of surface deformation and the inability to produce precise deformation measurements, multi-temporal DInSAR techniques are not suitable as a stand-alone replacement for conventional in-situ techniques (Paerse et al., 2014; Pawluszek-Filipiak and Borkowski, 2020).

References

Alaska Satellite Facility. (n.d.). [Image of Typical Side-Looking Radar Pointing Perpendicular to The Flight Direction]. Retrieved February 7, 2020, from https://asf.alaska.edu/information/sar-information/what-is-sar/

Anderssohn, J., & Riedmann, M. (2014, June). Use of Bi-and Monostatic Interferometry of an Open Pit Mining Area in Germany. In *EUSAR 2014; 10th European Conference on Synthetic Aperture Radar* (pp. 1-4). VDE.

Berardino, P., Fornaro, G., Lanari, R., & Sansosti, E. (2002). A new algorithm for surface deformation monitoring based on small baseline differential SAR interferograms. *IEEE Transactions on geoscience and remote sensing*, *40*(11), 2375-2383.

Braun, A., & Veci, L. (2020). TOPS Interferometry Tutorial. *Array Systems. Available online: http://step. esa. int/docs/tutorials/S1TBX% 20TOPSAR% 20Interferometry% 20with% 20Sentinel-1% 20Tutorial_v2. pdf (accessed February 2020)*.

Canaslan, F., & Ustun, A. (2012, May). Impact of perpendicular and temporal baseline characteristics on InSAR coherence maps. In *Proc. FIG Working Week*.

Chaabani, A., & Deffontaines, B. (2020). Application of the SBAS-DInSAR technique for deformation monitoring in Tunis City and Mornag plain. *Geomatics, Natural Hazards and Risk*, *11*(1), 1346-1377.

Chen, C. W., & Zebker, H. A. (2000). Network approaches to two-dimensional phase unwrapping: intractability and two new algorithms. *JOSA A*, *17*(3), 401-414.

Chen, J., Lin, H., Huang, C., & Fang, C. (2009). The relationship between the leaf area index (LAI) of rice and the C-band SAR vertical/horizontal (VV/HH) polarization ratio. *International Journal of remote sensing*, *30*(8), 2149-2154.

Chen, Y., Qiao, S., Zhang, G., Xu, Y. J., Chen, L., & Wu, L. (2020). Investigating the potential use of Sentinel-1 data for monitoring wetland water level changes in China's Momoge National Nature Reserve. *PeerJ*, *8*, e8616.

de Leeuw, M. R., & de Carvalho, L. M. T. (2009). Performance evaluation of several adaptive speckle filters for SAR imaging. Anais XIV Simpósio Brasileiro de Sensoriamento Remoto, 7299-7305.

Donahue, M., 2018. Ancient Forest Home of Squatter Communities Is Doomed by Coal [WWW Document]. Natl. Geogr. Mag. URL.https://www.nationalgeographic.com/news/2018/04/hambach-forest-germany-logging-coal-conservation-science/

Ebmeier, S. K., Biggs, J., Mather, T. A., Elliott, J. R., Wadge, G., & Amelung, F. (2012). Measuring large topographic change with InSAR: Lava thicknesses, extrusion rate and subsidence rate at Santiaguito volcano, Guatemala. *Earth and Planetary Science Letters*, *335*, 216-225.

European Space Agency (2007). *EnviSat ASAR Product Handbook* [2.2]. Retrieved June 01, 2019, from https://earth.esa.int/pub/ESA_DOC/ENVISAT/ASAR/asar.ProductHandbook.2_2.pdf

European Space Agency (2020). *Germany Land Motion Mapped.* Retrieved May 27, 2021, from https://www.esa.int/Applications/Observing_the_Earth/Copernicus/Sentinel-1/Germany_land_motion_mapped

Fárová, K., Jelének, J., Kopačková-Strnadová, V., & Kycl, P. (2019). Comparing DInSAR and PSI techniques employed to Sentinel-1 data to monitor highway stability: A case study of a massive dobkovičky landslide, Czech Republic. *Remote Sensing*, *11*(22), 2670.

Fattahi, H., & Amelung, F. (2014). InSAR uncertainty due to orbital errors. *Geophysical Journal International*, *199*(1), 549-560.

Fattahi, H., & Amelung, F. (2015). InSAR bias and uncertainty due to the systematic and stochastic tropospheric delay. *Journal of Geophysical Research: Solid Earth*, *120*(12), 8758-8773.

Ferretti, A., Prati, C., & Rocca, F. (2001). Permanent scatterers in SAR interferometry. *IEEE Transactions on geoscience and remote sensing*, *39*(1), 8-20.

Ferretti, A., Monti-Guarnieri, A., Prati, C., Rocca, F., & Massonnet, D. (2007). InSAR Principles: Guidelines for SAR Interferometry Processing and Interpretation. ESA Publication TM-19.

Ferretti, A., Fumagalli, A., Novali, F., Prati, C., Rocca, F., & Rucci, A. (2011). A new algorithm for processing interferometric data-stacks: SqueeSAR. *IEEE transactions on geoscience and remote sensing*, *49*(9), 3460-3470.

Flores-Anderson, A. I., Herndon, K. E., Thapa, R. B., & Cherrington, E. (2019). The SAR Handbook: Comprehensive Methodologies for Forest Monitoring and Biomass Estimation.

Gagnon, L., & Jouan, A. (1997, October). Speckle filtering of SAR images: a comparative study between complex-wavelet-based and standard filters. In Wavelet Applications in Signal and Image Processing V (Vol. 3169, pp. 80-92). International Society for Optics and Photonics.

Hanssen, R. F. (2001). *Radar interferometry: data interpretation and error analysis* (Vol. 2). Springer Science & Business Media.

Hooper, A., Zebker, H., Segall, P., & Kampes, B. (2004). A new method for measuring deformation on volcanoes and other natural terrains using InSAR persistent scatterers. *Geophysical research letters*, *31*(23).

Hooper, A., Segall, P., & Zebker, H. (2007). Persistent scatterer interferometric synthetic aperture radar for crustal deformation analysis, with application to Volcán Alcedo, Galápagos. *Journal of Geophysical Research: Solid Earth*, *112*(B7).

Hooper, A. (2008). A multi-temporal InSAR method incorporating both persistent scatterer and small baseline approaches. *Geophysical Research Letters*, *35*(16).

Lazecký, M., Jiránková, E., & Böhmová, D. (2010). Usage of InSAR techniques to detect and monitor terrain subsidence due to mining activities.

Lauknes, T. R., Dehls, J., Larsen, Y., Høgda, K. A., & Weydahl, D. J. (2006, February). A comparison of SBAS and PS ERS InSAR for subsidence monitoring in Oslo, Norway. In *Fringe 2005 Workshop* (Vol. 610).

Lauknes, T. R., Shanker, A. P., Dehls, J. F., Zebker, H. A., Henderson, I. H. C., & Larsen, Y. (2010). Detailed rockslide mapping in northern Norway with small baseline and persistent scatterer interferometric SAR time series methods. *Remote Sensing of Environment*, *114*(9), 2097-2109.

Lawal, A. D., Radice, G., Ceriotti, M., & Makarfi, A. U. (2016). Investigating SAR algorithm for spaceborne interferometric oil spill detection. *International Journal of Engineering and Technical Research*, *4*(3), 123-127.

Li, Z., Fielding, E. J., Cross, P., & Preusker, R. (2009). Advanced InSAR atmospheric correction: MERIS/MODIS combination and stacked water vapour models. *International Journal of Remote Sensing*, *30*(13), 3343-3363.

Li, S., Zhang, S., Li, T., Gao, Y., Chen, Q., & Zhang, X. (2020). Modeling the optimal baseline for a spaceborne bistatic sar system to generate dems. *ISPRS International Journal of Geo-Information*, *9*(2), 108.

Liu, L., Yu, J., Chen, B., & Wang, Y. (2020). Urban subsidence monitoring by SBAS-InSAR technique with multi-platform SAR images: a case study of Beijing Plain, China. *European Journal of Remote Sensing*, *53*(sup1), 141-153.

Ji, L., Zhang, Y., Wang, Q., Xin, Y., & Li, J. (2016). Detecting land uplift associated with enhanced oil recovery using InSAR in the Karamay oil field, Xinjiang, China. International Journal of Remote Sensing, 37(7), 1527-1540.

Khakim, M. Y. N., Tsuji, T., & Matsuoka, T. (2012). Geomechanical modeling for InSAR-derived surface
 deformation at steam-injection oil sand fields. Journal of Petroleum Science and Engineering, 96, 152-
 161.

Khakim, M. Y. N., Tsuji, T., & Matsuoka, T. (2013). Detection of localized surface uplift by differential SAR
 interferometry at the hangingstone oil sand field, Alberta, Canada. *IEEE Journal of Selected Topics in
 Applied Earth Observations and Remote Sensing*, *6*(6), 2344-2354.

Meinen, B. U., & Robinson, D. T. (2020). Mapping erosion and deposition in an agricultural landscape:
 Optimization of UAV image acquisition schemes for SfM-MVS. *Remote Sensing of Environment*, *239*,
 111666. https://doi.org/10.1016/j.rse.2020.111666

Moreira, A., Prats-Iraola, P., Younis, M., Krieger, G., Hajnsek, I., & Papathanassiou, K. P. (2013). A tutorial on
 synthetic aperture radar. *IEEE Geoscience and remote sensing magazine*, *1*(1), 6-43.

National Resources Canada. (2015) [Image of Polarization of a Plane Electromagnetic Wave]. Retrieved May
 10, 2020, from https://www.nrcan.gc.ca/maps-tools-publications/satellite-imagery-air-photos/remote-
 sensing-tutorials/microwave-remote-sensing/radar-polarimetry/9275

National Resources Canada (2020). *Precise Point Positioning.* Retrieved April 20, 2021, from
 https://webapp.geod.nrcan.gc.ca/geod/tools-outils/ppp.php?locale=en

NovAtel Inc. (2015). *An Introduction to GNSS: GPS, GLONASS, BeiDou, Galileo and other Global
 Navigation Satellite Systems* [2]. Retrieved May 3, 2021, from https://novatel.com/an-introduction-to-
 gnss

Onn, F., & Zebker, H. A. (2006). Correction for interferometric synthetic aperture radar atmospheric phase
 artifacts using time series of zenith wet delay observations from a GPS network. *Journal of
 Geophysical Research: Solid Earth*, *111*(B9).

Pawluszek-Filipiak, K., & Borkowski, A. (2020). Integration of DInSAR and SBAS Techniques to determine mining-related deformations using sentinel-1 data: The case study of Rydułtowy mine in Poland. *Remote Sensing*, *12*(2), 242.

Pearse, J., Singhroy, V., Samsonov, S., & Li, J. (2014). Anomalous surface heave induced by enhanced oil recovery in northern Alberta: InSAR observations and numerical modeling. Journal of Geophysical Research: Solid Earth, 119(8), 6630-6649.

Rosen, P. A., Hensley, S., Joughin, I. R., Li, F. K., Madsen, S. N., Rodriguez, E., & Goldstein, R. M. (2000). Synthetic aperture radar interferometry. *Proceedings of the IEEE*, *88*(3), 333-382.

Samsonov, S. V., Czarnogorska, M., & Charbonneau, F. (2015). Selecting optimal RADARSAT constellation mission beams for monitoring ground deformation in Alberta's oil sands. Canadian Journal of Remote Sensing, 41(5), 390-400.

Simons, M., Y. Fialko, and L. Rivera (2002), Coseismic Deformation from the 1999 Mw 7.1 Hector Mine, California, Earthquake as Inferred from InSAR and GPS Observations, *Bulletin of the Seismological Society of America*, *92*(4), 1390-1402.

Tang, W., Motagh, M., & Zhan, W. (2020). Monitoring active open-pit mine stability in the Rhenish coalfields of Germany using a coherence-based SBAS method. *International Journal of Applied Earth Observation and Geoinformation*, *93*, 102217.

Touzi, R. (1999, June). On the use of polarimetric SAR data for ship detection. In *IEEE 1999 International Geoscience and Remote Sensing Symposium. IGARSS'99 (Cat. No. 99CH36293)* (Vol. 2, pp. 812-814). IEEE.

Wang, R., & Deng, Y. (2018). Fundamentals of bistatic SAR. In *Bistatic SAR System and Signal Processing Technology* (pp. 1-40). Springer, Singapore.

Werner, C., Wegmüller, U., Strozzi, T., & Wiesmann, A. (2002, June). Processing strategies for phase unwrapping for INSAR applications. In Proceedings of the European Conference on Synthetic Aperture Radar (EUSAR 2002) (Vol. 1, pp. 353-356).

Woodhouse, I. (2006). Introduction to microwave remote sensing. Boca Raton: CRC Press.

Xu, H., Dvorkin, J., & Nur, A. (2001). Linking oil production to surface subsidence from satellite radar interferometry. Geophysical research letters, 28(7), 1307-1310.

Yang, Q., Zhao, W., Dixon, T. H., Amelung, F., Han, W. S., & Li, P. (2015). InSAR monitoring of ground deformation due to CO2 injection at an enhanced oil recovery site, West Texas. *International Journal of Greenhouse Gas Control*, *41*, 20-28.

Zebker, H. A., & Villasenor, J. (1992). Decorrelation in interferometric radar echoes. *IEEE Transactions on geoscience and remote sensing*, *30*(5), 950-959.

Appendices

Appendix A – Sentinel-1 SAR Images used for 2015

Sentinel-1 IW SLC Image	Date of Acquisition
S1A_IW_SLC__1SDV_20150103T172415_20150103T172444_004010_004D4A_59C7	January 3, 2015
S1A_IW_SLC__1SDV_20150115T172415_20150115T172443_004185_005144_C327	January 15, 2015
S1A_IW_SLC__1SDV_20150127T172350_20150127T172426_004360_00551C_6739	January 27, 2015
S1A_IW_SLC__1SDV_20150208T172414_20150208T172443_004535_005920_45E4	February 8, 2015
S1A_IW_SLC__1SDV_20150220T172414_20150220T172448_004710_005D28_4D37	February 20, 2015
S1A_IW_SLC__1SDV_20150304T172414_20150304T172448_004885_00616B_B423	March 4, 2015
S1A_IW_SLC__1SDV_20150316T172415_20150316T172443_005060_0065AB_B456	March 16, 2015
S1A_IW_SLC__1SDV_20150328T172415_20150328T172443_005235_0069C8_02E4	March 28, 2015
S1A_IW_SLC__1SDV_20150409T172416_20150409T172449_005410_006E1A_DC0D	April 9, 2015
S1A_IW_SLC__1SDV_20150421T172416_20150421T172444_005585_007258_3430	April 21, 2015
S1A_IW_SLC__1SDV_20150503T172416_20150503T172443_005760_00765E_36F1	May 3, 2015
S1A_IW_SLC__1SDV_20150515T172417_20150515T172445_005935_007A51_99A3	May 15, 2015
S1A_IW_SLC__1SDV_20150527T172418_20150527T172446_006110_007EDE_7EBE	May 27, 2015
S1A_IW_SLC__1SDV_20150702T172419_20150702T172447_006635_008DA4_89FA	July 2, 2015
S1A_IW_SLC__1SDV_20150714T172420_20150714T172448_006810_0092A3_49A2	July 14, 2015
S1A_IW_SLC__1SDV_20150726T172421_20150726T172449_006985_009792_9B83	July 26, 2015
S1A_IW_SLC__1SDV_20150807T172424_20150807T172451_007160_009C69_41B4	August 7, 2015
S1A_IW_SLC__1SDV_20150819T172425_20150819T172452_007335_00A12A_BCDC	August 19, 2015
S1A_IW_SLC__1SDV_20150831T172425_20150831T172452_007510_00A5F7_34FB	August 31, 2015
S1A_IW_SLC__1SDV_20150912T172426_20150912T172453_007685_00AAB1_5998	September 12, 2015
S1A_IW_SLC__1SDV_20150924T172426_20150924T172453_007860_00AF57_D99C	September 24, 2015

S1A_IW_SLC__1SDV_20151006T172426_20151006T172453_008035_00B3FD_69FE	October 6, 2015
S1A_IW_SLC__1SDV_20151018T172426_20151018T172453_008210_00B8CC_9B7C	October 18, 2015
S1A_IW_SLC__1SDV_20151030T172426_20151030T172453_008385_00BD78_6385	October 30, 2015
S1A_IW_SLC__1SDV_20151111T172412_20151111T172440_008560_00C220_1ED0	November 11, 2015
S1A_IW_SLC__1SDV_20151123T172426_20151123T172453_008735_00C704_82ED	November 23, 2015
S1A_IW_SLC__1SDV_20151205T172413_20151205T172440_008910_00CBFF_AE89	December 5, 2015
S1A_IW_SLC__1SDV_20151217T172425_20151217T172452_009085_00D0CA_001C	December 17, 2015
S1A_IW_SLC__1SDV_20151229T172412_20151229T172439_009260_00D5CD_78E3	December 29, 2015

Appendix B – Sentinel-1 SAR Images used for 2016

Sentinel-1 IW SLC Image	Date of Acquisition
S1A_IW_SLC__1SDV_20160110T172424_20160110T172451_009435_00DAC4_0AF2	January 10, 2016
S1A_IW_SLC__1SDV_20160122T172411_20160122T172438_009610_00DFE4_25AF	January 22, 2016
S1A_IW_SLC__1SDV_20160203T172424_20160203T172451_009785_00E4F4_CD66	February 3, 2016
S1A_IW_SLC__1SDV_20160215T172425_20160215T172452_009960_00EA11_98D8	February 15, 2016
S1A_IW_SLC__1SDV_20160227T172423_20160227T172450_010135_00EF21_53AD	February 27, 2016
S1A_IW_SLC__1SDV_20160310T172410_20160310T172437_010310_00F422_AD7C	March 10, 2016
S1A_IW_SLC__1SDV_20160322T172424_20160322T172451_010485_00F908_A137	March 22, 2016
S1A_IW_SLC__1SDV_20160403T172411_20160403T172438_010660_00FE19_C0C4	April 3, 2016
S1A_IW_SLC__1SDV_20160415T172419_20160415T172446_010835_01035A_70A7	April 15, 2016
S1A_IW_SLC__1SDV_20160427T172412_20160427T172439_011010_0108C8_7AE1	April 27, 2016
S1A_IW_SLC__1SDV_20160509T172420_20160509T172447_011185_010E48_EB7A	May 9, 2016
S1A_IW_SLC__1SDV_20160521T172416_20160521T172443_011360_011401_361D	May 21, 2016
S1A_IW_SLC__1SDV_20160602T172420_20160602T172447_011535_0119AA_D500	June 4, 2016
S1A_IW_SLC__1SDV_20160614T172420_20160614T172448_011710_011F26_6E6D	June 14, 2016
S1A_IW_SLC__1SDH_20160708T172425_20160708T172454_012060_012A5C_F7C8	July 8, 2016
S1A_IW_SLC__1SDV_20160720T172422_20160720T172449_012235_013003_077F	July 20, 2016
S1A_IW_SLC__1SDV_20160801T172423_20160801T172450_012410_0135D4_D5F5	August 1, 2016
S1A_IW_SLC__1SDV_20160813T172424_20160813T172451_012585_013B95_5A5C	August 13, 2016
S1A_IW_SLC__1SDV_20160918T172425_20160918T172452_013110_014CF7_8000	September 18, 2016
S1A_IW_SLC__1SDV_20160930T172426_20160930T172453_013285_01529D_F6E7	September 30, 2016
S1A_IW_SLC__1SDV_20161012T172426_20161012T172453_013460_015829_E382	October 12, 2016
S1A_IW_SLC__1SDV_20161024T172426_20161024T172453_013635_015D99_544D	October 24, 2016

S1A_IW_SLC__1SDV_20161105T172425_20161105T172452_013810_016316_BC27	November 5, 2016
S1A_IW_SLC__1SDV_20161117T172425_20161117T172452_013985_01687E_B781	November 17, 2016
S1A_IW_SLC__1SDV_20161129T172425_20161129T172452_014160_016DE6_24B8	November 29, 2016
S1A_IW_SLC__1SDV_20161211T172425_20161211T172452_014335_017376_560E	December 11, 2016
S1A_IW_SLC__1SDV_20161223T172424_20161223T172451_014510_0178EB_5B17	December 23, 2016
S1B_IW_SLC__1SDV_20161006T172339_20161006T172406_002389_00408C_3619	October 6, 2016
S1B_IW_SLC__1SDV_20161018T172339_20161018T172406_002564_004543_1F6C	October 18, 2016
S1B_IW_SLC__1SDV_20161030T172339_20161030T172406_002739_004A26_6F28	October 30, 2016
S1B_IW_SLC__1SDV_20161111T172339_20161111T172406_002914_004F15_F0E7	November 11, 2016
S1B_IW_SLC__1SDV_20161123T172338_20161123T172405_003089_005402_B6F0	November 23, 2016
S1B_IW_SLC__1SDV_20161205T172338_20161205T172405_003264_005900_57C6	December 5, 2016
S1B_IW_SLC__1SDV_20161217T172338_20161217T172405_003439_005DFD_4179	December 17, 2016
S1B_IW_SLC__1SDV_20161229T172337_20161229T172404_003614_00630B_A469	December 29, 2016

Appendix C – List of CLC land usages classified into urban or non-urban

Corine Landcover Classification	Aggregated Classification
Continuous urban fabric	Urban
Discontinuous urban fabric	Urban
Industrial or commercial units	Urban
Road and rail networks and associated land	Urban
Port areas	Urban
Airports	Urban
Mineral extraction sites	Urban
Dump sites	Urban
Construction sites	Urban
Green urban areas	Non-Urban
Sport and leisure facilities	Urban
Non-irrigated arable land	Non-Urban
Permanently irrigated land	Non-Urban
Rice fields	Non-Urban
Vineyards	Non-Urban
Fruit trees and berry plantations	Non-Urban
Olive groves	Non-Urban
Pastures	Non-Urban
Annual crops associated with permanent crops	Non-Urban
Complex cultivation patterns	Non-Urban
Land principally occupied by agriculture with significant areas of natural vegetation	Non-Urban
Agro-forestry areas	Non-Urban
Broad-leaved forest	Non-Urban
Coniferous forest	Non-Urban
Mixed forest	Non-Urban
Natural grasslands	Non-Urban
Moors and heathland	Non-Urban

Sclerophyllous vegetation	Non-Urban
Transitional woodland-shrub	Non-Urban
Beaches - dunes - sands	Non-Urban
Bare rocks	Urban
Sparsely vegetated areas	Non-Urban
Burnt areas	Non-Urban
Glaciers and perpetual snow	Non-Urban
Inland marshes	Non-Urban
Peat bogs	Non-Urban
Salt marshes	Non-Urban
Salines	Non-Urban
Intertidal flats	Non-Urban
Water courses	Non-Urban
Water bodies	Non-Urban
Coastal lagoons	Non-Urban
Estuaries	Non-Urban
Sea and ocean	Non-Urban

Appendix D – Coherence Maps of the SBAS processing

For 2015 – Shown in radar coordinate system
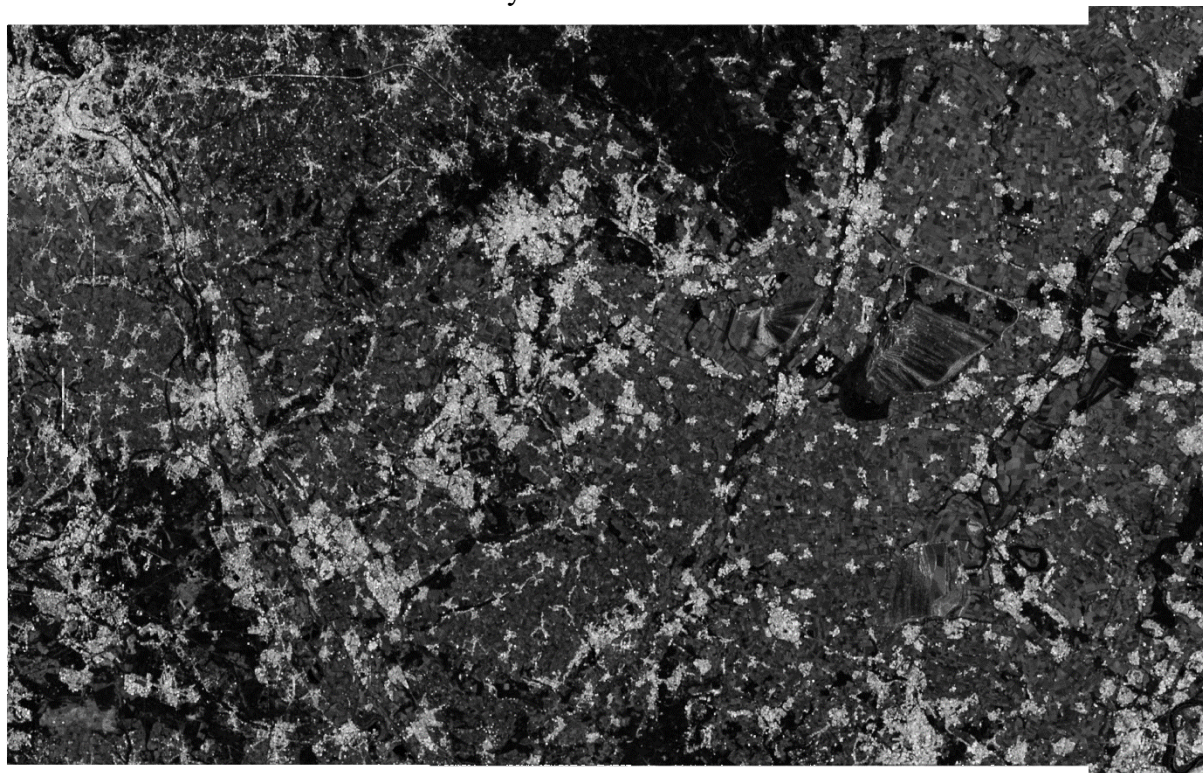
Average Coherence of All Interferograms

0.061653   0.969644

SBAS 2015 Coherence

For 2016 – Shown in radar coordinate system

Average Coherence of All Interferograms

0.064055   0.973224
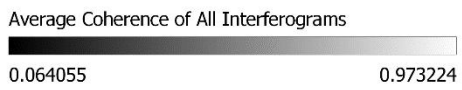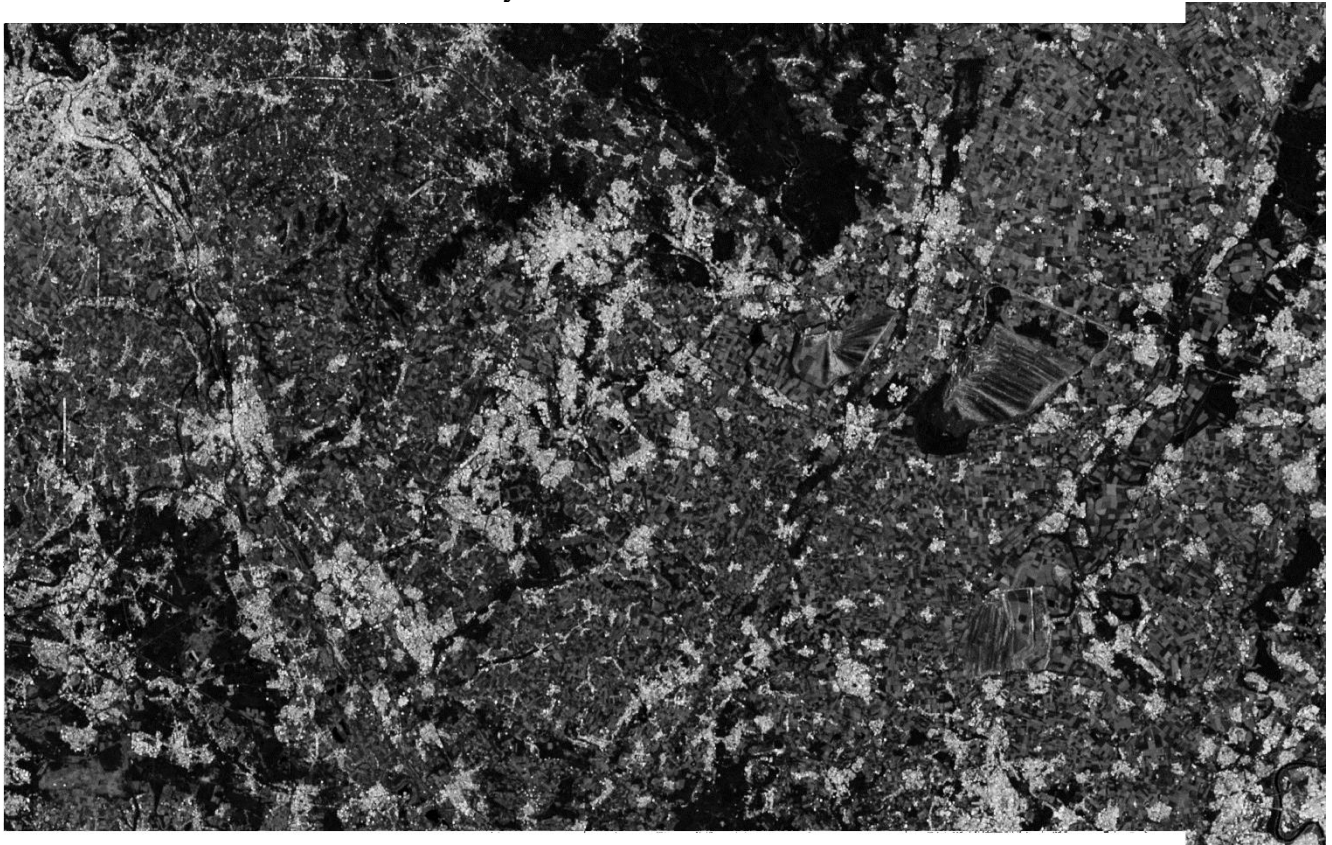
SBAS 2016 Coherence

Appendix E – Coherence Masks for SBAS Processing
For 2015 – Shown in radar coordinate system
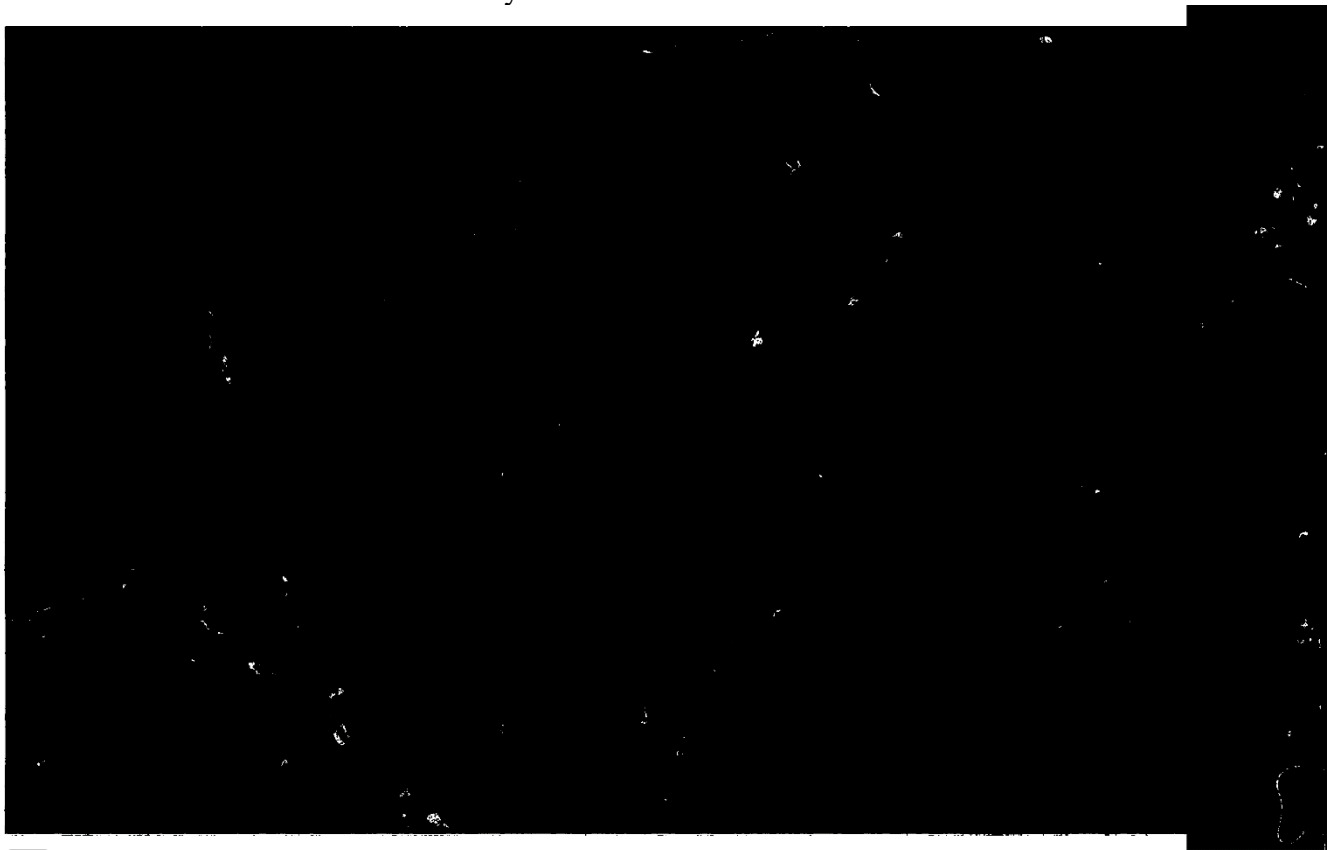
Included Areas

Masked Areas

SBAS 2015 Coherence

For 2016 – Shown in radar coordinate system

Included Areas

Masked Areas

SBAS 2016 Coherence Mask

Appendix F – Contrast Image of 2015 PSI Deformations
Deformation rates in the LoS measured by PSI for 2015 with regions of interests overlaid and a contrasting scale

97
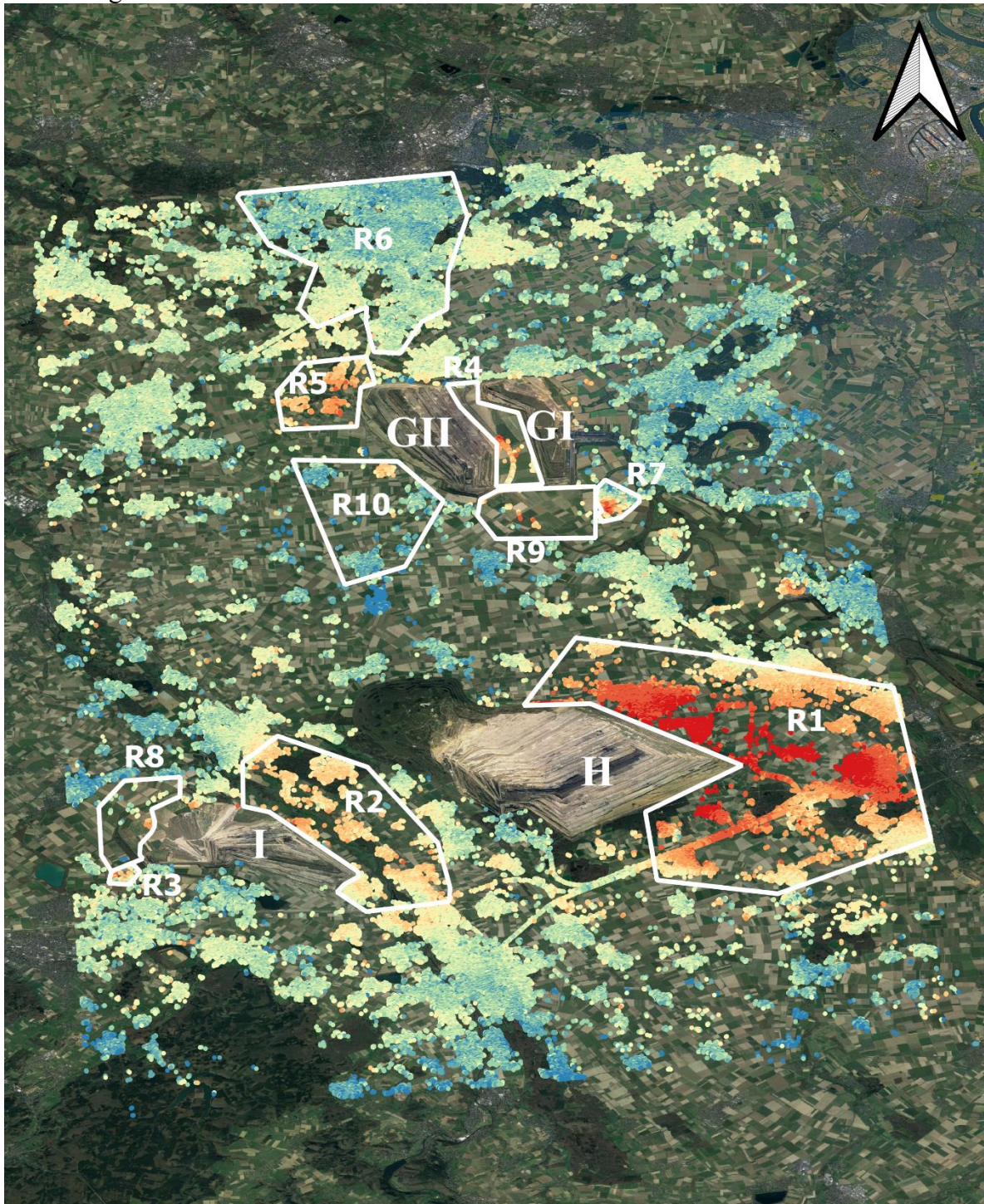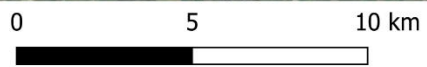
Appendix G – Contrast Image of 2016 PSI Deformations
Deformation rates in the LoS measured by PSI for 2016 with regions of interests overlaid and a contrasting scale

Appendix H – Euskirchen GNSS station positional time series
Euskirchen station positional data over 2015
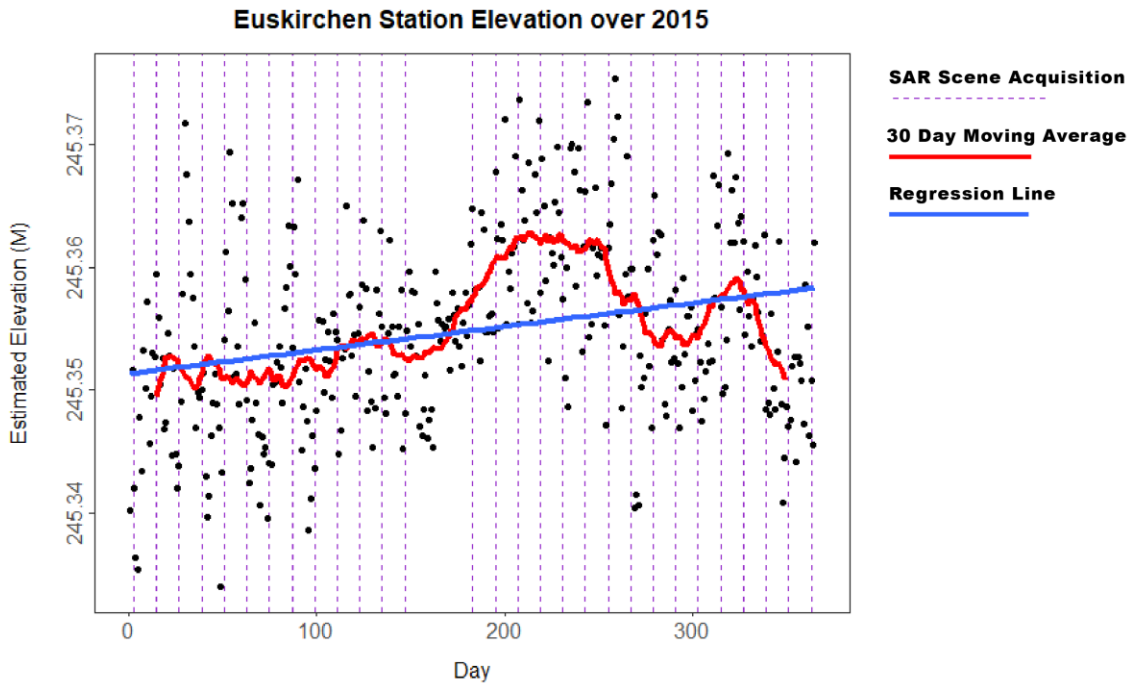
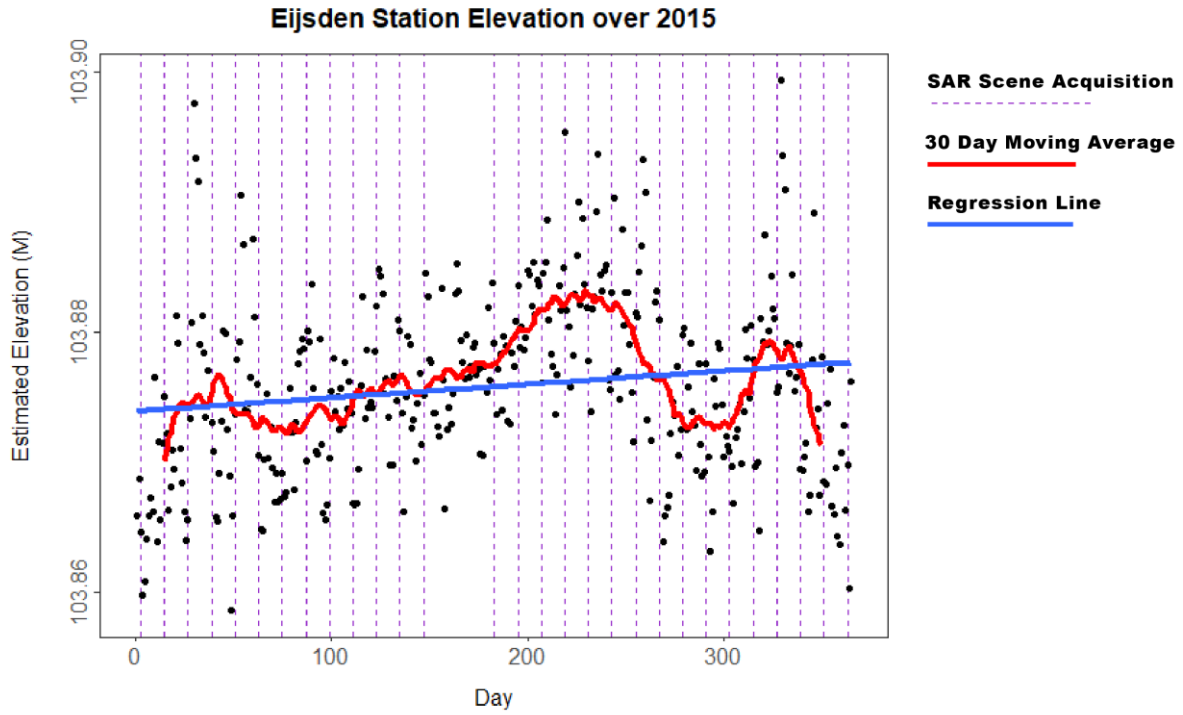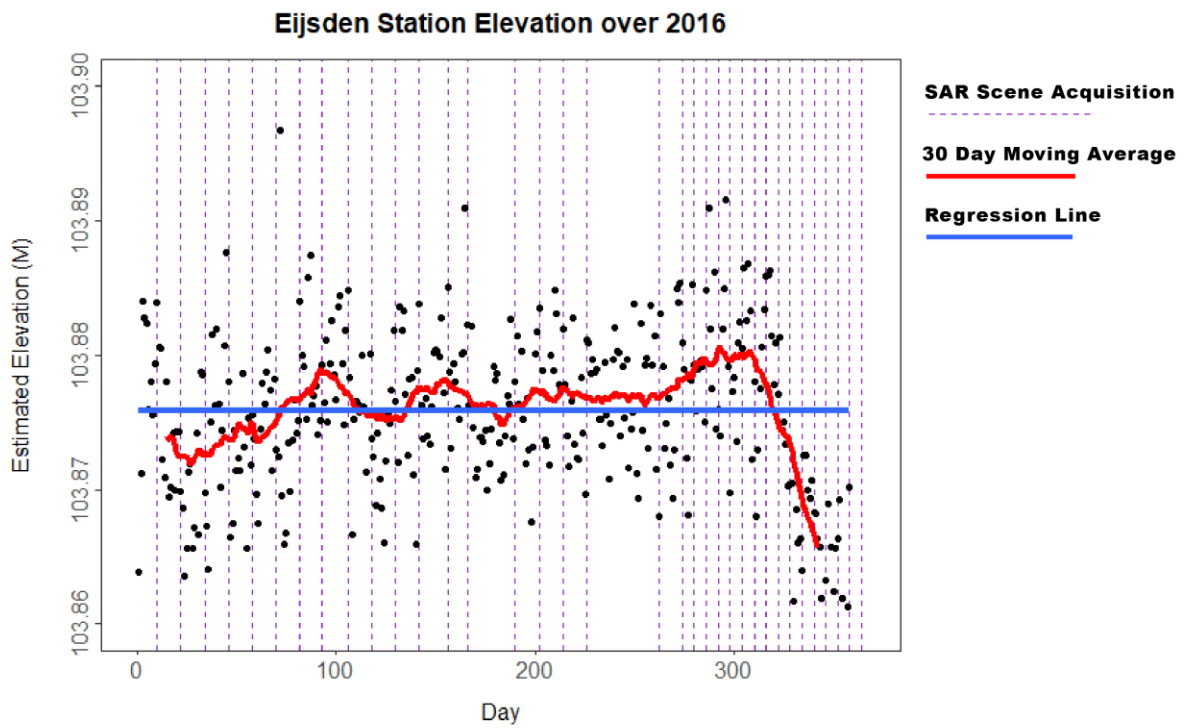Euskirchen station positional data over 2016

Euskirchen station positional data over 2014 – 2020
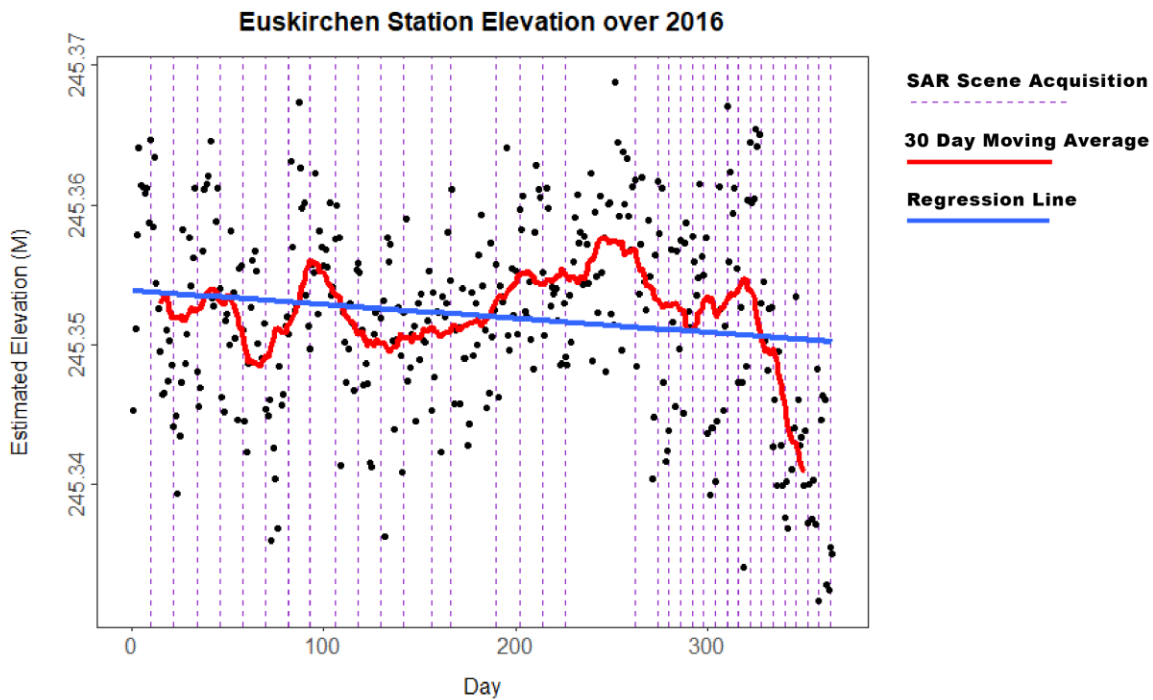
Euskirchen Station Elevation over 2014 - 2020
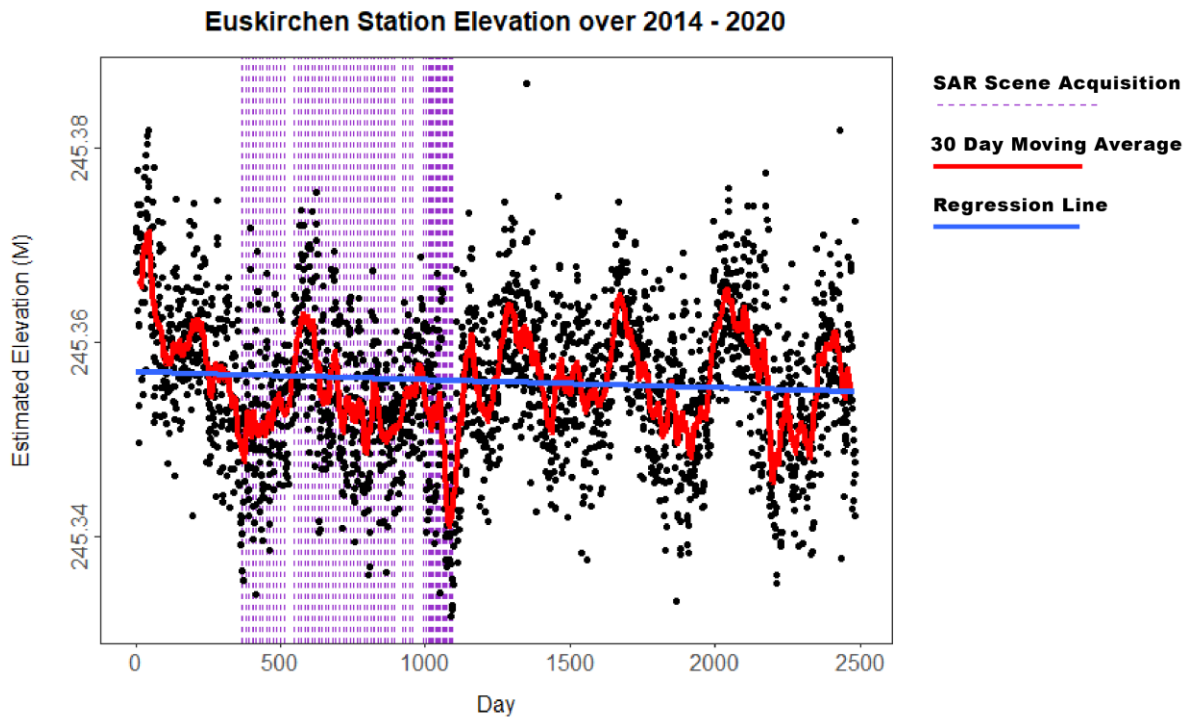
Appendix I – Eijsden GNSS station positional time series
Eijsden station positional data over 2015

Eijsden station positional data over 2015

Eijsden station positional data over 2014 – 2020

Eijsden Station Elevation over 2014 - 2020